

Design Optimisation of a Transverse Flux Linear Oscillating Generator for Resonant Free-Piston Stirling Applications

by

Louis Hoogenhout Joubert

*Thesis presented in partial fulfilment of the requirements
for the degree of Master of Science in Electrical
Engineering in the Faculty of Engineering at Stellenbosch
University*



Department of Electrical and Electronic Engineering,
University of Stellenbosch,
Private Bag X1, Matieland 7602, South Africa.

Supervisor: Dr. JM Strauss

March 2015

Declaration

By submitting this thesis electronically, I declare that the entirety of the work contained therein is my own, original work, that I am the sole author thereof (save to the extent explicitly otherwise stated), that reproduction and publication thereof by Stellenbosch University will not infringe any third party rights and that I have not previously in its entirety or in part submitted it for obtaining any qualification.

Abstract

The design optimisation of a linear oscillatory electric generator for application in free-piston Stirling engines is described in this thesis.

A basic overview of free-piston Stirling engine technology is given by firstly providing a brief description of the operation of the heat engine. The applications of free-piston Stirling engines in industry are given and the proposed future applications are described.

Different types of electrical machine designs from industry and academia are evaluated in a literature study. A classification structure is also proposed based on the magnetic flux variation within the designs.

Based on the literature study, a transverse flux, single-phase, moving magnet, tubular topology was chosen for investigation.

A three dimensional finite element simulation was chosen as the most appropriate method to model the linear electrical machine. A commercial simulation package was called from a simulation script and the outputs from the finite element simulation were again used to calculate the electrical machine performance parameters using the instantaneous voltage- and current values.

A sequential quadratic programming algorithm was used to perform optimisation of the machine topologies, with the optimisation variables being dimensional parameters that describe the machine geometry and the goal of the optimisation to minimise the active mass of the machine, while maintaining preset minima for the output power and the efficiency.

The machine was optimised for a number of different translator configurations and the different configurations were analysed and compared. It was found that a quasi-Halbach arrangement of the permanent magnets yielded the lowest overall active mass. A comparative study is also presented, where this quasi-Halbach variant is compared to a commercial machine. It was found that the linear machine design with a quasi-Halbach arrangement compares well with the commercial machine.

A prototype and test bed was designed and constructed. Due to manufacturing difficulties however, the machine could not be completed in time for testing.

Uittreksel

Die ontwerpsoptimering van 'n lineêre ossillerende elektriese generator vir toepassing in vrysuier Stirling enjins word beskryf in hierdie tesis.

'n Basiese oorsig van vrysuier Stirling enjin tegnologie word gegee deur eerstens 'n kort beskrywing te gee van die werking van die hitte-enjin. Die aanwending van vrysuier Stirling enjins in industrie word gegee en voorgestelde toekomstige toepassings word beskryf.

Verskillende tipes elektriese masjien ontwerpe vanuit die industrie en die akademie word geëvalueer in 'n literatuurstudie. 'n Klassifiseringstruktuur, gebaseer op die magnetiese vloedverandering in die ontwerpe, word ook voorgestel.

'n Transverse vloed, enkelfase, bewegende magneet, tubulêre topologie is gekies vir die ondersoek, gebaseer op die onder andere die literatuurstudie.

'n Drie-dimensionele eindige element simulاسie is gekies as die mees geskikte metode om die lineêre elektriese masjien te modelleer. 'n Kommersiële simulاسie pakket is deur middel van 'n simulاسie skrip geroep en die uitsette vanaf die eindige element simulاسie is weer gebruik om die werksverrigtingsparameters van die elektriese masjien te bereken deur gebruik te maak van die oomblikswaardes van die spanning en stroom.

'n Sekwensiële kwadratiese programmering algoritme is gebruik om optimering van die masjien topologie te doen, met die dimensionele parameters wat die masjien geometrie beskryf as die optimeringsveranderlikes en doel van die optimering om die aktiewe massa van die masjien te minimeer, terwyl die uitsetdrywing en die benuttingsgraad by voorafgestelde minima gehou word.

Die masjien is geoptimeer vir verskeie translator konfigurasies en die verskillende konfigurasies is geanaliseer en vergelyk. Dit is bevind dat 'n kwasi-Halbach skikking van die permanente magnete die laagste totale aktiewe massa gelever het. 'n Vergelykende studie is ook aangebied, waar die kwasi-Halbach variant vergelyk is met 'n kommersiële masjien. Dit is bevind dat die lineêre masjien met die kwasi-Halbach skikking baie goed vergelyk met die kommersiële masjien.

'n Prototiepe masjien en toetsopstelling is ontwerp en aan mekaar gesit. Maar as gevolg van vervaardigbaarheids tekortkominge kon toetse op die prototiepe nie betyds gedoen word nie.

Acknowledgements

I would like to express my sincere gratitude to the following people and organisations.

Dr. Johann Strauss for his guidance, support and patience. Especially for his patience.

Jacques Schutte for providing such a solid platform from which to proceed.

The ESKOM Tertiary Education Support Program for financially supporting this research.

Robert Dobson for his financial support.

Prof. Gerhard Venter for his valued advice on optimisation.

Stiaan Gerber for the occasional helping hand and the conversations on design.

The Customer Support division at *MagNet*® for their prompt and professional service.

Dedications

Hierdie tesis word opgedra aan my familie.

Contents

1	Introduction	1
1.1	Overview	1
1.2	The Stirling Engine as an Energy Conversion Mechanism	1
1.3	Project Motivation and Description	4
1.4	Thesis Structure	5
1.5	Notes to the Reader	6
2	Electrical Linear Oscillating Machines in Free-Piston Stirling Engines	9
2.1	Overview	9
2.2	Different Types of Linear Oscillating Machines	9
2.3	Axial Flux Machines	11
2.4	Transverse Flux Machines	16
2.5	Exotic Flux Machines	19
2.6	Summary	20
3	Electrical Machine Modelling and Simulation	24
3.1	Overview	24
3.2	Mathematical Approach	24
3.3	Linear Electric Machine Modelling from Simulation Outputs	30
3.4	Conclusive Remarks	45
4	A Machine Optimisation Approach	46
4.1	Overview	46
4.2	Optimisation Goal	46
4.3	Optimisation Algorithms	48
4.4	Sequential Quadratic Programming	49
4.5	Implementation	57
4.6	Conclusive Remarks	67
5	Design Evolution	68
5.1	Overview	68
5.2	Initial Design	69

CONTENTS	viii
5.3 First Design	71
5.4 Second Design	76
5.5 Third Design	85
5.6 Fourth Design	92
5.7 Fourth Design with Optimisation Based on Transient Function Evaluations . .	98
5.8 Design Review	101
6 A Brief Evaluation and Comparative Study	103
6.1 Overview	103
6.2 Project Goal	103
6.3 Comparison with a Commercial Linear Oscillating Machine	110
7 Prototype Design	112
7.1 Overview	112
7.2 Design Challenges	112
7.3 Prototype Construction	114
7.4 Conclusion	120
8 Conclusions and Recommendation	122
8.1 Analytical Machine Simulation	122
8.2 Optimisation Parameters	122
8.3 Summary	123
Bibliography	124
Appendices	128
A Dynamics of Resonant Motion	129
A.1 Principals of Undamped Harmonic Motion in Free Vibration	129
A.2 Principals of Damped Harmonic Motion in Free Vibration	130
A.3 Principals of Undamped Motion in Forced Vibration	133
A.4 Principals of Damped Motion in Forced Vibration	135
A.5 Free Piston Stirling Engine Dynamics	139
B Loss Discrepancy Investigation	140
C Commercial Machine Data sheet	146
D Prototype Schematics	147

Nomenclature

Variables

A	Area	[m ²]
F	Force	[N]
I	Electrical current amplitude	[A]
N	Number of turns	[]
P	Power	[W]
R	Electrical resistance	[Ω]
T	Time period	[s]
X	Oscillatory positional amplitude	[m]
a	Dimmensional parameter	[m]
c	Dimmensional parameter	[m]
f	Frequency	[Hz]
i	Electrical current	[A]
k	Positive integer	[]
l	Length	[m]
n	Positive integer	[]
p	Parameter	[]
v	Voltage	[V]
x	Postion	[m]
\dot{x}	Velocity	[m/s]
\ddot{x}	Acceleration	[m/s ²]
η	Efficiency	[]

λ	Magnetic flux linkage	[Wb]
τ	Lagrangian multiplier	[]
ω	Angular velocity	[rad/s]

Vectors

\vec{P}	Parameter vector
\vec{R}	Vector of residuals
\vec{S}	Search direction

Subscripts

<i>Cu</i>	Copper
<i>Loss</i>	Descriptive
<i>a</i>	Air
<i>coils</i>	Descriptive
<i>eddy</i>	Descriptive
<i>fill</i>	Descriptive
<i>hyst</i>	Descriptive
<i>in</i>	Descriptive
<i>j</i>	Positive interger
<i>m</i>	Positive Interger
<i>magnets</i>	Descriptive
<i>mech</i>	Descriptive
<i>n</i>	Positive interger
<i>out</i>	Descriptive
<i>s</i>	Section
<i>t</i>	Terminal
<i>w</i>	Width
λ	Magnetic flux

Superscripts

i Positive interger

l Lowwer

q Iteration

u Upper

List of Publications

1. J. Schutte, L.H. Joubert, J.M. Strauss, "Constrained Optimisation of a Transverse Flux PM Linear Generator," in *Electrical Machines (ICEM), 2012 XXth International conference on*. IEEE, 2012.
2. L.H. Joubert, J. Schutte, J.M. Strauss, R.T. Dobson, "Design Optimisation of a Transverse Flux, Short Stroke, Linear Generator," in *Electrical Machines (ICEM), 2012 XXth International conference on*. IEEE, 2012.
3. L.H. Joubert, J.M. Strauss, "Optimisation of a Transverse Flux Linear Oscillating Generator by Transient 3D Finite Element Analysis," in *Electrical Machines (ICEM), 2014 XXth International conference on*. IEEE, 2014.

Chapter 1

Introduction

1.1 Overview

In this chapter, the free-piston Stirling engine is described in Section 1.2. The applications of this technology is discussed in Section 1.3. A structured layout of the document is then given in Section 1.4, followed by important notes regarding the thesis in Section 1.5.

1.2 The Stirling Engine as an Energy Conversion Mechanism

Electrical machines facilitate the conversion of energy between mechanical- and electrical energy. In this study the mechanical interaction is between the electrical machine and a free-piston Stirling engine. This section provides a brief introduction to Stirling engines to explain the nature of this mechanical interaction.

The inventor of the Stirling engine, Rev. Robert Stirling was awarded a patent in 1816 for his "Air Engine" [1]. This machine was later re-named a "Stirling Engine".

The Stirling engine is a heat engine that operates under the cyclical expansion and compression of a working fluid as a result of heat transfer to and from the engine. Mechanical work can be done by a Stirling engine because of a potential energy difference between the hot and the cold side of the engine.

The Stirling engine is found in a number of different configurations, namely alpha, beta and gamma configurations [2]. This study proposes an electrical machine that is specifically designed for a beta type, free-piston configuration. As this is the only relevant configuration pertaining to this study, it is the only configuration that is described.

Free-piston Stirling technology finds its origin in the work of Dr. William Beale from Ohio University in the early 1960's. In 1969, Beale published a paper wherein the free-piston Stirling engine is first described [3]. In the same year, Beale filed a patent for his

invention [4]. The patent was awarded in 1971.

A basic schematic of the free-piston Stirling engine is shown in Figure 1.1. The operation of this engine is based on the cyclical expansion and compression of a working fluid due to temperature changes resulting from heat transfer to and from the engine. The expansion and compression of the working fluid drives the pistons into motion.

Conventional kinematic Stirling engines have a direct mechanical coupling between the displacer and power piston. Because of this the positional phase shift of the two motion components (the displacer and the power piston) is fixed. The displacer constantly displaces the working fluid between the hot and cold side of the engine. The potential heat energy differential between the hot and cold side of the engine can then constantly drive the power piston in motion due to the pressure differential caused by the rapid expansion and contraction of the working fluid. The motion of the power piston directly drives the displacer and a cycle can logically be envisioned.

Without a direct mechanical coupling, piston motion becomes difficult to explain. Intricate knowledge of the thermodynamic Stirling cycle and the linear dynamics of a resonating system is required. Such knowledge provides the required insight to envision the pressure profiles observed across the displacer in a "sprung-mass" representation. However, in keeping with the convention proposed by Strauss [5], if it is assumed that the displacer is directly driven by a linear electric motor, the explanation can be based on a kinematic Stirling engine configuration.

The easiest way to explain the operation of a kinematic Stirling engine is to divide the cycle into four steps. Firstly the working fluid is displaced to the expansion space. Secondly, the working fluid is expanded. The working fluid is then displaced to the compression space in the third step and finally, the working fluid contracts in a fourth step.

If it is assumed that the displacer is externally driven, the first step starts with the displacer at its topmost position shown in Figure 1.1. From here, it is driven downwards for a part of the downwards stroke length. Assume that the power piston is static for this first step, that is, the power piston has just completed its upward stroke and is about to begin its downward stroke. With this assumption, it can be envisioned that the displacer forces the working fluid from the compression space to the expansion space, through the regenerator.

The working fluid that now, in this second step, occupies the expansion space, receives heat energy from the heater. The influx of heat increases the temperature of the working fluid. The temperature increase causes an increase in pressure in the expansion space and drives the displacer further downward. If a constant volume is maintained within the compression space for this step, the power piston is likewise driven downwards by the rapid expansion of the working fluid in the expansion space.

For the third step, the displacer is externally driven upwards. Assume now, that the

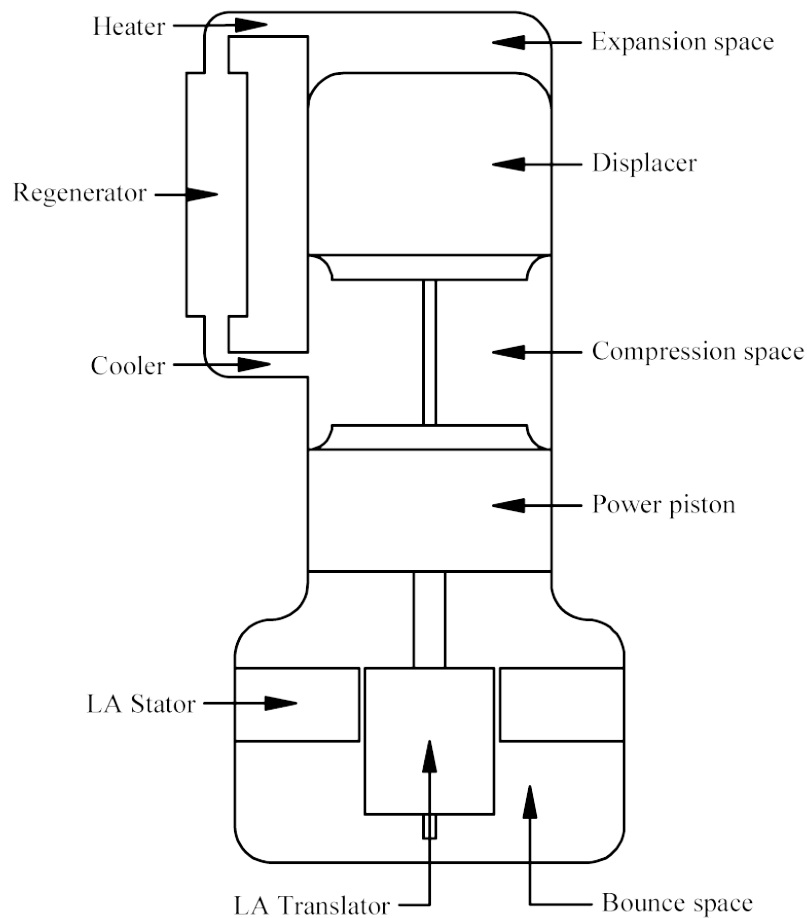


Figure 1.1: Simple schematic of a typical beta type free-piston Stirling engine.

power piston is static once more. It has just completed its downward stroke and is about to start moving upwards. With a static power piston and the displacer moving upwards, working fluid is displaced from the expansion space to the compression space through the regenerator.

In the fourth step, heat is removed from the working fluid in the compression space through the cooler. This results in a temperature drop in the working fluid which causes a drop in pressure in the compression space. Assuming a constant volume in the expansion space now, it can be envisioned that the power piston is driven upwards by this contraction stage. Both pistons are now in position for the first step to commence once more.

The engine can function without a regenerator. The inclusion of a regenerator provides an energy storage device that retains heat from every preceding cycle. This improves upon the thermodynamic Stirling heat cycle.

In reality, these steps all overlap and both pistons are in constantly in oscillatory motion. The volume of the expansion space and the volume in the compression space is always dynamic and never entirely constant for a single step. The Stirling engine is a continuously combusted engine. This makes the concise definition of individual steps problematic.

The fact that the power piston follows the motion of the driven displacer by a delayed phase angle allows the simplified explanation above to be formulated. However, it is only within a detailed examination of the thermodynamic cycle along with linear-resonant behaviour of the sprung-mass system that an accurate explanation where the displacer need not be externally driven, can be formulated. This brings to light one of the difficulties in free-piston Stirling engine design. It requires the collaboration of various specialist professionals to attend to the various aspects of such a design.

Under proper conditions, it is however known that piston oscillation occurs. As long as heat is transferred to and from the engine in adequate amounts, the pressure in the working gas continues to change and the mechanical energy resulting from the potential heat energy differential between the hot and the cold side of the engine can be converted into electrical energy with a linear electric generator fixed to the power piston [6].

The free-piston Stirling engine configuration has no mechanical coupling as is mentioned earlier and piston motion is a function of resonant behaviour. Because of this it can be designed to be practically frictionless which avoids the need for lubrication. This can only be done if flexural bearings are used to facilitate piston motion. Free-piston Stirling engines can therefore be hermetically sealed while conventional kinematic Stirling engines would risk lubricant contamination or clogging of the re-generator if sealed [7].

Hermetic sealing holds certain advantages. The thermodynamic cycle becomes a closed loop cycle. Mass does not cross the boundaries of the defined system.

An efficient working fluid can therefore be chosen to be contained within this closed loop cycle. Helium is generally chosen because it is chemically inert and has good heat transfer properties. The low friction environment in conjuncture with the chemically inert working fluid can lead to a low-maintenance design and consequently a long operational life.

The free-piston Stirling engine can also be pressurised. An increase in the mean pressure directly relates to an increase in mass of the working fluid. This increase in mass, increases the energy density of the energy conversion process.

1.3 Project Motivation and Description

Stirling engines are externally combusted heat engines. This makes them versatile, capable of operating with most types of fuel combustion or alternative heat sources. As such they have potential in space applications with heat sources such as a nuclear reactor or radioisotope decay. The low maintenance and high efficiency of the free-piston configuration contributes to the consideration of using these machines in power systems for proposed lunar and Mars surface stations [8].

Free-piston Stirling engines find similar applications in the alternative energy industry as a medium for waste heat recovery, to increase the overall efficiency of systems. *Infinia Cor-*

poration [9] and *Sunpower Inc.* [10], are likewise investigating the use of free-piston Stirling engines as modular concentrated solar to electrical energy conversion units.

A brief investigation found three projects that were funded by institutions of the United States government. It is likely that there are more such projects and there are certainly many more privately funded projects. This evaluation is a general overview to ascertain the developmental stage of the technology. It is included in this document only because the technology is relatively unknown.

In 1988, a joint venture by the *National Aeronautics and Space Administration* and the *Department of Energy*, employed the services of *Mechanical Technology Incorporated*. The goal of this project was to design and produce a 25 kW electric alternator for a free piston Stirling engine. This project was budgeted a total of \$4,9 million [11].

The "Dish Stirling Joint Venture Program" initiated in 1991, was funded by *Cummins Power Generation Inc.* and the *Department of Energy*. This project focussed on the "Stirling Solar Dish" concept and received funding to the amount of \$17,2 million [12].

In 2002, a project entitled "Radioisotope Power Conversion Technology", managed by the *National Aeronautics and Space Administration Glenn Research Centre* was funded to \$17,8 million as of 2006 [13].

These monetary figures do not represent the full costs of development that this technology has seen. However, a general idea of a well developed technology emerges.

Persistent problems with free-piston Stirling system still remain. One such problem is the power density of the electric machine. The problem that the electrical machines in free-piston Stirling engines are too big, is specifically given for the failure of some projects [14].

This project therefore focuses on designing a small electrical machine with a high power density. A dimensional optimisation is performed to minimise the mass of the electrical machine, while maintaining certain output performance measures to this end.

The *National Aeronautics and Space Administration* is considered to be a world leader in this power conversion technology with research experience that spans over 30 years [15]. The transparency of this institution as a government agency provides a good guideline by which the success of this project can be measured.

1.4 Thesis Structure

This section is an overview to present the contents of this document in a summarised form. The structured layout provides a reference framework to locate relevant information.

Chapter 2 categorises the different types of linear electric machines that are typically used in free-piston Stirling engines. The machine classification structure is based on the orientation of the magnetic flux variation.

The mathematical modelling and simulation used in the design process is described in Chapter 3. An instantaneous energy model based on a finite element simulation is employed to evaluate the linear oscillating electric generator.

In Chapter 4 the optimisation process is presented. Automated scripts communicate information between the mathematical model of the machine and the optimisation algorithm. The optimisation algorithm used in this study is the sequential quadratic programming algorithm.

Chapter 5 describes the design evolution of the electrical machine. The work presented is a comparative study. The machine design is changed based on observations and insights gained from evaluating the optimisations.

The final machine design is evaluated and compared to an industry leader in Chapter 6. The focus of this evaluation is on the integration of the electrical machine into a free-piston Stirling engine.

A test bed that incorporates the prototype is designed and constructed. Manufacturing difficulties in the assembly of the translator inhibited construction. Due to time constraints, the prototype was never tested. This is discussed in Chapter 7.

Comments and recommendations are made in conclusion of this thesis. This is done in Chapter 8.

1.5 Notes to the Reader

- Existing electrical machine configurations for this application are very diverse. In a literature study with so many different configurations that can be discussed, many design configurations must be left out. If every configuration of linear machine ever developed for free-piston Stirling applications were discussed, Chapter 2 would simply be too long. A general trend is therefore presented to illustrate the different paths followed by preceding machine designers.
- In Chapter 2, very little information regarding the performance measures of the electrical machines, such as the specific power or power-to-weight ratio is given. This is due to two factors.
 - Firstly, there is generally very little publicised data on these machines. Many of these machines are only depicted in diagrams with no information regarding the performance measures.
 - Secondly, the performance measures of these machines can very rarely be directly compared to one another. The output performance measures are dependent on the stroke length of the machine, the operating frequency, the output power and

the efficiency. If these four variables are not exactly the same for two different machines, they cannot be compared to each other.

- A colour convention that is used in illustrations of the electrical machines presented in this thesis is as follows. Grey represents electric steel components. Brown represents the copper windings of the coils. Blue represents magnets that are radially magnetised in an outward direction. Red represents magnets that are radially magnetised in an inward direction. Magnets that are not magnetised in a radial direction but in any other direction are shown in purple.
- Short stroke linear electrical machines differ fundamentally from rotating electrical machines. There are two main reasons for this.
 - After the start-up, rotating machines generally continue to rotate in a fixed direction. Short stroke linear machines constantly oscillate. As soon as the translator starts moving in one direction, it almost immediately needs to slow down again and stop only to then immediately start moving in the opposite direction. At a 50 Hz operating frequency, a linear machine's translator stops and starts moving in the opposite direction 100 times every second. General rotating machine conventions are quite often not applicable to short stroke linear electrical machines for this reason.
 - In rotating electrical machine design, it is often found that sinusoidal profiles are desired in current and voltage curves. Because of this, idealised models often describe rotating electrical machines using sinusoidal profiles and design goals often strive to accomplish sinusoidal outputs. This is not the case for short stroke linear machines in this specific application. Linearised models, that is, reducing Stirling engine motion and forces to be sinusoidal, misrepresent Stirling engine inputs to these linear machines. Non-linearities are specifically exploited in free-piston Stirling engine design to improve stability of resonant operation. These include non-linearities in the electrical machines such as the reluctance forces with regard to the translator position. Even though sinusoidal motion is assumed later in this thesis, conventional linearised representations serve no purpose in this linear electric machine design.
- In this thesis, mathematical simulation refers to the analysis of the physical laws of electromagnetism within the geometry. This typically relates to the dynamic behaviour of magnetic flux in the machine. Mathematical model refers to the holistic overview of the machine. This typically relates to the output power characteristics and the mass of the machine.

-
- Generally, the mathematical simulation results are used as inputs to the mathematical model. With these inputs, the mathematical model is used to calculate the performance measures of the machine.

Chapter 2

Electrical Linear Oscillating Machines in Free-Piston Stirling Engines

2.1 Overview

This chapter is dedicated to describing the different types of electrical machines that are generally used in free-piston Stirling engines. Section 2.2 provides a brief introduction to the first machine designed for this specific application. This section then proceeds to create a classification structure within which the different types of machines can be categorised.

These categories, namely axial-, transverse- and exotic flux machines, are explained in Sections 2.3, 2.4 and 2.5 respectively. These categories are described using historic examples as well as machines that are currently used in industry and machines proposed in literature. A summary then concludes this chapter in Section 2.6.

2.2 Different Types of Linear Oscillating Machines

The first publication that indicates the use of a linear electric machine in a free-piston Stirling engine design, is a paper written by Beale in 1969 [3]. Little reference is made to the electric machine but a diagrammatic sketch indicates its general configuration. Figure 2.1 shows the design depicted in this article.

This design appears to incorporate two stationary coils, cylindrically wound in an iron-cored stator. Magnets are fixed to the power piston shaft that would logically have to be radially magnetised in an inward and an outward direction respectively. An inner iron core affixed to the shaft between the two magnets completes the magnetic flux path. The changing magnetic flux-linkage in the iron core, as a function of the magnet position, induces a voltage in the enclosed coils.

From this point forward, many papers have been published with the goal of producing

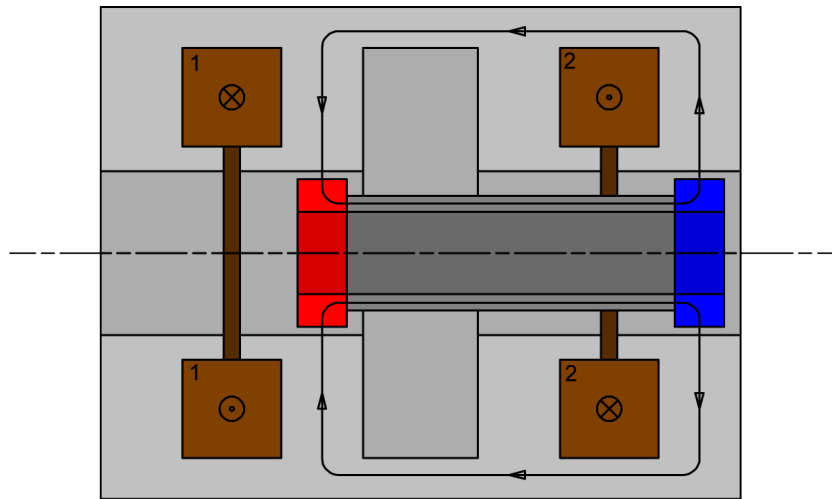


Figure 2.1: Schematic of the first free-piston Stirling engine application specific linear oscillating machine by Beale [3].

the best application specific electrical machine design. A few of the important designs are discussed in the following sections.

As is often the case with emerging technologies, subsequent designs have a great diversity. Input and output parameters, design goals, operating conditions and free-piston Stirling engine application (heat pumps, concentrated solar etc.) vary from one design to the next. In-order to create a coherent structure that describes the development of this technology, certain liberties have to be taken in terms of machine classification.

The easiest way to create a classification structure, is to define categories based on the magnetic flux variation as a function of the translator position. Three categories exist in this regard.

In Section 2.3, axial flux machines are discussed. Axial flux machines have magnetic flux variations in a plane oriented along the axis of motion as illustrated in the left-hand image of Figure 2.2. Generally speaking, this plane can be rotated along the axis of motion to exhibit an identical flux profile at any angle. These types of machines usually have cylindrical coils with moving elements along the axis of that cylinder.

In Section 2.4, transverse flux machines are discussed. Transverse flux machines have magnetic flux variations in a plane perpendicular to the axis of motion as illustrated in the right-hand image of Figure 2.2. Generally speaking, this plane can be shifted along the axis of motion to exhibit a similar magnetic flux path. These types of machines usually have multiple coils wound around "spokes" that protrude towards the centre of the machine.

In Section 2.5, exotic flux machines are discussed. This is a category that is created simply

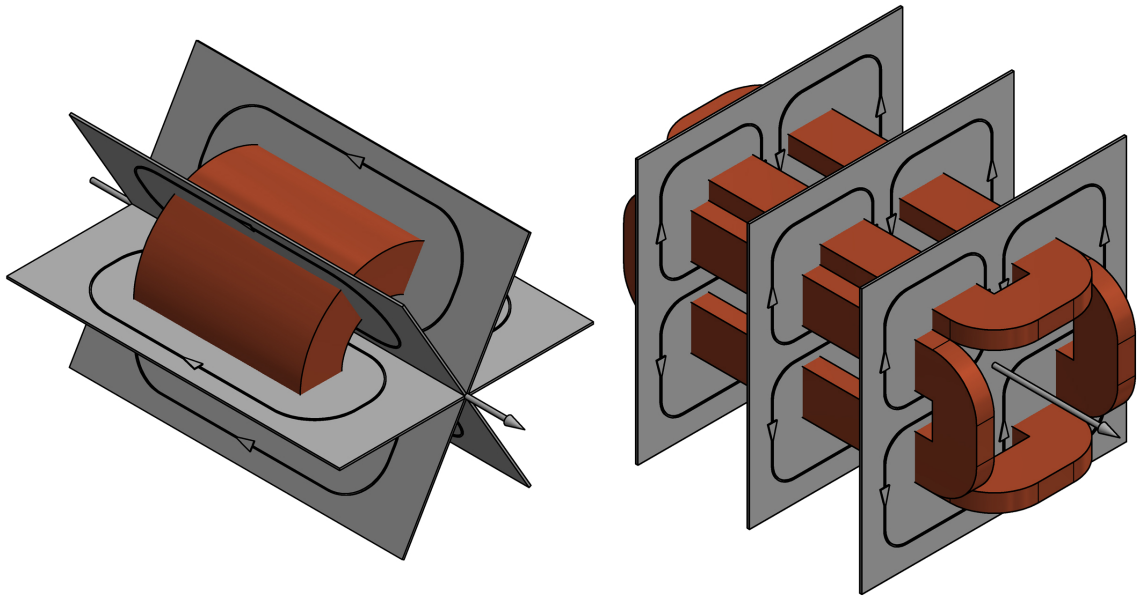


Figure 2.2: Magnetic flux planes on the axis of motion.

to classify machines that do not fall under the previous two general descriptions. It is often found that the magnetic flux variations in these machines could, if not aligned with the utmost precision, cause a torsion around the axis of motion. Mechanical difficulties that arise from this possible torsion, result in the disqualification of such designs for free-piston Stirling engine applications in general. There are however a few viable designs that fall under this classification.

2.3 Axial Flux Machines

The early development of electrical machines to be used specifically in free-piston Stirling engines is dominated by this type of machine. There is, however a further divide in machines that have this type of magnetic flux linkage. Two subcategories are therefore created in the pursuit of clarity. Moving coil machines generally have a stationary magnetic field in which the coils are oscillated. Moving magnet machines have a varying magnetic flux linkage across stationary coils due to oscillating magnets.

2.3.1 Moving Coil Axial Flux Machines

In 1977, an article was published by Beale under his newly-founded company, *Sunpower Inc.*, with a diagram showing a moving coil design [16]. This design is illustrated in Figure 2.3. No detailed description of the electric machine is given in the article, but it is clear that it functions as follows.

This design depicted in Figure 2.3 shows a stationary magnetic field with a moving coil.

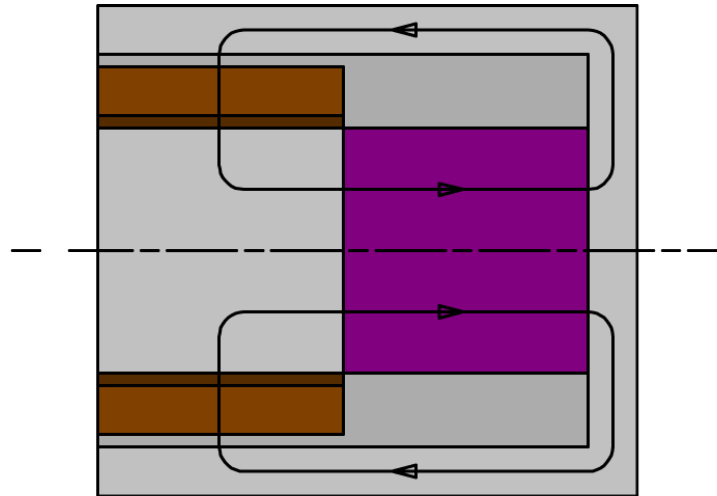


Figure 2.3: An early moving coil axial flux design by Beale [16].

The cylindrical, stationary permanent magnet would have to be magnetised along its axis. In the figure the purple magnet is magnetised from left to right. The axial flux path is completed by means of a back-iron stator shown in grey. The cylindrically wound coil, shown in brown, appears to be fixed to the power piston shaft and oscillates within the stationary magnetic field. As the coil moves within this magnetic field, a voltage is induced.

The *Department of Energy* of the United States of America and the *National Aeronautics and Space Administration* signed a collaboration agreement in 1982 to the benefit of free-piston Stirling engine research [17]. The product of this collaboration was published in 1985, where a detailed description of a moving coil design is given [18]. The design described in this publication has an identical configuration to that of the machine shown in Figure 2.3.

The operating conditions and performance measures of this machine reveal that the 3 kW generator, operating at a frequency of 60 Hz over a stroke-length of 50 mm has an electromagnetically active mass of about 98 kg. This is considered to be a large mass for the output power of 3 kW.

In more modern times, Strauss [5] investigated a machine with significantly better performance measures. In 2013, Strauss proposed the design depicted in Figure 2.4.

This design employs radially magnetised magnets shown in red and blue. The magnets create a static magnetic field that is completed by two back iron stators shown in grey. The stators form inner and outer cylinders. Moving coils, shown in brown, are proposed to oscillate within the resulting static magnetic field. Figure 2.4 shows an example configuration with six radially magnetised magnets and three moving coils.

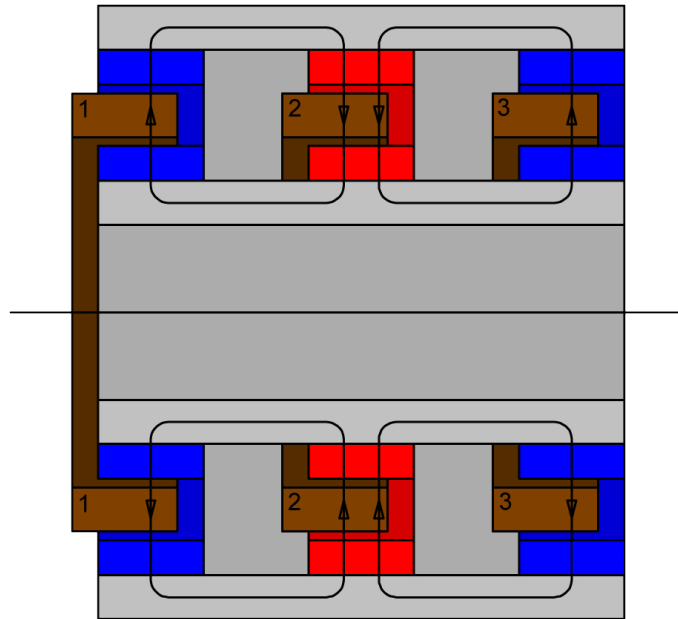


Figure 2.4: Axial flux moving coil configuration proposed by Strauss [5].

This design was not intended for a free-piston Stirling engine operating at a natural resonant frequency, as is the case for the project described in this document. The design of Strauss proposes to enforce a different control strategy on the Stirling engine with the goal of maximising the thermodynamic efficiency.

Nevertheless, within resonant applications, this design appears to operate at increased specific power levels compared to that of the *Department of Energy and National Aeronautics and Space Administration* collaboration published in 1985.

2.3.2 Moving Magnet Axial Flux Machines

This specific configuration is the most widespread in literature. The first diagram published by Beale as was shown in Figure 2.1, illustrates such a design.

A publication from Sunpower Inc. in 1987 by Berchowicz, Richter and Shade contains a diagram that indicates a simplified axial flux moving magnet design [10]. This design, shown in Figure 2.5, uses a single coil encased in an outer stator. The translator likely has three ring magnets that are radially magnetised and mounted on a back-iron.

Once more, little information on the linear electric machine is provided. However, the fundamental layout of the *Sunpower Inc.* design remained unchanged for 20 years. This is known because a diagram published in an article by Kim and Berchowicz in 2006 [19] shows a very similar design.

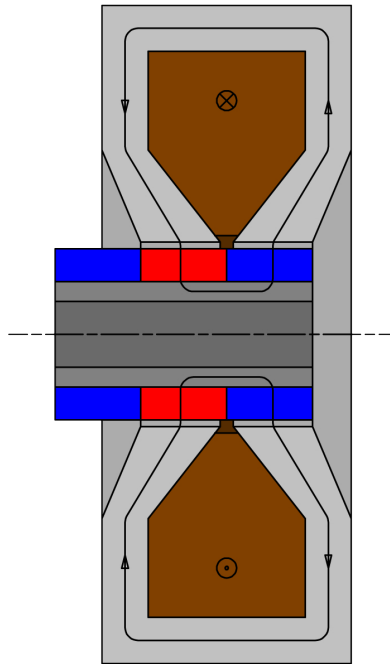


Figure 2.5: The *Sunpower Inc.* stationary coil, axial flux configuration by Berchowit *et al.* [10].

The magnetic flux in the stator changes as a function of the translator position. In Figure 2.5 the translator is shown in the extreme left-hand position. As the translator moves to the right, the magnetic flux in the stator reverses direction. This change in magnetic flux induces a voltage in the enclosed coil.

The laminate structure of this machine remains unclear. Wedge-shaped laminations could be used to construct the stator and translator components shown in grey in Figure 2.5. It is also possible that a soft magnetic compound is used instead of laminations to construct these stator and translator components.

In the case of the stator, regular flat laminations could be used. The use of regular flat laminations would then imply that the outer periphery of the stator is not solid. This can however not be the case for the translator structure. The translator structure could use magnets in a Halbach array that would eliminate the need for a back-iron translator structure. This is however only conjecture as no detailed description of the machine is given.

The manufacturing process for this machine configuration would have to be more complex than that of other machine configurations. This is cause for concern with regards to this specific topology.

A dual air-gap configuration is proposed in a publication by Dhar *et al.* from *Mechanical Technology Inc.* in 1989 [20]. This design, shown in Figure 2.6, operates in a manner similar to the machine employed by *Sunpower Inc.* that was shown in Figure 2.5 .

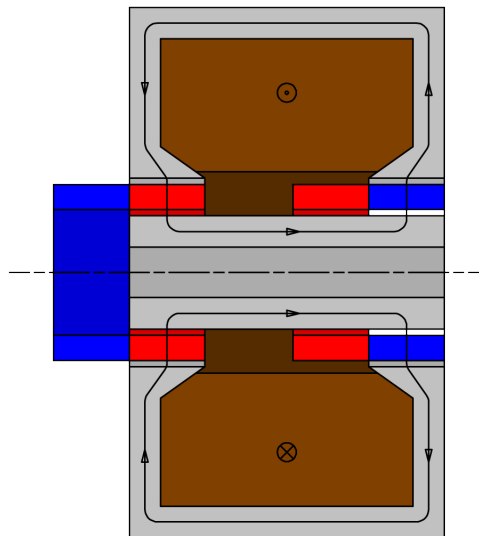


Figure 2.6: Axial flux, stationary coil configuration from *Mechanical Technology Inc.* [20].

The design of Dhar *et al.* uses two translator segments as opposed to the single translator configuration of the *Sunpower Inc.* machine. These translator segments, the blue and red magnets shown in the extreme left-hand position in Figure 2.6, oscillate in-between the inner- and outer stator, shown in grey. The changing magnet position reverses the flux-linkage and consequently induces a voltage in the brown coil enclosed within the outer stator.

As is the case for the *Sunpower Inc.* design shown in Figure 2.5, the manufacturing process for the machine design of Dhar *et al.* remains unclear. Once again the laminate structure of the stator components could be problematic.

A multi-phase machine of this type was designed by P. Zheng, X. Gan and L. Li. A publication in 2010 [21] describes a 1 kW machine that weighs only 2.9 kg. This is a remarkably high power density for linear machines of this type. However, there is no indication of the stroke-length, operating frequency or current density in the publication. The efficiency is however given at 86.7%.

A study published by Gerber [22] in 2011 shows the design of a moving magnet, axial flux configuration as illustrated in Figure 2.7. This design is only presented as a case study and no indication is given of the performance measures.

The design of Gerber has sets of cylindrically wound coils within an inner and outer stator. The radially magnetised ring magnets oscillate within a dual air-gap between the two stators.

The brown coils in Figure 2.7 are numbered from one to four. The red and blue magnets of the translator are shown in the extreme left-hand position. As the translator moves to the

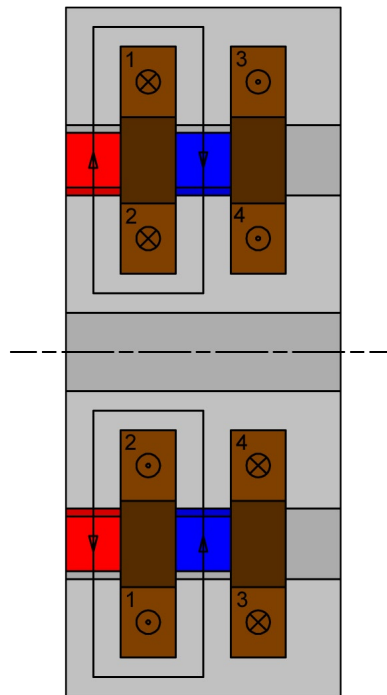


Figure 2.7: Axial flux moving magnet configuration with stationary coils proposed by Gerber [22].

right, the flux-linkage in the grey stators that initially enclose coils one and two, is reversed and encloses the other coils numbered three and four. The varying magnetic flux, resulting from the translator motion, induces a voltage in the four coils.

All of the machine designs evaluated in this section suffer from the same drawback in manufacturability as mentioned several times. It appears that any moving magnet, axial flux linear machine design requires the use of soft magnetic compounds, wedge-shaped laminations or a complex flat laminate structure. This appears to be an inherent drawback for all machines of this type.

2.4 Transverse Flux Machines

In 1977, a textbook by Boldea and Nassar [23] shows a transverse flux design as illustrated in Figure 2.8. This design is a moving iron machine, where segments of the translator intermittently completes a magnetic flux path through coils wound around "spokes" protruding towards the centre of the machine.

Figure 2.8 shows a sectioned isometric view of Boldea and Nassar's design. The stationary blue and red magnets in the figure are fixed to the large grey stator. The stator can be

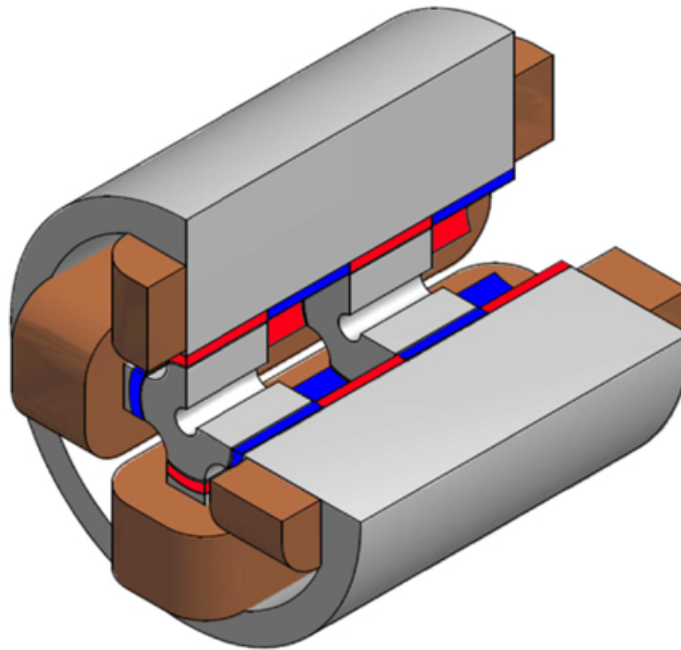


Figure 2.8: Moving iron, transverse flux design proposed by Boldea and Nassar [23].

constructed using identical flat laminations stacked from the bottom left to the top right of the figure. The translator sections, constructed in a similar fashion as the stator, completes the flux-linkage of one set of magnets. As the translator sections move towards the top right, they complete the flux-linkage of the next set of magnets that are magnetised in the opposing direction to the first set. This reverses the flux-linkage that the coils enclose and consequently induces a voltage.

This design exhibits a poor power to weight ratio, as found by Schutte and Strauss [24] in 2010. Even so, a foundation for tubular transverse flux linear oscillating electric machines is established by this design.

A dual air-gap machine illustrated in Figure 2.9, with the moving magnets oscillating at the outer periphery of the coils, was presented by Qiu *et al.* from *Infinia Corp.* [9] in 2005. Little regarding the performance measures is published about this design.

Figure 2.9, a sectioned isometric view, shows the red and blue magnets of the translator in a position to the bottom left. The circular outer stator and the star-shaped inner stator is shown in grey. Brown coils encircle the protruding spokes of the inner stator. As the magnets move towards the top right, the flux-linkage in the coils is reversed, inducing a voltage.

Schutte, Joubert and Strauss proposed a design similar to that of Boldea and Nassar in 2012 [25]. In this design the magnets are fixed to the translator as illustrated in Figure 2.10.

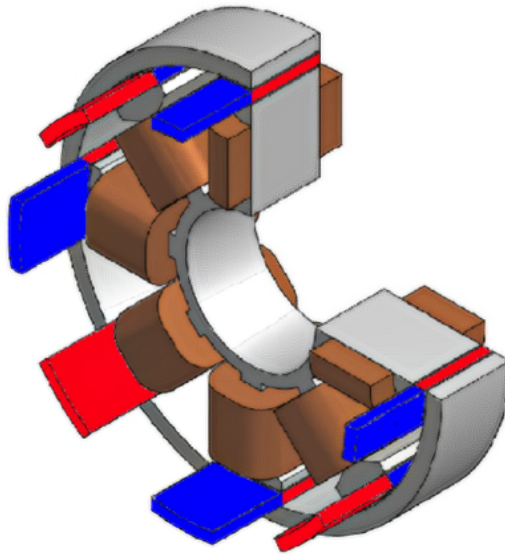


Figure 2.9: Dual air-gap, transverse flux design by Qiu *et al.* from *Infinia Corp.* [9].

This design addresses the issue of the poor power to weight ratio of the design proposed by Boldea and Nassar with some success.

The sectioned isometric view in Figure 2.10, shows the moving magnet design with the translator in the bottom left position. As the translator moves to the top right, the magnetic flux-linkage is reversed to induce a voltage in the coils. Cosic proposed a strikingly similar multiphase design of this configuration for longer stroke applications [26].

Q-drives, a commercial company, manufactures and sells machines that appear to be of a transverse flux design. This design is shown in Figure 2.11. The performance measures are

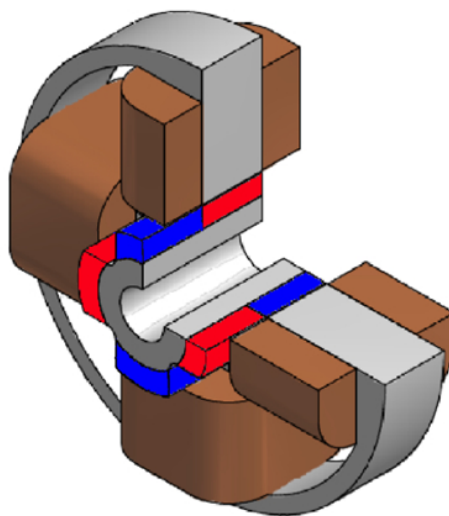


Figure 2.10: Moving magnet, transverse flux design by Schutte *et al.* [25].

documented on their website [27]. This linear alternator is reportedly used by the *National Aeronautics and Space Administration* in recent free-piston Stirling engines [28].

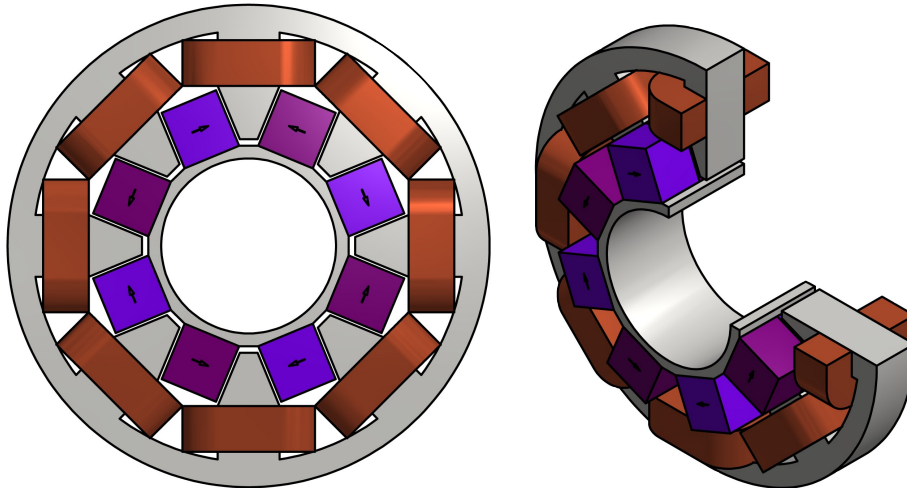


Figure 2.11: Schematic of the *Q-drives* machine by Cory and Yarr [27].

The *Q-drives* design by Cory and Yarr was awarded a patent in 1995 [29]. From the information in the patent and on the website, the design appears to work in the following manner.

Figure 2.11, shows the dual air-gap, moving magnet configuration. The magnets, shown in purple, appear to be flat and seem to be magnetised in a direction perpendicular to the axis of motion.

As the translator oscillates, it reverses the magnetic flux-linkage in the stator spokes. This flux-linkage is encircled by the stator windings and consequently a voltage is induced in these windings.

This machine does not appear to be tubular. This implies that a torsion around the axis of motion would be present, should this design function as a generator. This is a possible disadvantage of this machine design.

2.5 Exotic Flux Machines

As previously stated, the majority of exotic flux machines could cause an unwanted torsion around the axis of motion. There is one design however that is rather intriguing that has no such risk.

Govindaraj, Chatterjee and Ganguli presented a design in 2009 with an air-gap perpendicular to the axis of motion [30]. This design is shown in Figure 2.12.

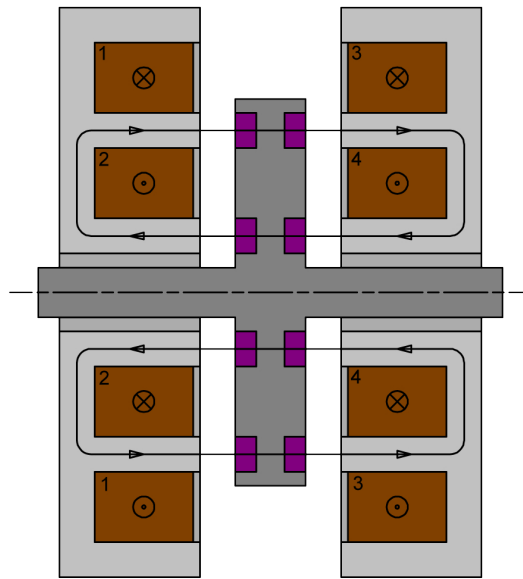


Figure 2.12: Exotic flux design by Govindaraj *et al.* [30]

The nature of this design is such that the air-gap varies as a function of the translator position. The magnitude of the force will therefore increase exponentially as the translator reaches the limits of the stroke length. This presents an interesting force profile along the axis of motion, which may be beneficial to Stirling engine operation.

The force profile perpendicular to the axis of motion should also not increase as a function of the applied load. This could prove beneficial in terms of the flexure bearing design.

In-order to obtain a high power density, however, the stroke length will need to be very short and this may prove to be a problem in Stirling engine applications. The mass of the translator appears to be quite high and this could limit the operating frequency, compounding the stroke length issue.

2.6 Summary

Two decisions need to be made with regards to the machine topology that is to be designed in this thesis. Firstly, the general characteristics need to be established. Then, within these general characteristics, a specific layout needs to be chosen.

The general machine characteristics refer to the number of phases and poles of the machine. The operating conditions are important regarding this decision, i.e. how the energy is to be extracted from the generator and how this effects the Stirling engine on a mechanical basis. This decision is discussed in Section 2.6.1.

The specific layout refers to the magnetic flux variation within the machine structure.

The orientation and structure of electromagnetically active components is the focus of this decision, discussed in Section 2.6.2.

2.6.1 General Characteristics

Within a free-piston Stirling system, the linear electric machine serves a dual purpose. Naturally it is a medium by which the mechanical energy of the power piston is converted into electrical energy. The second function is to enforce the stable operation of the Stirling system.

The force that the electric generator exerts on the power piston consists of two components. One component is constant, the other is variable.

The constant force component is the reluctance force. This force component is entirely dependent on the geometry of the machine. It relates to the natural resting position of the magnets within the iron-cored stator. As the position of the translator is disturbed from this position, a reactant force acts to restore the natural position. As the reluctance force is dependent on the translator position alone, it can be related to a non-linear mechanical spring constant.

The variable force component relates to the electromagnetic interaction between the stator and the translator. When the translator is in motion, the magnetic flux in the iron core varies. This variance in magnetic flux induces a voltage within the encircling coils. This voltage is dependent on the translator velocity.

If an electric load is applied to the coils a current is produced in the coils that again produces a magnetic field that counteracts the original magnetic field. This results in a force on the translator.

As this force resists the translator as a function of velocity and electric load, it can be modelled as a mechanical damper with a variable damping coefficient.

The profile of the force consisting of these two components can, if designed correctly, enforce stability within a free-piston Stirling engine operating at a natural frequency resonance. It can only be done in these relatively simple terms of a "spring-damper system" if the current is driven in phase with the electromotive force and if the machine is of a single phase design.

The design philosophy of the system is therefore that the power piston's oscillation amplitude is controlled by the linear electric machine's driven current amplitude. To increase the power piston's oscillatory amplitude, the amplitude of the driven current is decreased. To decrease the power piston's oscillatory amplitude, the driven current amplitude is increased. The characteristics of linear resonant systems is described in Appendix A.

This is, however not the only reason for choosing a single phase design. Within rotary machines, the output power profile is smoother in multiple phase machines than in single

phase machines (which is generally desired in rotary machine systems). This can generally be done without compromising the specific power of the machine. The main reason for this is because magnetic pole pairs that leave the domain of one phase, enter the domain of another phase.

This is not the case within short-stroke linear oscillatory machines. Additional phases (a two or more phased machine) is simply impractical due to the very short stroke of the machine, while the control of the machine is increased in complexity, that is to maintain a simple "spring-damper" system.

The force profile of a multi-phase machine is therefore undesired regarding the control of the Stirling system and the specific power of a multi-phase machine will likely be diminished if such a design is employed. This is certainly not the case for all linear machines but in this application specific design, a multi-phase topology appears to be a poor choice. This is in complete agreement with electrical machines used in free-piston Stirling engines in the past.

2.6.2 Specific Topology

The differences between axial flux designs and transverse flux designs are not significant enough to completely disregard one or the other for free piston Stirling applications. This is why the use both can be found in in the developmental history of the technology.

One of the industry leaders, *Sunpower Inc.* employs an axial flux design [19], another industry leader, *Infinia Corp.* employs a transverse flux one [9]. No definite motivation can be given for the choice of investigating a transverse flux machine in this project instead of an axial flux one.

Regarding specific performance measures, Redlich [31] observes that no moving magnet topology has a distinct advantage over other moving magnet topologies. When choosing a specific topology, other considerations need to be taken into account. One such consideration is the manufacturability of the electrical machine.

It has already been mentioned that the manufacturability of axial flux machines is concerning. Such machines can easily be manufactured if a solid iron core is used. The use of a solid iron core is predicted to have substantial eddy current losses due to the varying magnetic flux in the iron core.

An alternative to a solid iron core, is to construct the core out of wedge-shaped laminations. Wedge-shaped laminations are expensive and difficult to manufacture.

A secondary alternative is to construct the core out of soft magnetic compounds. Soft magnetic compounds are difficult to manufacture due to the brittle nature of these materials. Soft magnetic compounds are produced using an oxidation and sintering process on powder metallics. This results in difficulties when manufacturing techniques using any form of tool-

ing is employed. Furthermore, soft magnetic compounds are expensive and generally have a lower permeability than laminate silicon steel. This generally relates to a lower specific power in machines employing soft magnetic compounds in relation to machines employing a laminate steel structure.

The third alternative is to design an axial flux machine in a moving coil configuration where a solid core will not have a varying magnetic field and will consequently not have core losses. Here the coil connections present a manufacturing problem. If a moving coil configuration is designed, sliding or flexing contacts need to be employed. Both sliding and flexing contacts have an adverse effect on the design life of the electrical machine and consequently the Stirling system.

Despite these limitations, both the use of soft magnetic compounds in moving magnet axial flux topologies and the use of flexing contacts in moving coil axial flux topologies are being investigated at Stellenbosch University in parallel projects. The reason for this is because very little is known regarding the performance measures of different topologies in direct comparison with each other.

For reasons that will become clear in Section 3.2, it is considered that transverse flux machines can only be accurately simulated by a three dimensional finite element method. Recent advances in computational technologies have made the use of this method more accessible. It can therefore be argued that until recent times, accurate representations of transverse flux machines were limited. Logically transverse flux linear machines would then be less developed than the axial flux counterparts. This is only conjecture but warrants further investigation.

A prototype of Schutte's machine was built using a mechanical design produced by the author which established the ease of manufacturability for the transverse flux topology [32]. Considering that the manufacturability of axial flux topologies is cause for concern, the decision was made to proceed with a transverse flux topology.

This decision is supported by the parallel investigations at the University. This is because designs resulting from the other projects need to be compared to the transverse flux topology at some stage in the future.

Chapter 3

Electrical Machine Modelling and Simulation

3.1 Overview

In this chapter the mathematical model that is used to analyse the electromagnetic and mechanical properties of the linear electric machine is described. The practical implementation of this model follows thereafter.

In Section 3.2, the different types of mathematical simulation techniques are described that can be used to analyse a transverse flux linear electric machine. The focus of this section is on finding a simulation technique that can be integrated into an optimisation.

The implementation of the chosen mathematical simulation technique into the mathematical model of the machine is described in Section 3.3. This mathematical model considers both an optimisation of the machine parameters and the integration of the electric machine design method into the holistic design process of a free-piston Stirling engine.

3.2 Mathematical Approach

3.2.1 Different Types of Mathematical Simulation Techniques

Generally speaking there are two predominant approaches to obtain a mathematical simulation of an electrical machine. One approach is to use an analytical simulation and the other approach is to use a numerical simulation.

Numerical simulations are usually of either a finite element type or a finite difference type. The finite element simulation uses an area or volume representation. The finite difference simulation uses a nodal representation. Finite element approaches are more prevalent and consequently they are the only type to be considered in this study.

The first step in obtaining a mathematical simulation technique for the machine is to con-

sider the conditions in which the machine needs to operate. These conditions are discussed in Section 3.2.2. The considerations of an analytical approach are discussed in Section 3.2.3. Numerical methods are then discussed in Section 3.2.4.

3.2.2 Operating Conditions

Free-piston Stirling engines are relatively simple mechanical devices that consist of only two moving parts. The design of such a machine is, however, a complex process.

The thermodynamic cycle and heat exchanger, the thin-walled pressure vessel, the mechanics of resonant motion, the non-linear deformation of the flexure bearings and the linear electric machine all generally require a specialist in these fields to design. Due to this interdisciplinary collaboration, the different models employed within the various designs require flexibility to adapt to a holistic overview of the system.

In the approach taken in this thesis, sinusoidal motion is assumed as this is a fair approximation to the motion of the power piston. Within the Stirling engine, however, the actual motion of the power piston deviates from a precise sinusoidal motion. This is predominantly due to non-linearities in the Stirling gas cycle.

Non-linearities in the Stirling gas cycle causes pressure profiles that deviate from an idealised model. The force acting on the pistons, resulting from the pressure differentials, deviate from a sinusoidal profile. The positional vector that describes piston motion therefore also deviates from a sinusoidal profile.

As the profile of the piston motion deviates from that of a precise sinusoidal curve, the profile of the driven current has to adapt. This is because it is the mechanism by which the reacting force profile of the translator (affixed to the power piston) is regulated.

Furthermore, it is found by Schutte [32] that the flux linkage profile for transverse flux, moving magnet topologies deviate from a sinusoidal profile under no-load conditions. This happens even when the motion of the translator is defined as by precise sinusoidal curve. This is due to the fact that both magnetic pole pairs influence the flux-linkage at all positions within the short stroke length. As the magnetic flux components deviate from a sinusoidal curve, the induced voltage components likewise deviate from a sinusoidal curve. This was observed in simulation and verified experimentally.

In light of this, the mathematical simulation used in a model that describes the electrical machine cannot restrict itself to representing the machine using only sinusoidal representations. In doing so, it would undermine the holistic design of the system, since the machine is misrepresented by ignoring crucial non-linearities. Any mathematical representation that relies on a phasor analysis inherently linearises the problem, adds very little value in this specific application and is consequently disregarded.

The mathematical simulation approach has to be based on an instantaneous response.

The mathematical simulation can then still, regardless of the profile that the different components are presented in, accurately represent the machine. This is done to allow flexibility in the model so that it can adapt to the holistic system at a later stage.

3.2.3 Analytical Simulation Techniques

Boldea and Nassar [23] proposed an analytical simulation approach for a moving iron topology in 1977. This topology has already been illustrated in Figure 2.8. The behaviour of the electromagnetic properties for this moving iron topology is considered to be similar to the behaviour of the electromagnetic properties of the machine topology described in this thesis.

The simulation approach of Boldea and Nassar is to construct a reluctance network that represents the geometry of the machine. By analysing this reluctance network, a linear approximation to the magnetic flux-linkage is obtained. This is a typical magnetic equivalent circuit analysis.

The flux-linkage in this approach is the sum of the flux-linkage caused by the permanent magnetic field as a function of the translator position and the flux-linkage created by the electromagnetic field caused by the current in the coils. This approach accurately describes the machine but only for a limited range of geometric representations.

As the geometry of the machine changes beyond the scope that this simulation technique was originally intended for, inaccuracies in the magnetic flux-linkage calculations manifest. These inaccuracies are the result of two contributing factors.

The first factor is magnetic saturation. Some geometries could contain areas with high magnetic flux densities. When high magnetic flux densities are present, the silicon steel laminations become magnetically saturated. When magnetic saturation occurs, the behaviour of the magnetic flux-linkage can no longer be accurately described by a linearised simulation technique.

The second factor relates to the magnetic equivalent circuit. As the geometry varies beyond the scope envisioned by the creator of the mathematical simulation, new reluctance paths become prevalent [32]. These reluctance paths are generally ignored by creator of the mathematical simulation because the paths are only significant within geometric variations of the machine that are not logical to pursue. When a geometry is presented where these reluctance paths are significant, the simulation that ignores these paths can no longer accurately represent the electromagnetic behaviour.

Optimisation algorithms cannot make the distinction between geometries that are accurately represented in simulation and geometries that are not accurately represented. An optimisation algorithm is a design tool that systematically steps through different parameter combinations without preconceived notions of what the end result should look like. This can often lead to counter intuitive geometric configurations. An optimisation algorithm can

therefore "suggest" configurations that the design engineer would otherwise not consider. If the mathematical simulation approach is formulated within preconceived restrictions, this aspect of optimisation is lost.

Furthermore, an approach that does not account for saturation in the laminate steel, would require a restriction on the maximum magnetic flux density to keep the machine within the design space where the representation is valid. This would be perfectly acceptable if it was known that the optimum design lies within this region. It was found by Schutte [32] in a previous study, however, that this is not the case.

It can also be logically determined that when the mass of a machine is to be minimised, the iron core will saturate. The level of saturation will be restricted by the desired efficiency, but the iron will saturate because the optimisation algorithm strives to use as little material as possible.

Cosic [33], proposed an analytical simulation approach for a similar, three-phase transverse flux design with crank-less internal combustion applications in mind. Cosic's method is based on the same principals as that of Boldea and Nassar. Even so, this approach has a more complex three-dimensional reluctance network that could address some of the issues. But even this approach, however complex, could not accurately represent all the reluctance paths for all geometric variations. Furthermore, the fundamental problem of a linear simulation technique persists.

It is true that an analytical simulation method can be created that does account for magnetic saturation within the laminate steel components. Such a simulation technique can specifically focus on mapping all possible reluctance paths within a magnetic equivalent circuit with the goal of using it in optimisation. However, in the light of these previous simulation techniques and the inherent limitations of analytical simulations for this specific type of machine design, it was decided to follow an alternative path.

The analytical simulation approaches discussed in this section are found in a well regarded text book [23] and in a doctoral dissertation [33]. Creating an analytical simulation that produces reliable results in an optimisation environment that out performs the approaches discussed above, falls beyond the scope of this study.

It should be noted that there are recent advances in this approach, specifically as proposed by Seibold in 2014 [34] for rotating transverse flux machines. This specific analytical simulation does account for saturation within the laminate electric steel structure and presents a reluctance network of previously unparalleled complexity. Such an approach needs to be considered in future work. This analytical simulation was, however, publicised after the decision was made to proceed with an alternative approach.

3.2.4 Numerical Simulation Techniques

The finite element method is a numerical method that divides the machine geometry into smaller elements. These elements are then individually solved using Maxwell's equations that define the laws of electromagnetics. Boundary information is communicated from one element to the next in such a way that the holistic geometry is represented. Machine geometry can either be represented in a two-dimensional plane or in a three-dimensional volume.

Two-Dimensional Finite Element Simulation

A two-dimensional finite element analysis represents a machine within a two-dimensional plane. This can only be done if the magnetic flux variations in this two-dimensional plane can be replicated to represent the three-dimensional structure of the machine. The characteristics of the machine can then be extrapolated from this two-dimensional representation.

In the case of a transverse flux linear machine, the motion of the translator and the dynamic changes in magnetic flux are not in the same two-dimensional plane. If the magnetic flux variations were to occur in the "xy" plane, the translator motion would be along the "z" axis. It is therefore physically impossible to model this type of linear machine using a single two-dimensional finite element simulation. Alternatives to the conventional representation therefore need to be considered.

It is conceivable to represent this machine using multiple two-dimensional finite element simulations. There are, however, concerns regarding this approach.

When the translator approaches the central position, the flux-linkage within the stator core is affected by both magnetic pole pairs of the translator. If a two-dimensional plane is simulated, only the effects of one of the magnetic pole pairs can be accounted for.

Furthermore, it is later found in Chapter 5, that the optimum design has a large diameter and a short length. More like that of a disk than a tube. The magnetic end effects therefore have a significant influence on the machine and cannot be disregarded as is the case in a two-dimensional simulation.

Magnetic end effects refer to the magnetic field on the boundary between two materials with different magnetic properties. Generally this phenomenon can be ignored because the effected area is small compared to the unaffected area. If the machine geometry were to resemble that of a tube, with a small diameter and a long length, the end effects would have a limited influence on the machine. If the machine geometry resembles that of a disk, however, with a large diameter and a short length, the end effects can no longer be ignored.

Within a finite element environment, a three-dimensional representation provides the highest degree of confidence regarding simulation accuracy. This is true for almost all electrical machine configurations. It is often found that the discrepancies between a two-dimensional and a three-dimensional environment is inconsequential. That is not the case

for this particular machine. This is due to the inherently three-dimensional nature of the magnetic flux and the significant influence of the magnetic end effects.

Three-Dimensional Finite Element Method

The three-dimensional finite element simulation method is the only viable option with regard to conceiving a quantifiable representation of this specific electrical machine, for a wide variety of geometric configurations. The two-dimensional finite element simulation technique cannot account for magnetic end effects and cannot account for the inherently three-dimensional nature of the magnetic flux. Most existing analytical simulation techniques cannot account for magnetic saturation and struggle with geometric configurations outside a predetermined range. The three-dimensional finite element simulation is therefore the simulation technique that is used in this study.

Two different finite element simulation approaches can be considered, namely a static simulation and a dynamic or transient simulation. The distinction between the two lies within a consideration of the time domain.

A static approach simulates the machine at predefined intervals in time. Each of these simulations is regarded as a single problem. The machine state is simulated at different intervals where the translator position and current in the coils are established. The order in which these problems are solved is irrelevant because they are all individual problems.

A transient approach consecutively solves the machine state as a function of time. The initial conditions for subsequent time intervals are communicated from the preceding interval. In this manner, the simulation can directly account for effects caused by dynamic changes in the magnetic flux.

A transient analysis is more accurate than a static analysis, but takes more time to complete, since there is more information that needs to be communicated and more calculations that need to be performed. Both of these methods are used in this study.

Transient finite element simulations are usually used to establish the steady state of a machine. Generally a transient simulation is initiated with an electric load applied to the machine. Because the transient simulation communicates initial conditions from one time interval to the next, the electrical current at steady state conditions can be determined. This is not the case for this study.

In this design, the electrical current is proposed to be driven (in phase with the electromotive force) by power electronics. As such the steady state of the current is known. The transient simulation type is therefore a "forced transient" and not the general "free transient". The transient simulations used in this project are used for the sole purpose of calculating the time dependent losses that a static simulation cannot account for.

3.3 Linear Electric Machine Modelling from Simulation Outputs

3.3.1 Overview

This thesis documents a study in design optimisation. In such a study, the machine model serves an important function. It is a tool that allows different configurations of different topologies to be compared directly to each other.

An optimisation algorithm finds the best set of numbers within an allowable range. It does so by comparing the results from one set of numbers to the results from another set of numbers. This is where the model comes into play.

A model needs to receive a set of numbers and relate these numbers to a physical machine. This machine then needs to be analysed using a mathematical simulation and yield results in a form that the optimisation algorithm can understand.

As a work-flow process, the model receives a set of inputs and delivers a set of outputs. In Section 3.3.2 the model inputs are discussed, the mathematical simulation set-up is described in Section 3.3.3 and the model outputs in Section 3.3.4.

The representative model is written in the open-source scripting software language, *Python*. This *Python* script receives the model inputs and processes them into the format required for the mathematical simulation.

The information is then passed to a second script written in *Microsoft® Visual Basic®*. This second script is responsible for the mathematical simulation.

Upon the completion of the mathematical simulation the results are communicated back to the *Python* modelling script. The *Python* script then processes the information and produces the model outputs.

3.3.2 Model Inputs

The model inputs are simple numerical values produced by the optimisation algorithm as the optimisation parameter vector. These parameters are used to, amongst others, directly describe the geometry of the machine. In addition to describing the geometry, the amplitude of the current in the coils is part of the parameter vector but only in the case when a transient simulation technique is used to simulate the machine.

Generally, when working with an optimisation parameter vector, the values need to be scaled or normalised to represent the different inputs of a mathematical simulation. In the case of this study, it is not necessary because the dimensional variables they represent are of a comparable order of magnitude and can be directly related as lengths in millimetres or angles in degrees.

Figure 3.1, shows an example of simulation inputs as dimensional parameters. The mathematical simulation is only performed on a section of the linear machine as will be discussed in Section 3.3.3.

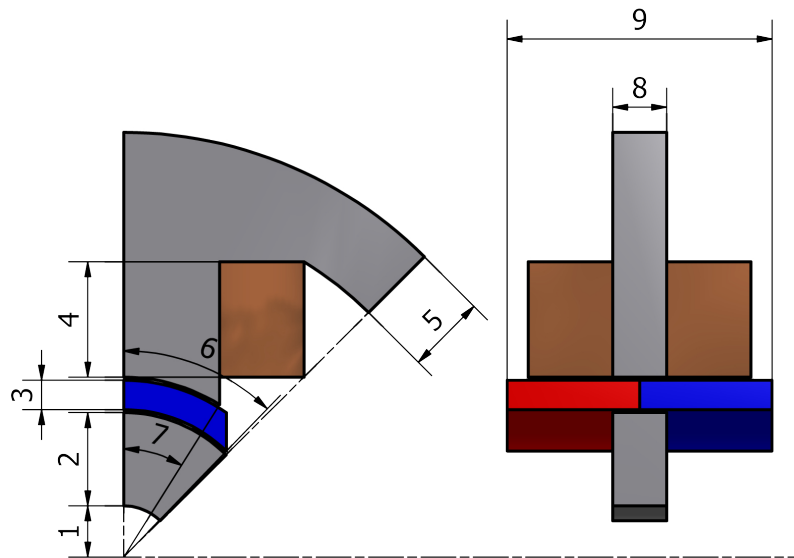


Figure 3.1: An example of simulation parameters.

The only exception where an optimisation input parameter needs to be scaled is when a transient simulation requires a current amplitude input in Ampere. In this case, where a single turn equivalent simulation is performed, the optimisation input parameter that represents the current amplitude is simply multiplied by relevant scaling factor. This is done so that the optimisation parameters all have a similar sensitivity on the simulation.

3.3.3 Simulation Set-up

This section describes the mathematical simulation of the machine. A script, written in *Microsoft® Visual Basic®* automates the drawing, simulation and extraction of results from *Infolytica's MagNet®*. The structure of the script is shown in Figure 3.2.

Two different types of simulation are performed in this study, namely static- and transient simulations. Up to a point the structure used to perform the two simulation types are identical. Where the structure differs for the two different types of simulation techniques, the distinction is made.

Within the finite element environment, symmetry can be exploited in-order to simulate a small part of the electrical machine. This section can be scaled to represent the full machine at a later stage. In this study the smallest repeating section is that of one half of one coil. This was already illustrated in Figure 3.1. In the case of a static simulation where the losses

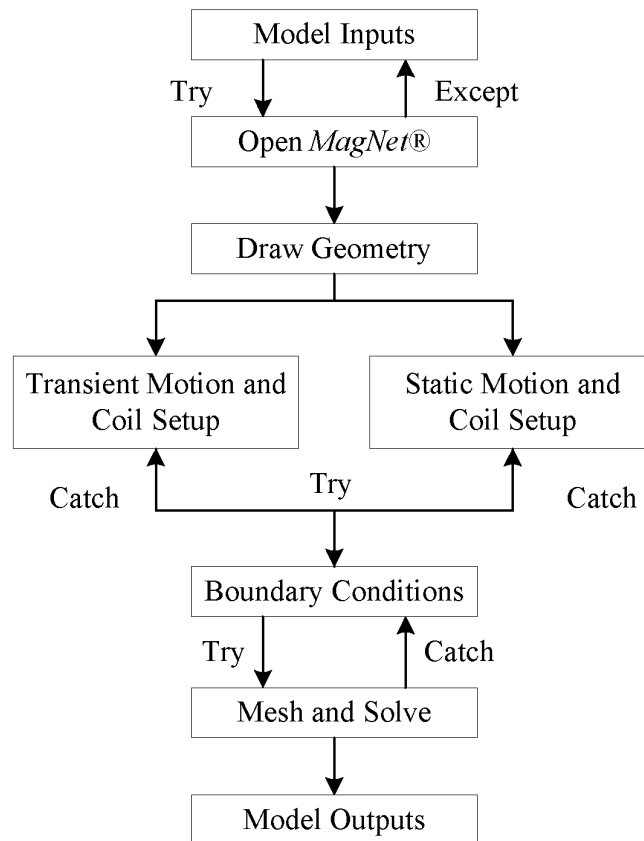


Figure 3.2: Simulation Script Structure

due to time-varying magnetic flux are not taken into account, only one half of the motion cycle can be simulated. The full cycle properties can be extrapolated from the information produced by a half-cycle simulation.

Open MagNet

When all model inputs are received and converted into the correct format, the *Python* script initialises the *Visual Basic*[®] simulation script. The *Visual Basic*[®] simulation script is initialised as an executable file. Within this initialisation the first measure is taken to create a stable platform for the unusually long time required to perform an optimisation. This is illustrated by the top two blocks of Figure 3.2.

The *Visual Basic*[®] simulation script needs to initialise *MagNet*[®]. *MagNet*[®] is licensed software with limited licenses available on the network. If the licenses are in use, or if the network server is down, the software cannot be initialised.

This would not prove to be a problem in most optimisation routines, however, for this study an optimisation often requires weeks to complete. The optimisation would never be able to converge if measures are not taken to create a stable simulation environment.

The first routine that addresses this stability issue is a *Python* "try, except" loop. This

loop continually tries to initialise the *Visual Basic*[®] simulation script until it is successful. A software licence can be obtained in this simple manner without inhibiting the network. This is because other users on the network receive a message from *MagNet*[®], telling them that their simulation will start as soon a license becomes available. A licence will become available as soon as the simulation performed by the script is complete. When all licences are in use, the script will constantly try to obtain one. The script will obtain a licence when another user's simulation completes. Or, in the case of server down-time, when the server is running again.

At this stage, an observation should be made regarding semantics. In Figure 3.2, a "try, except" and a "try, catch" loop describes the same process. The only difference between the two is the software language that the loop is written in. The "try, except" loop is a *Python* routine and the "try, catch" loop is a *Visual Basic*[®] routine.

Draw Geometry

When *MagNet*[®] has been opened, the machine is drawn by the *Visual Basic*[®] simulation script, to the dimensions given by the *Python* modelling script upon initialisation. This is illustrated by the Draw Geometry block in Figure 3.2.

Material properties are assigned to the appropriate volumes. The material properties are given in Table 3.1.

Table 3.1: Material properties.

Component	Grade and Specification
1) Steel Laminations	M19 guage 24
2) Coil	Copper Stranded
3) Magnets	NdFeB N36

An airbox is drawn to enclose the machine and a second airbox is drawn to enclose the moving elements. This is done to create a volume of dense mesh around the critical components as will be discussed later when the meshing process is described.

Next, the motion components are defined and the driven current in the coil is configured. This is where the static- and transient simulation methods differ.

Static Simulation Motion and Coil Set-up

In Figure 3.2, the motion and coil set-up for the static simulation is represented by the Static Motion and Coil Set-up block. In this process, the translator position in time,

$$x(t) = X \sin(\omega t) \quad (3.3.1)$$

is divided into eleven steps, k . It is defined using the stroke length, X , and oscillatory frequency, ω (in radians per second).

The oscillatory frequency,

$$\omega = 2\pi f \quad (3.3.2)$$

is defined from the frequency, f (in Hz). The k (eleven in this study) time intervals,

$$t_n = \frac{n}{2f(k-1)}, n = 0, 1, 2, \dots, (k-1), \quad (3.3.3)$$

taken from the frequency, f , is defined taking into consideration that only one half of one cycle is simulated.

The driven current in the coil is then set up. For the static optimisation, the current amplitude is calculated. This is because the static simulation only accounts for copper losses in the coil. All other loss mechanisms are ignored.

The geometry of the machine is known. From the geometry, the resistance of the coil can be calculated. Taking the copper fill factor, k_{fill} , into account, the resistance,

$$R = \frac{n_{coils} \rho_{Cu} l_{Cu}}{k_{fill} A_{Cu}} \quad (3.3.4)$$

of the coils can be calculated using the resistivity of copper, ρ_{Cu} , the mean conductor length, l_{Cu} and cross sectional area of the coil, A_{Cu} , calculated from the machine geometry.

With the desired efficiency of the optimisation problem, $\eta_{desired}$, the coil losses,

$$P_{loss} = \frac{P_{out}(\eta_{desired} - 1)}{\eta_{desired}} \quad (3.3.5)$$

at the desired output power, P_{out} , can be calculated.

Finally, the root mean square of the current amplitude,

$$I_{RMS} = \sqrt{\frac{|P_{loss}|}{R}} \quad (3.3.6)$$

that will deliver the desired efficiency when the desired output power levels are achieved, is calculated.

From this, the instantaneous current values in the coil

$$i(t) = \sqrt{2} I_{RMS} \sin(\omega t) \quad (3.3.7)$$

can now be implemented to the corresponding positions of the translator, as defined by the

time intervals, t_n from Equation 3.3.3.

The driven current amplitude is calculated in this way, so that the optimisation problem becomes less complex. For this set-up, the current amplitude need not be an optimisation variable and the efficiency need not be a constraint.

Transient Simulation Motion and Coil Set-up

The transient motion and coil set-up is depicted by the Transient Simulation Motion and Coil Set-up block in Figure 3.2. For the transient simulation, more loss mechanisms are taken into account. For this reason the current amplitude cannot be calculated from the desired efficiency. The current amplitude is therefore a variable and the efficiency is a constraint for the transient optimisation.

Due to hysteresis, the transient simulation is performed over a full oscillation cycle. Added to this full cycle, two additional time steps are simulated. These two time steps are added because the first two time steps of the transient simulation produce inaccurate results.

Each time step in a transient simulation requires initial conditions. The initial conditions are communicated from the preceding time step. The very first time step has no initial condition information, so values of zero are taken instead. This results in transient start-up inaccuracies. From experience it is observed that the transient start-up inaccuracies only effect the first two time intervals. This is why two additional time intervals are simulated in-order to obtain accurate simulation information over a full oscillation cycle.

The *Visual Basic*[®] simulation script for the transient simulation is less complex than that of the static simulation, because *MagNet*[®] has built-in functions to set up the motion components and the coil parameters.

The script for the transient simulation therefore only needs to communicate stroke length, X , the frequency f , the current amplitude, I and the time intervals. Twenty two time intervals were chosen for this project but only the information from the last twenty time intervals is used.

What follows in the script for the transient and the static simulations are, once again, identical.

Boundary Conditions

The boundary conditions need to be established. Only one half of one coil is simulated. The purpose of the boundary conditions is to relay how this section is replicated to form a whole machine.

MagNet[®] defines two different types of boundary conditions, namely a "flux normal" and a "flux tangential" boundary condition. The "flux normal" boundary condition stipulates

that the magnetic flux pierces the boundary surface perpendicularly. The "flux tangential" boundary condition stipulates that the magnetic flux varies along the boundary surface.

In Figure 3.3, the two different boundary conditions are shown. Yellow indicates a "flux tangential" boundary condition and green indicates a "flux normal" boundary condition.

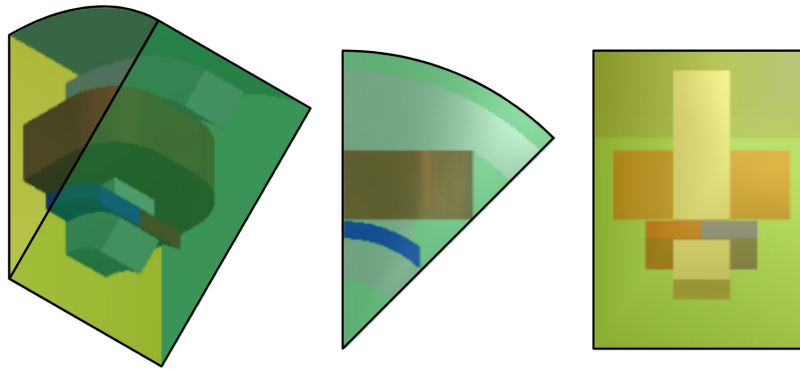


Figure 3.3: Boundary conditions on the simulated section of the electrical machine.

At this stage in the scripting process another problem emerges. While *MagNet*[®] allows different names to be attributed to different components in the simulation, it does not allow the surfaces on the components to be named. *MagNet*[®] automatically assigns names to all the surfaces on the components. When assigning boundary conditions, the surface that is being assigned is identified by its name.

In the optimisation process the geometry changes. In some cases *MagNet*[®] assigns a different name to some surfaces on some components. This creates a problem.

When the *Visual Basic*[®] simulation script assigns, for example "Stator, Face2" to "Boundary3", but that specific face has been assigned a different name. "Stator, Face2" is no longer on the same plane as "Boundary3" and *MagNet*[®] cannot interpret the command.

Luckily, *MagNet*[®] is fairly consistent in naming the faces on the geometry and a finite combination of face names exists. It is therefore possible to write a "try, catch" loop in the script that cycles through the known permutations until one is found where the correct names are used.

These permutations can only be found by trial and error. Unfortunately, as different designs are scripted, different geometries need to go through the same process to obtain all the different combinations of face names. This makes the optimisation process rather frustrating.

An optimisation can take weeks to achieve convergence. If for instance on the tenth day of optimisation a new combination of face names is found, that combination needs to be integrated into the *Visual Basic*[®] simulation script and the optimisation process has to begin again. It is likely, however, that a fairly good design will have been found in the optimisation

by then. Consequently when the optimisation is then restarted, good initial values can be chosen. The time is therefore not entirely wasted.

Mesh and Solve

The *Visual Basic*[®] simulation script needs to assign "mesh" values to the geometry. This process is represented by the Mesh and Solve block in Figure 3.2. The finite element method breaks the problem up into a number of smaller problems. The geometric model is divided into many tetrahedrons. These tetrahedrons are arranged in the shape of the holistic geometric model. This process is called "meshing". Each tetrahedron is solved analytically and the boundary condition information of each element is communicated to the next.

Defining the maximum length that any of the tetrahedrons' sides can be is a critical factor. Restricting the lengths to a very small value would increase the amount of tetrahedrons required to construct the simulation. This increases the accuracy of the numerical approximation but also increasing the computational time required to complete an evaluation. Relaxing the maximum allowable length decreases the computational time, but decreases the accuracy of the simulation. If the model accuracy becomes too low, numerical noise becomes a problem that adversely effects the optimisation routine.

This presents a challenge in the implementation of the optimisation. Sequential quadratic programming, as will be discussed in Chapter 4, is chosen as the optimisation algorithm that is used in this project. This optimisation algorithm performs a gradient analysis to determine the influence of change in the parameter vector values on the goal function and the constraint functions.

In practice, this means that a set of parameters is selected by the algorithm. From this point each of the parameters are individually changed in a separate evaluation to gauge their effect on the goal function and the constraint functions. The magnitude of the change in parameters for this gradient analysis is important to the optimisation algorithm. The smaller the change, the more accurately the sequential quadratic programming algorithm can approximate the optimisation problem.

The mesh and the gradient analysis step size are therefore two interdependent aspects of the optimisation. The step size has to be small enough to allow the algorithm to obtain a convergence and the mesh has to be small enough to accurately reflect the dimensional changes in a gradient analysis. This has to be implemented practically, so that the time required to obtain an optimum is minimal.

The goal function of the optimisation is to minimise the mass. The mass could be determined by calculating the sum of the mesh element volumes and multiplying the volumes by their respective densities. It is however found that in doing so, the goal function becomes the dominant agent in the mesh accuracy. This is due to the fact that the mesh need not be uniform throughout the model to accurately represent the electromechanical properties.

Certain areas in the machine require a high level of accuracy while other areas are less important. The mesh in the air-gap, for instance, is more important than the mesh in the coil. In determining the mass, however, all areas are equally important.

An analytical model is therefore required to calculate the mass as this reduces computational time by means of a more directed mesh control. The best directed mesh settings and function evaluation step sizes are determined by experimentally changing them and observing the effects.

The mesh settings presented an additional problem in the scripting process. *MagNet*[®] creates two different mesh volumes. One volume incorporates the stationary parts and the other volume incorporates the moving parts.

The volume containing the moving components need to go through the meshing process for every time step. The volume containing the stationary parts retain the original mesh throughout the simulation. This decreases the computational time required to perform an analysis.

A boundary between the stationary and moving volumes is created and nodes on this boundary communicate the information between the two volumes. However, in certain cases the geometry presents a meshing problem in one of the time steps where the nodes fail to connect the two volumes. When solving the finite element problem, *MagNet*[®] then returns an error.

Because of the possibility of a meshing error, the *Visual Basic*[®] simulation script incorporates its final "try, catch" loop. If this error is received, the script tries different mesh settings and reinitialises the solver routine.

Finally, the *Visual Basic*[®] simulation script retrieves the output information and communicates this information to the *Python* modelling script. *MagNet*[®] is then closed and the simulation script terminates.

3.3.4 Model Outputs

The results from a finite element simulation are simple numeric values. How these values relate to measurable characteristics of an electrical machine is the focus of this section.

The electrical machine model receives discrete values from the finite element simulation. In-order to create a model, a continuous curve is fit to these discrete values. This is done using the *Python spline* function. Differentiation and integration of these curves are done using the numerical *splev* and *splint* functions. The reason for this will become clear later in this section.

The first thing to be done is to scale the results to represent a full machine. As only one half of one coil is simulated, the simulated results that need to be scaled are multiplied by two times the amount of coils in the design.

Static Simulation Outputs

The static simulation is performed on one half of a time cycle. These results are "flipped" and "shifted", i.e. the second last value is multiplied by minus one and added to the end of the output array, then the third last etc. until a full cycle is represented.

In static simulation, the only loss mechanism that can be taken into account is that of the copper losses in the coils. As such, a fairly simple energy balance can be used to represent the outputs.

Elementary physics dictate that the mechanical power delivered to the linear alternator is a time dependent product of the force, f , and the velocity, \dot{x} . The instantaneous power integrated over a time period, T , can therefore be expressed as follows to represent the input mechanical power,

$$P_{in} = \frac{1}{T} \int_0^T f(t) \dot{x}(t) dt. \quad (3.3.8)$$

The voltage,

$$v_\lambda = \lambda \dot{x}, \quad (3.3.9)$$

induced in a conductor with length, l , moving at a relative velocity, \dot{x} , perpendicular to a magnetic flux, λ , is expressed by Faraday's law of electromagnetic induction. Naturally this is equally valid for the case of a stationary conductor with a magnetic field in motion as is the case in this "moving magnet" study.

The Lorentz Force,

$$f = \lambda i, \quad (3.3.10)$$

is similarly expressed as a function of the current, i , flowing in the conductor.

From the above, the instantaneous electromechanical relationship between the induced voltage and flowing current along with the velocity and force is expressed as

$$v_\lambda i = f \dot{x}. \quad (3.3.11)$$

It stands to reason that the input mechanical power can therefore be expressed as

$$P_{in} = \frac{1}{T} \int_0^T v_\lambda(t) i(t) dt. \quad (3.3.12)$$

The output electrical power, P_{out} , would then be the input mechanical power with all the different loss mechanisms, P_{loss} , subtracted from that.

From first principals, Faraday's law of electromagnetic induction, it is known that the induced voltage,

$$v_\lambda = N \frac{d\lambda}{dt}, \quad (3.3.13)$$

is a function of the variation in magnetic flux, λ , within an enclosed electrical winding with N turns.

The number of turns in the coils are taken as one throughout the optimisation process. The effect of a multitude of turns, equal current distribution, is taken into account within the simulation. At the construction phase, when a specific induced voltage magnitude is required, the number of turns can be chosen. This can easily be done when the physical dimensions of the coils are known. It simplifies the simulation and optimisation process, however, to use a single turn equivalent coil until the construction phase is reached.

The magnetic flux-linkage, λ , is composed out of two components. Flux resulting from the permanent magnets and electromagnetic flux resulting from the driven current in the coils. Analytical models employed by Cosic [33] and Boldea [23], approximates the resulting magnetic flux as the sum of these two components. Finite element based software, however, take the non-linearities within the electric steel's magnetic saturation into account when calculating the resulting magnetic flux.

It should be noted that the voltage, v_λ , that is derived from the magnetic flux-linkage, λ , takes the inductance of the machine into account, as one of the contributing components of the magnetic flux-linkage is that of the coils. When the generator operates in a "no-load" state, magnetic flux-linkage across the coils is only that of the permanent magnets and the voltage derived from the flux-linkage in this state is the electromotive force voltage. Figure 3.4 shows the equivalent circuit diagram of the electrical machine.

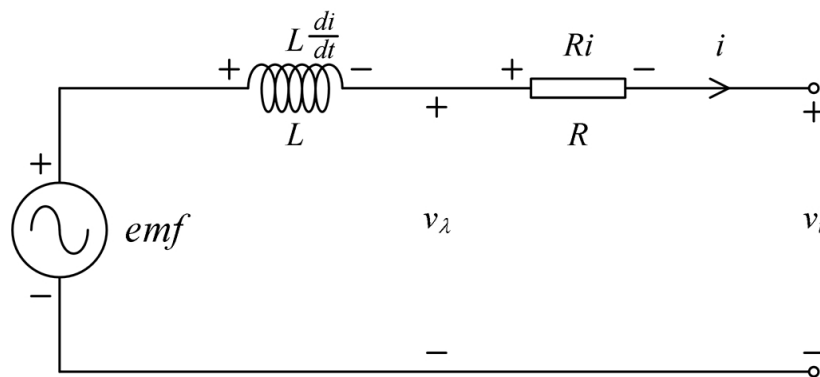


Figure 3.4: Equivalent circuit diagram of the electrical machine.

Under normal operating conditions, with the flux-linkage obtained from the finite element software and the driven current known, the mechanical input power, P_{in} , can be

calculated from Equation 3.3.12.

From the geometry of the machine, the resistance is calculated by the *Visual Basic* simulation script. The terminal voltage, v_t , can now be calculated as

$$v_t(t) = v_\lambda(t) - Ri(t). \quad (3.3.14)$$

It is true that *MagNet*[®] provides the terminal voltage. It was found, however, that the voltage produced by *MagNet*[®] is inaccurate.

While reviewing the simulation output data from *MagNet*[®], it was consistently found that there was an unexplained phase-shift in the voltage.

The voltage is derived from the flux-linkage, as shown in Equation 3.3.13. Under no-load conditions, the electromotive force voltage resulting from a sinusoidal motion profile, should be 90° out of phase with the flux-linkage.

The voltage provided by *MagNet*[®], was however not exactly 90° out of phase. This error was investigated. After reviewing different aspects of the simulation set-up, the reason for this erroneous phase-shift was found.

The flux-linkage values for the no-load conditions were exported and from these values the voltage was derived using two different methods. One was a simple forward difference method,

$$v_\lambda(i) = \frac{\lambda(i) - \lambda(i-1)}{i}. \quad (3.3.15)$$

The other was done using the *Python spline* curve fit and to get the derivative of the flux-linkage, the *splev* function was used. The results from these two methods were plotted, along with the voltage values received from *MagNet*[®].

Figure 3.5 shows the results. From this figure, it can be seen that *MagNet*[®] uses a forwards difference method to derive the voltage and this is the reason for the phase shift.

It is assumed that *MagNet*[®] does so because this is a very simple technique to obtain a voltage. As such it must be a stable and robust method of doing so. In the case of this study, however, it causes an error. For this reason, the voltage used in the *Python* modelling script is derived using the *spline* and *splev* functions instead of using the voltage provided by *MagNet*.

The electrical output power, P_{out} , is expressed as

$$P_{out} = \frac{1}{T} \int_0^T v_t(t) i(t) dt. \quad (3.3.16)$$

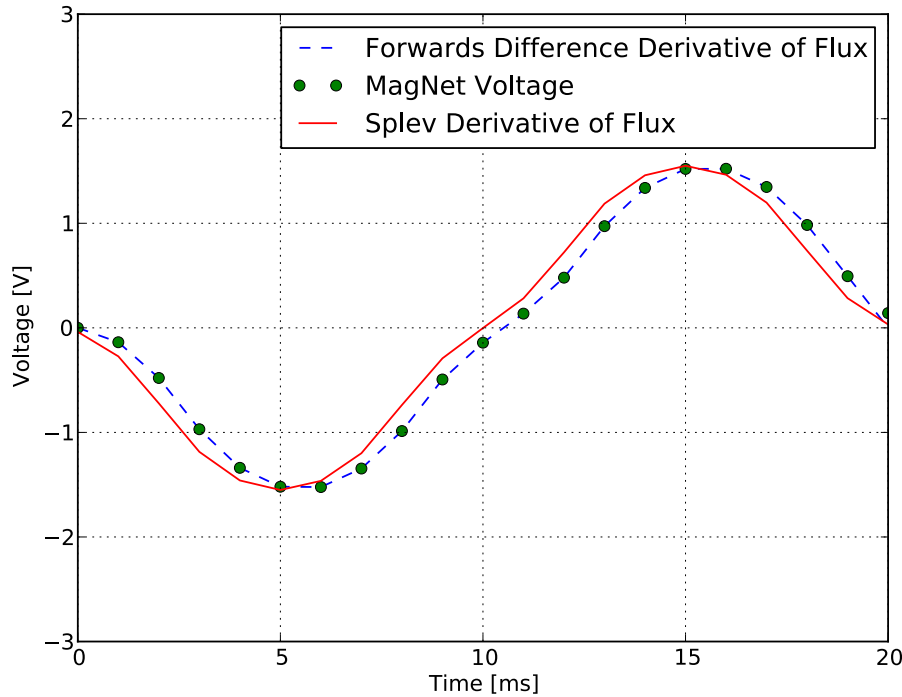


Figure 3.5: No-load Voltage Derived Using Different Techniques

The efficiency, η , of the generator can now be calculated as

$$\eta = \frac{P_{out}}{P_{in}}. \quad (3.3.17)$$

3.3.4.1 Transient Simulation Outputs

As the transient simulation is performed over more than a full time cycle to account for the start-up transients, the valid simulation output data is selected to construct a single full time cycle. In transient simulations, the energy balance becomes more complex, because there are many different loss mechanisms. The energy balance established by *MagNet*[®] needs to be used in post-processing.

The resultant flux-linkage, λ , obtained from the simulation package is a function of both the electromagnetic field caused by the current in the coils and the permanent magnets of the translator. The single turn equivalent voltage, v_λ , induced within the coils due to a variation of this flux-linkage is calculated as follows, namely

$$v_\lambda = \frac{d\lambda}{dt}. \quad (3.3.18)$$

With this voltage known, the related power, P_λ , can be calculated with

$$P_\lambda = \frac{1}{T} \int_0^T v_\lambda(t) i(t) dt. \quad (3.3.19)$$

The mechanical input power, P_{mech} , is similarly calculated from the translator velocity, \dot{x} , and the force in the direction of translator motion, f as obtained from the simulation by

$$P_{mech} = \frac{1}{T} \int_0^T f(t) \dot{x}(t) dt. \quad (3.3.20)$$

Ohmic losses in the magnets due to eddy currents are taken into account by the simulation package during the transient simulation process and can be obtained from the difference between P_{mech} and P_λ , i.e.

$$P_{loss_{magnets}} = P_{mech} - P_\lambda. \quad (3.3.21)$$

This is known to be true because *MagNet*[®] also provides the ohmic losses in the magnets as a simulation output. The simulation output ohmic magnet losses and the ohmic losses calculated from Equation 3.3.21 were compared and shown to be equal.

In the case where a stainless steel shaft on which the magnets will be mounted is taken into account during the optimisation process, the ohmic losses also account for such losses in the shaft.

Copper losses in the coils as a function of time are also simulated by *MagNet*[®]. The average copper losses, taking into account a copper fill factor of k_{fill} throughout, may therefore be calculated as

$$P_{loss_{copper}} = \frac{1}{k_{fill}} \frac{1}{T} \int_0^T p_{copper}(t) dt. \quad (3.3.22)$$

The total output power, P_{out} may now be calculated with

$$P_{out} = P_\lambda - P_{loss_{copper}}, \quad (3.3.23)$$

where the eddy current losses ($P_{loss_{eddy}}$) and hysteresis losses ($P_{loss_{hyst}}$) in the laminated silicon-steel core may also be retrieved from *MagNet*[®]. These losses are however calculated as single values after the transient simulations. The inclusion of these losses to determine the efficiency of the linear generator could be either to further subtract from the output power or to add these to the input power. The latter possibility was chosen, and the total input power is calculated with

$$P_{in} = P_{mech} + P_{loss_{eddy}} + P_{loss_{hyst}}. \quad (3.3.24)$$

It was chosen to add these losses to the input power rather than subtracting them from the output power, because of the optimisation algorithm. In optimisation, a machine configuration might be simulated where almost no power is delivered. In such a case, if the losses were to be subtracted from the output power, a nonsensical result could be obtained with a negative value for the output power. This risk is reduced by adding these losses to the input power instead.

From the energy balance, it is observed that the output power can be obtained in two different manners. Either by calculating it from the forces, or by calculating it from the flux-linkage. Comparing these two values was one of the measures used to determine the mesh settings.

In optimisation, when the difference between these two values becomes greater than one percent, the smaller of the two values is selected as the output power. In practice, this condition is almost never applied as the values are almost always within the one percent margin and consequently the value calculated from the flux-linkage is almost always used. The exceptions to this all occur in strange machine configurations where there is close to no power output.

Finally, the efficiency of the linear generator is calculated by

$$\eta = \frac{P_{out}}{P_{in}}. \quad (3.3.25)$$

Mass Calculation

The most important model output is the goal function of the optimisation. This is the mass of the machine. It is mentioned earlier that the mass is calculated analytically.

The analytical mass calculations provide a challenge. This is because the analytical calculations must remain within the real defined domain for all possible combinations of dimensions.

The analytical model can not have any duality, i.e. the use of parametric equations are disqualified. Care should therefore be taken with the use of trigonometric functions, to remain within the defined domain and to avoid a zero-division.

The final analytical calculations were compared to values obtained by drawing the machine in *Autodesk Inventor*[®]. When the analytical calculations corresponded to the *Inventor*[®] results within the ninth significant number (the highest accuracy that *Inventor*[®] can provide), it was assumed that the analytical calculations were accurate.

3.4 Conclusive Remarks

In this chapter, the different types of mathematical simulation approaches were evaluated. It was decided to proceed with the numerical simulation technique of a three-dimensional finite element method.

The integration of this simulation technique into a representative mathematical model of the electrical machine was then shown. This integration involves the writing automated scripts to facilitate the simulation software *MagNet*[®].

Chapter 4

A Machine Optimisation Approach

4.1 Overview

In this chapter the optimisation approach used for optimisation of the linear electric machines is discussed. This includes the practical implementation of this approach.

In Section 4.2, the goal of the optimisation process is described. The different methods of obtaining this goal are then evaluated in Section 4.3 and the motivation for the chosen path is provided. The basic mathematical operation of the chosen optimisation algorithm is described in Section 4.4.

4.2 Optimisation Goal

The purpose of the optimisation is to facilitate the conception of a good design. Optimisation is a single tool amongst many that is used in the design process. The focus of the optimisation is therefore not to produce a mathematically perfect representation of the design environment but rather to highlight the strengths and weaknesses that different configurations have. With comparative information on the performance of different design configurations, an attempt to contribute to the development of the linear electric machine technology can be made. It is from this perspective that the optimisation process was implemented.

The electric machines in Stirling engines are too big [14]. The electric machine serves two purposes in Stirling engines. The primary function is to convert the mechanical energy into electrical energy. The secondary function is to provide a control mechanism to regulate piston motion.

A design environment should be created with flexibility in mind. The goal of the optimisation might change in future. At some point the different aspects of the entire Stirling engine system design is envisioned to be integrated with one another. At this later stage, the force profile of the translator (affixed to the power piston) will certainly have to conform to a desired force profile to better control piston motion.

At this stage however, every measure that the optimisation procedure follows must be focused on making the electrical machine smaller as overly large electrical machines is the specific reason given for the failure of previous free-piston Stirling engine projects [14].

A quantifiable performance measure needs to be chosen so that one set of parameters can be compared to another set of parameters. In this study, the electromagnetically active mass is chosen as this measure.

The required output power and efficiency is established along with the operating conditions. The machine that meets the established requirements within these conditions, with the lowest electromagnetically active mass, is deemed the best design.

By defining the stroke length and the operating frequency as constants and restricting the output power to be above a chosen value at a chosen efficiency, the mechanical input is inherently defined. Mechanical energy is converted into electrical energy as a function of the force and velocity of the translator. If the stroke length and operating frequency are constants, the velocity becomes fixed and the work derived from the force and fixed velocity is defined from the power and efficiency constraints. In such a defined system it is then proposed to minimise the mass as the goal function.

As the generator is intended for use in a free-piston Stirling engine, the volume is very important. As previously mentioned, free-piston Stirling engines are hermetically sealed. The smaller the volume of the electric generator, the smaller the pressure vessel needs to be that contains it. Volume could therefore have been chosen as the goal. However, the density of the materials used in the generator are relatively comparable. As such, using the volume as the goal function and using the mass as the goal function should yield relatively comparable results. The mass is however easier to verify experimentally than the volume so it was finally decided to use the mass as the goal function.

It is certainly true that any electrical machine design intended for a commercial market needs to be economically viable. Such a machine needs to take the cost of manufacture into account. The magnetic materials used in a permanent magnet machine is generally the most expensive component. Designing for a market would have to take this into account.

This specific machine is not at that stage in development. The best configuration of copper, steel and magnetic material still needs to be established. Once this is done, the components can be restricted to adhere to the market but until that stage, minimising the active mass remains the goal of optimisation.

4.3 Optimisation Algorithms

4.3.1 Types of Optimisation Algorithms

There are many different algorithms that can be used in an optimisation. In this section the strengths and weaknesses of the single goal algorithms generally used in engineering applications [35] are evaluated. This is only a very narrow aspect of optimisation, specifically relevant for this application. Two general categories of optimisation algorithms exist in this regard, namely heuristic algorithms described in Section 4.3.2 and meta-heuristic algorithms described in Section 4.3.3.

4.3.2 Heuristic Optimisation Algorithms

Often called "local" optimisation algorithms, these optimisations generally follow a gradient-based approach. A design point is evaluated by performing function evaluations. These function evaluations provide gradient information regarding the design point. Based on this gradient information a new design point is chosen that improves the goal function and the process is repeated. New design points are chosen in this manner until no more progress can be made and convergence is accomplished.

These techniques generally require relatively few function evaluations to obtain a convergence and as such they are computationally efficient. They can also solve problems with a large number of design variables. Upon implementation, they generally require little problem-specific tuning.

Heuristic algorithms are however susceptible to convergence on local, sub-optimum points and they struggle with discrete problems where variables can only be natural numbers (such as the amount of coils in an electrical machine, for example). They are susceptible to numerical noise as this taints the gradient information and they are complex algorithms that are difficult to implement efficiently [35].

4.3.3 Meta-heuristic Optimisation Algorithms

Often called "global" optimisation algorithms, the most commonly used global algorithms are classified as evolutionary algorithms. Unlike heuristic algorithms, evolutionary algorithms do not require gradient information but rather use a set of design points often referred to as a population.

The design points are ranked according to the goal function. Random combinations of characteristics from the highest ranked design points are incorporated into the next generation of design points, creating a new population. This is repeated until there is no longer a noticeable difference between consecutive generations.

These methods are robust and have an increased chance of finding a global optimum. They are easy to implement and well suited to discrete problems.

Drawbacks of global algorithms are that they require a large amount of function evaluations and are consequently expensive to implement in terms of computational time. They are limited in terms of the number of design variables and have poor constraint handling capabilities [35].

4.4 Sequential Quadratic Programming

It is important to note that no algorithm can guarantee a global optimum [35]. Meta-heuristic algorithms have a higher likelihood to do so than heuristic algorithms, but the cost of this probability is a much higher amount of function evaluations.

Since it has been established that function evaluations are to be performed by a three dimensional finite element analysis, meta-heuristic algorithms are deemed impractical. Meta-heuristic algorithms will simply take too long to reach convergence.

Venter recommends that global methods should only be considered in cases where local methods are not viable and further, that mathematical theoreticians consider sequential quadratic programming to be an excellent technique for solving constrained, non-linear problems [35].

Schittkowski and Yuan [36] state that sequential quadratic programming is currently the standard method in both academia and industry for solving complex application problems. In light of these recommendations the choice was made to proceed with the local, sequential quadratic programming technique.

A brief overview of the structure of gradient based optimisation follows. The purpose of this overview is not to comprehensively evaluate the mathematical process but rather to explain the function of some routines. At the end of the section, the specific structure of sequential quadratic programming is briefly evaluated.

4.4.1 General Structure of Optimisation

In essence, the definition of a non-linear constrained optimisation problem, as evaluated by Vanderplaats [37], is as follows. Using \vec{P} , the parameter vector

$$\vec{P} = \begin{bmatrix} p_1 \\ p_2 \\ \cdot \\ \cdot \\ \cdot \\ p_n \end{bmatrix}, \quad (4.4.1)$$

minimise the objective function

$$F(\vec{P}), \quad (4.4.2)$$

subject to the inequality constraints

$$g_j(\vec{P}) \leq 0; \quad j = 1, 2, \dots, m, \quad (4.4.3)$$

the equality constraints

$$h_k(\vec{P}) = 0; \quad k = 1, 2, \dots, l, \quad (4.4.4)$$

and the upper and lower side constraints,

$$p_i^l \leq p_i \leq p_i^u; \quad i = 1, 2, \dots, n. \quad (4.4.5)$$

An iterative procedure is followed, i.e.

$$\vec{P}^q = \vec{P}^{q-1} + \alpha^* \vec{S}^q, \quad (4.4.6)$$

until such time as convergence is obtained, with q denoting the iteration and α^* , a scalar quantity denoting a "distance" to be moved in "direction", \vec{S} . Note that as $\alpha^* \vec{S}^q$ is a propagation on \vec{P} , this can therefore also be written as

$$\vec{P}^q = \vec{P}^{q-1} + \delta \vec{P}. \quad (4.4.7)$$

4.4.2 Criteria of Convergence

The Tucker-Kuhn conditions mathematically define what is to be considered as an optimum. There are three conditions.

The first is obvious. The design point \vec{P}^* must be feasible. The design must lie within the bounded design space.

The second condition states that if the constraint, $g_j(\vec{P})$, is not satisfied, the Lagrangian multiplier, τ_j must be zero. The Lagrangian is the function that describes the dynamics of a problem and the Lagrangian multipliers are the medium by which the dynamics are described, i.e.

$$\tau_j g_j(\vec{P}^*) = 0; \quad j = 1, 2, \dots, m; \quad \tau_j \geq 0. \quad (4.4.8)$$

The third condition defines the vanishing gradient of the Lagrangian, i.e.

$$\nabla F(\vec{P}^*) + \sum_{j=1}^m \tau_j \nabla g_j(P^*) + \sum_{k=1}^l \tau_{m+k} \nabla h_k(\vec{P}^*) = 0, \quad (4.4.9)$$

with

$$\tau_j \geq 0, \quad (4.4.10)$$

and with τ_{m+k} unrestricted in sign. Equation 4.4.9 states that the gradient vanishes at the optimum.

The significance of the Kuhn-Tucker conditions are best illustrated using a graphic representation. Consider Figure 4.1. In this graphic representation a two parameter problem is shown. The constraints, g_1 , g_2 and g_3 are shaded in the in-feasible region and contour lines indicate discrete values of the goal function.

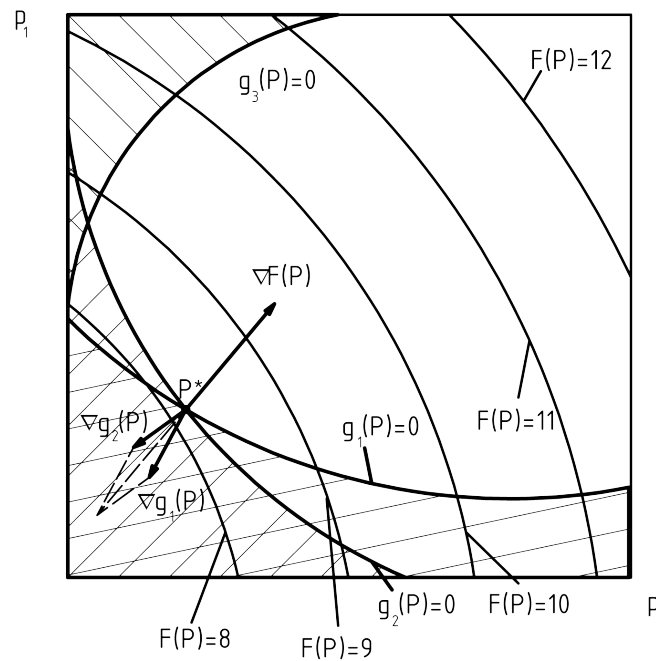


Figure 4.1: Kuhn-Tucker convergence conditions.

From this figure it can be seen that \vec{P}^* is feasible so the first condition is met. It can further be observed that the constraint, $g_3(\vec{P}^*)$, is not critical and therefore from Equation 4.4.8, the second condition applies here such that $\tau_3 = 0$. In the case of the other two constraints, $g_1(\vec{P}^*) = 0$ and $g_2(\vec{P}^*) = 0$ also satisfies the second condition. This is because \vec{P}^* lies on these two boundaries.

Now, Equation 4.4.9 states that the sum of the gradient of each active constraint, mul-

multiplied by its respective Lagrangian multiplier, should equal the negative of the objective function's gradient, i.e.

$$\nabla F(\vec{P}^*) + \tau_1 \nabla g_1(\vec{P}^*) + \tau_2 \nabla g_2(\vec{P}^*) = 0, \quad (4.4.11)$$

where

$$\tau_1 \geq 0; \tau_2 \geq 0. \quad (4.4.12)$$

So for Figure 4.1, the Kuhn-Tucker conditions are satisfied, defining an optimum.

4.4.3 Calculating the Lagrangian Multipliers

Now the Lagrangian multipliers can be calculated. It is known that if a constraint value is non-zero, the Lagrangian multiplier is equal to zero. In this regard both equality and inequality constraints are the same, so they can be treated in the same way. This can be done if it is taken into consideration that equality constraints will always be active at an optimum. That is, at an optimum, \vec{P}^* must lie on an equality constraint.

It is therefore possible to rewrite Equation 4.4.9, namely,

$$\nabla F(\vec{P}^*) + \sum_{j=1}^m \tau_j \nabla g_j(\vec{P}^*) = \vec{R}, \quad (4.4.13)$$

where \vec{R} denotes a vector of the residuals. This is because the Kuhn-Tucker conditions may not be precisely reached. Rather then, the residuals must be as small as possible so \vec{R} must therefore be minimised. If the components of \vec{R} all equal zero, the Kuhn-Tucker conditions are precisely met. In strife of this, the square of the magnitude of \vec{R} is minimised. Let

$$D = \nabla F(\vec{P}^*) \quad (4.4.14)$$

and

$$A = [\nabla g_1(\vec{P}^*) \nabla g_2(\vec{P}^*) \dots \nabla g_M(\vec{P}^*)], \quad (4.4.15)$$

where M denotes the number of active constraints. Equation 4.4.13 is redefined using Equations 4.4.14 and 4.4.15 such that

$$D + A\tau = \vec{R}. \quad (4.4.16)$$

The square of the magnitude of the residuals given by

$$\vec{R}^T \vec{R} = D^T D + 2\tau^T A^T D + \tau^T A^T A \tau, \quad (4.4.17)$$

is minimised by differentiating Equation 4.4.17 with regard to τ and choosing a result of zero yield

$$2A^T D + 2A^T A \tau = 0. \quad (4.4.18)$$

Therefore, τ is defined as

$$\tau = -[A^T A]^{-1} A^T D \quad (4.4.19)$$

and the residuals are calculated. If the residuals approach zero, an optimum is defined.

4.4.4 Sequential Quadratic Programming Structure

The broad concepts of a gradient based, bounded optimisation are now established. The structure of sequential quadratic programming can therefore be explained.

The purpose of this evaluation is not to investigate the intricacies of the algorithm, that is a complex field of study in its own right. Rather, an overview of the structure is given with the purpose of illustrating why this specific algorithm is chosen to facilitate the optimisation of the design described in this thesis.

Firstly, the search direction is defined by

$$Q(\vec{S}) = F(\vec{P}) + \nabla F(\vec{P})^T \vec{S} + \frac{1}{2} \vec{S}^T B \vec{S}. \quad (4.4.20)$$

This is an auxiliary function. It is a quadratic approximation to the goal function. A linear approximation to the constraint functions bound this approximated goal with

$$\nabla g_j(\vec{P})^T \vec{S} + \delta_j g_j(\vec{P}) \leq 0; \quad j = 1, 2, \dots, m, \quad (4.4.21)$$

and

$$\nabla h_k(\vec{P})^T \vec{S} + \bar{\delta} h_k(\vec{P}) = 0; \quad k = 1, 2, \dots, l. \quad (4.4.22)$$

Equation 4.4.20 forms the core of what distinguishes sequential quadratic programming from other algorithms. This auxiliary function is not the regular goal function as is the case for most other algorithms, it is a quadratic approximation to the goal function defined as a search direction. Sequential quadratic programming minimises this search direction, it does not minimise the goal function itself.

It should be noted, that the quadratic approximation to the goal function and the linear approximation to the constraints are analytical functions. They are based on numerical information, but the functions themselves are analytical.

In Equation 4.4.20, B is initially defined as an identity matrix. This matrix will be subsequently updated and as it approach the Hessian matrix of the Lagrangian an optimum is defined.

For the linear constraint functions, Equations 4.4.21 and 4.4.21, the design variables are the components of \vec{S} . The variables, δ_j and $\bar{\delta}$ are scalars used to prevent inconsistencies in linearised constraints. These variables are given by

$$\delta_j = 1 \text{ if } g_j(\vec{P}) < 0, \quad (4.4.23)$$

and

$$\delta_j = \bar{\delta} \text{ if } g_j(\vec{P}) \geq 0 \quad (4.4.24)$$

with

$$0 \leq \bar{\delta} \leq 1. \quad (4.4.25)$$

With the search direction \vec{S} determined by the auxiliary function, the analytical one-dimensional search problem is solved using the exterior penalty function, ϕ . This relates to the "distance" moved in direction \vec{S} . This is defined from

$$\phi = F(\vec{P}) + \sum_{j=1}^m u_j \{ \max[0, g_j(\vec{P})] \} + \sum_{k=1}^l u_{m+k} |h_k(\vec{P})|. \quad (4.4.26)$$

with

$$\vec{P} = \vec{P}^{q-1} + \alpha \vec{S}, \quad (4.4.27)$$

and

$$u_j = |\tau_j|; \quad j = 1, 2, \dots, m + l \quad (4.4.28)$$

for the first iteration and

$$u_j = \max[|\tau_j|, \frac{1}{2}(u'_j + |\tau_j|)] \quad (4.4.29)$$

for the subsequent iterations while using $u'_j = u_j$ from the previous iteration. Solving the one-dimensional search problem by minimising ϕ , produces α . The design point can then

be updated with Equation 4.4.27. Note here that sequential quadratic programming differs from the norm, where the residuals would have been minimised, as was done in Section 4.4.3. That is, in sequential quadratic programming, ϕ is minimised, not $\vec{R}^T \vec{R}$.

With the updated design point, $Q(\vec{S})$ is calculated once more, using an updated matrix, B . Powell [38], recommends that B should be updated using the Broyden-Fletcher-Shanno-Goldfarb update formula. Recall that B needs to approach the Hessian of the Lagrangian to define an optimum. B is therefore updated as

$$B^* = B - \frac{B \vec{c} \vec{c}^T B}{\vec{c}^T B \vec{c}} + \frac{\gamma \gamma^T}{\vec{c}^T \gamma}. \quad (4.4.30)$$

The components of this update formula are

$$\vec{c} = \vec{P}^q - \vec{P}^{q-1}, \quad (4.4.31)$$

$$\gamma = \theta y + (1 - \theta) B \vec{c}, \quad (4.4.32)$$

$$y = \nabla_p \Phi(\vec{P}^q, \tau^q) - \nabla_p \Phi(\vec{P}^{q-1}, \tau^{q-1}), \quad (4.4.33)$$

$$\Phi(\vec{P}, \tau) = F(\vec{P}) + \sum_{j=1}^m \tau_j g_j(\vec{P}) + \sum_{k=1}^l \tau_{m+k} |h_k(\vec{P})|, \quad (4.4.34)$$

$$\theta = 1; \text{ if } \vec{c}^T y \geq 0, 2 \vec{c}^T B \vec{c} \quad (4.4.35)$$

and

$$\theta = \frac{0,8 \vec{c}^T B \vec{c}}{\vec{c}^T B \vec{c} - \vec{c}^T y}; \text{ if } \vec{c}^T y < 0, 2 \vec{c}^T B \vec{c}. \quad (4.4.36)$$

Conclusively then, the Lagrangian is approximated. This approximation is then minimised. Since this approximation is done with regards to the variables, \vec{P} alone, the minimisation sub-problem uses linear approximations to the constraints and the result is used as a search direction. This search direction minimises the augmented Lagrangian. The formula used to update B , is a variable metric method because positive definiteness is used [37]. An optimum is defined when B approximates the Hessian of the Lagrangian. This structured process of the algorithm is given in Figure 4.2.

This evaluation of sequential quadratic programming is not an in-depth study of the mathematics. From this broad overview, it is however possible to consider its application in this specific design problem.

The dominant reason why sequential quadratic programming is chosen above other algorithms, is because of the fact that it approximates the goal function quadratically and optimises the search direction with linear approximations to the constraint functions.

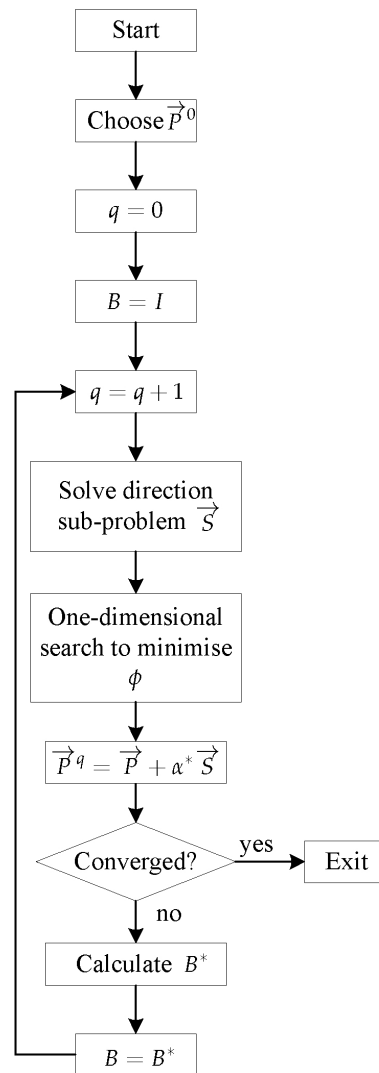


Figure 4.2: Structure of the sequential quadratic programming algorithm.

Recall that the goal function in this case is the analytically calculated mass. This goal function is calculated directly from the optimisation parameters. It stands to reason that the quadratic approximation to this goal function is free of numerical noise and consequently very accurate.

As the search direction is optimised, sequential quadratic programming should drive the optimisation to a minimal mass point with very few iterations. The problematic aspect of the optimisation is the constraints. The constraint in the case of a static optimisation is the output power. In the case of a transient optimisation the constraints are the output power and the efficiency. These constraints are susceptible to numerical noise and computationally expensive to calculate.

The use of sequential quadratic programming is considered to be the most time efficient approach in comparison to other approaches. No time is wasted in obtaining a minimal

mass point and the computationally expensive constraint functions are evaluated in regions determined by the accurately calculated goal function. Other algorithms that do not optimise the search direction, might waste time by evaluating the constraint functions in regions that are unimportant. The choice of this algorithm is therefore based on exploiting the fact that the mass can be calculated analytically to the best possible advantage of the project.

One drawback of sequential quadratic programming is that it can struggle to find the true optimum. The goal function is never minimised, only the augmented auxiliary function that defines the search direction is minimised. Because of this a near-optimum point is found very quickly, but as soon as the design point reaches a near optimum, the search direction minimisation problem converges. This can occur at a design point where the actual goal function can still be slightly minimised. Generally, however, this is close enough to the true optimum that it does not make much of a difference.

4.5 Implementation

4.5.1 Overview

The predominant problem regarding optimisation in this project is stability. In this optimisation approach, the structure of the algorithm is specifically written to be as stable as possible. This results in a complex, fractured structure. The structure incorporates many beak-points where subroutines can fail and terminate without inhibiting the overall optimisation process.

A secondary reason for the complex structure relates to communication protocols and available resources. *Infolytica*[®], the company that provides the simulation software, *MagNet*[®], has well documented tutorials and customer support for a scripting interface. The software language that the support structure is based in, is *Microsoft*[®] *Visual Basic*[®]. *MagNet*[®] also has a 64 bit architecture.

A resource that was made available to this project, is a scripted communication interface that communicates between *Python* and the optimisation software, *Visual Studio*[®] by *Vrand*[®]. This interface was written by Prof Gerhard Venter and Richard Hamman. *Visual Studio*[®] has a 32 bit architecture.

The purpose of the structure is to facilitate communication between the 64 bit simulation software, *MagNet*[®] and the 32 bit optimisation software, *Visual Studio*[®]. In-order to do this, the structure consists of two sections. One section has a 32 bit architecture and the other section has a 64 bit architecture. The communication structure is comprised out of six components. Four components are software scripts and two components are file locations.

Figure 4.3 shows these six communication components. In Figure 4.3 an additional file location is shown. This file location is an output data file location. By checking the data file

written to this location, the optimisation can be monitored.

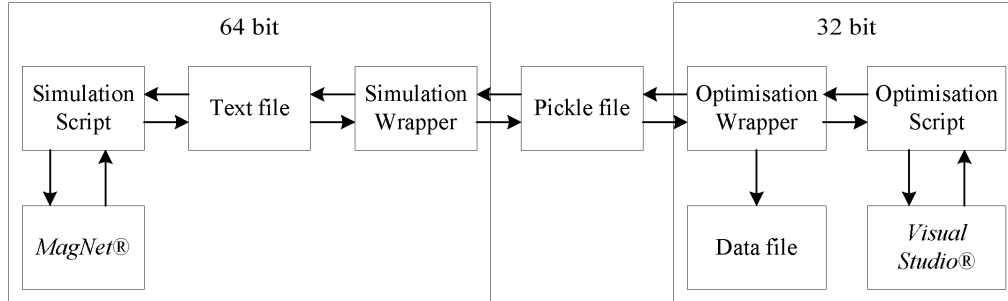


Figure 4.3: Communication structure in optimisation.

The first software component to be discussed is the Optimisation Wrapper. This is discussed in Section 4.5.2. The Optimisation Script is then discussed in Section 4.5.3. This is followed by a discussion on the Simulation Wrapper, in Section 4.5.4. The Simulation Script is discussed in Section 4.5.5.

4.5.2 Optimisation Wrapper

Figure 4.4 shows the detailed structure of the optimisation. In this figure, the Optimisation Wrapper is outlined in red. There are eight processes in the Optimisation Wrapper. The optimisation is written and compiled in a 32 bit version of *Python*.

Define Constants

In this process, a library is created that contains information that remains constant throughout the optimisation. The constants defined in this library are shown in Table 4.1.

Table 4.1: Constants defined in the library of the Optimisation Wrapper.

Constant
stroke length
frequency
air-gap distance
copper resistivity
coil fill factor
number of coils
copper density
magnet density
steel density
simulation time steps

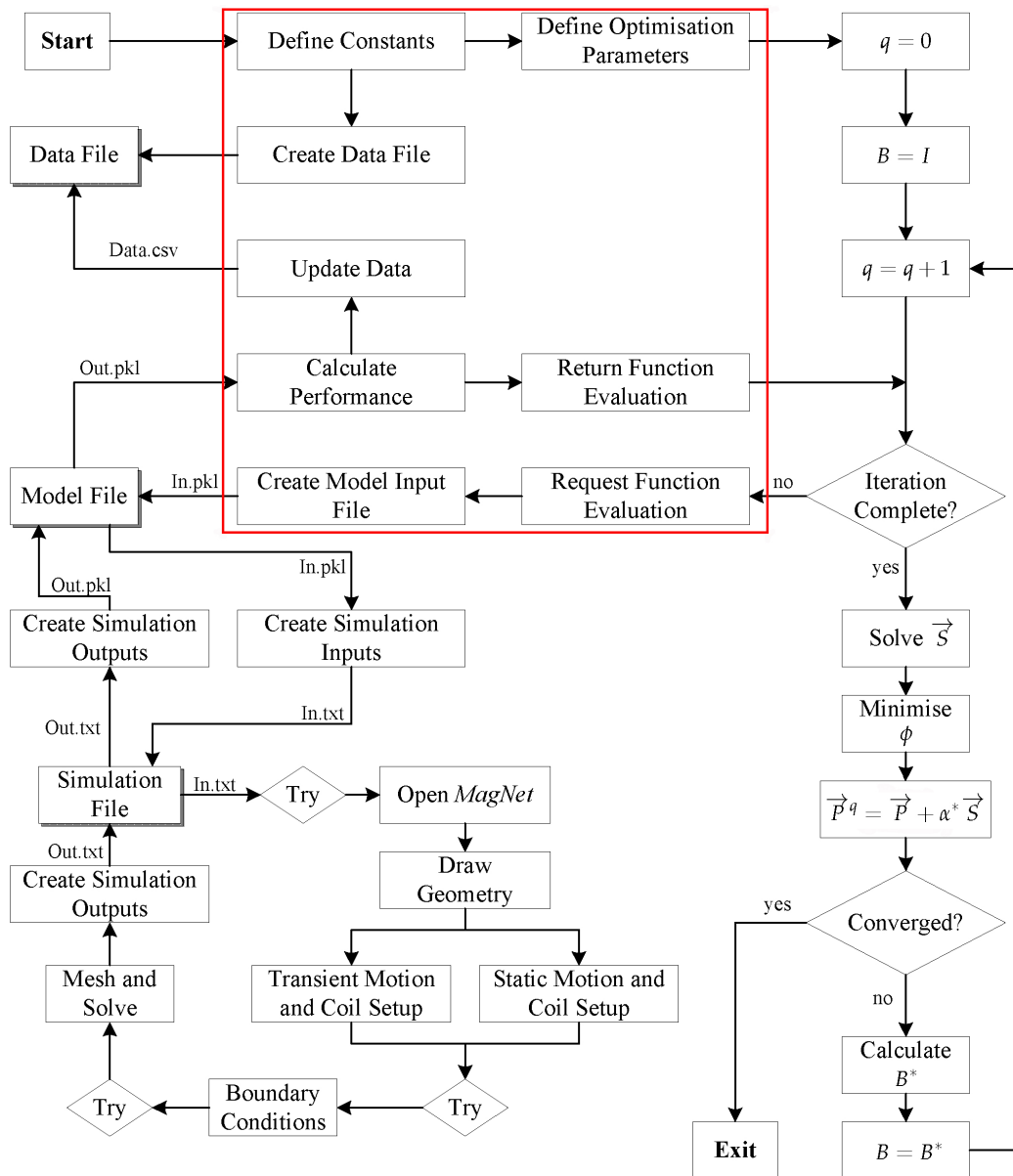


Figure 4.4: Optimisation Wrapper within the optimisation structure.

Create Data File

A file is created in this process. This file is created in the Data File location shown in Figure 4.4 to the left of the red outlined area.

The file is a .csv (comma separated variable) file. When this file is created, the headings for columns are written. The headings describe the output data that is to be written in the columns.

Define Optimisation Parameters

In this process, the optimisation parameters are created. The optimisation parameters are then used in the initialisation of the Optimisation Script. The parameters that are created and communicated to the Optimisation Script are discussed in Section 4.5.3.

The processes described up to this point are only performed once during initialisation. The next five processes are performed for each function evaluation.

Request Function Evaluation

In this process, the Optimisation Script requests information. The information requested pertains to the performance of a set of optimisation parameters, \vec{P} .

The information contained within \vec{P} is an array. Some of the values in this array are dimensional variables that need to be converted into lengths in millimetres or angles in degrees. In a transient optimisation, one of the variables needs to be scaled to represent the driven current amplitude.

Create Input File

As a function evaluation has been requested, this function evaluation needs to be performed. But there is a communication protocol problem that needs to be addressed first. The requested information is in 32 bit format. The software that performs the function evaluations however, has a 64 bit architecture.

The solution to the problem is to create and write an output file. The output file is a .pkl (pickle) file. This file can be read and written correctly by both 32 bit and 64 bit architecture programs. The file is created in the Model File location. The file is named "In.pkl".

Another reason taking this route is related to stability. Writing this information to a file creates a break point.

The Optimisation Wrapper will now constantly watch the Model File location will wait until this file is changed. Anything that happens down the line will not effect the Optimisation Wrapper as the wrapper will only respond when the pickle file in the Model File location is changed.

Calculate Performance

The Calculate Performance process is initiated when the pickle file in the Model File location is changed. The pickle file was changed and is now named "Out.pkl".

The information contained within the "out.pkl" file is read in this process. From the information, the performance of the function evaluation requested in the Request Function

Evaluation process is calculated. The performance is calculated in the manner already described in Section 3.3.4.

Update Data

The optimisation information received in the Request Function Evaluation process and the results generated in the Calculate Performance process can now be written to the Data File location. This is what happens in the Update Data process. The information that is written to the Data File location is shown in Table 4.2.

Table 4.2: Data written to the Data File location in the Update Data process.

Optimisation Parameter
p_1
p_2
.
.
.
p_n
Performance Measure
total mass
steel mass
copper mass
magnet mass
input power
losses
output power
efficiency
current density

Return Function Evaluation

The final process in the Optimisation Wrapper is to convert the output data into a format that the Optimisation Script can understand and to then communicate this information to the Optimisation Script. This is the purpose of the Return Function Evaluation process.

4.5.3 Optimisation Script

The Optimisation script facilitates direct communication with the optimisation software, *Visual Studio*[®]. Figure 4.5 shows the processes that the software performs outlined in red.

The process describes a sequential quadratic programming algorithm as has already been described in Section 4.4.

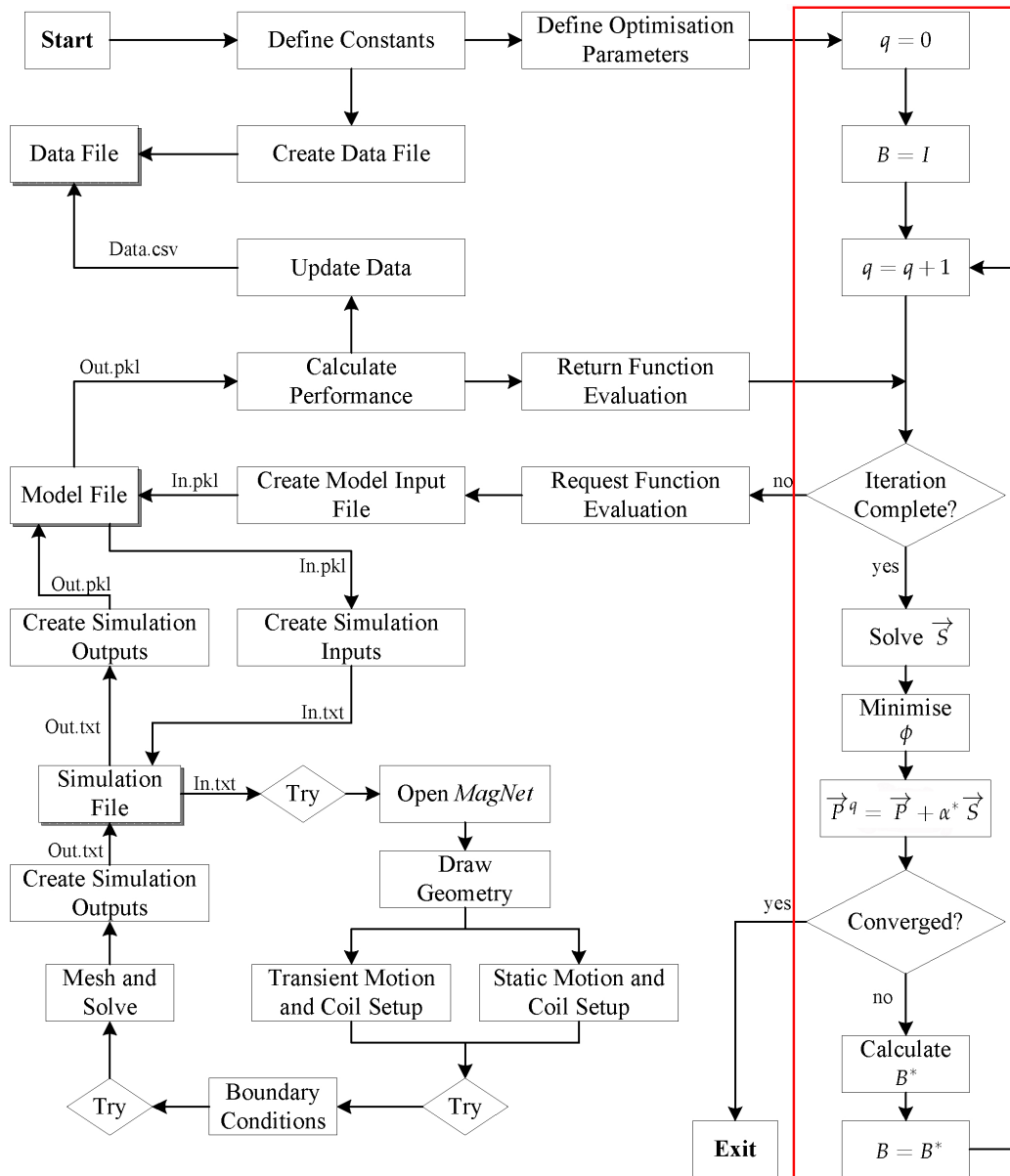


Figure 4.5: Optimisation Script within the optimisation structure.

In this section, the communication between the Optimisation Wrapper and the Optimisation Script is discussed. There are three communication interfaces. The initialisation of the Optimisation Script, the request for a function evaluation and the return of function evaluation results.

It is not considered necessary to explain the Request Function Evaluation and Return Function Evaluation communication processes in depth. The Request Function Evaluation simply passes an array of optimisation parameters, \vec{P} from the Optimisation Script to the

Optimisation Wrapper. The Return Function Evaluation simply passes an array containing the normalised goal function value, $F(\vec{P})$ and constraint function values, $g_j(\vec{P})$ from the Optimisation Wrapper to the Optimisation Script.

Define Optimisation Parameters

The Define Optimisation Parameters process block shown in the top of Figure 4.5 illustrates this communication process. This communication establishes a number of optimisation parameters. These optimisation parameters are listed in Table 4.3. Four of the variables in this initialisation process can be used to tune the optimisation algorithm for specific problems. These four variables are *fdRelStep*, *fdAbsStep*, *maxRelFirstStep* and *conTolMin*.

Table 4.3: Initialisation information for the Optimisation Script.

Variable	Description
x0	Initial optimisation parameter array.
xl	Lower boundary of optimisation parameter array.
xu	Upper boundary of optimisation parameter array.
evaluate	Specifies if the objective function is to be minimised or maximised.
method	Optimisation algorithm type i.e. sequential quadratic programming.
scale	Determines if the parameters are normalised.
iterLim	Limit on maximum number of iterations.
fdRelStep	The maximum relative step size for the gradient analysis.
fdAbsStep	The maximum step size for the gradient analysis.
maxRelFirstStep	The maximum step size for the first iteration.
ncon	The number of constraints.
conTolMin	The allowable tolerance on constraint violation for convergence.
memoryUse	A limit on the use of RAM.
storeHistory	Determines if the optimisation history needs to be stored.

In Section 3.3, when the mesh settings were discussed, it is mentioned that the mesh settings and the optimisation gradient step size are two interdependent aspects of optimisation.

The smaller the step size, the better the performance of the sequential quadratic programming algorithm becomes. However, the smaller the step size, the smaller the mesh elements need to be to accurately simulate the machine. With diminishing mesh element sizes, the time required to perform a function evaluation increases.

In order to obtain convergence within a reasonable amount of computational time, these two aspects are played off against each other to obtain a good balance. This balance can only be obtained through experimentation.

The two variables that describe the gradient step size are *fdRelStep* and *fdAbsStep*. The variable *fdRelStep* describes the step size change as a percentage value of the parameter to be evaluated. The variable *fdAbsStep* describes the step size change as a magnitude value.

The step size in a gradient analysis needs to be described by two parameters because the value of the parameter changes. If the parameter has a large value, the percentage change will be a large step. A large step does not present any problems regarding the mesh settings. If the parameter value approaches zero, the percentage change will become a very small step that in turn presents a problem with regards to the mesh settings.

For every gradient analysis, both step sizes are calculated and the larger of the two step sizes is selected as the gradient analysis step size. This allows mesh settings to be chosen with the knowledge that a step size will not be smaller than a specifically selected value.

The *maxRelFirstStep* variable relates to the allowable change in parameters between the initial and first iteration. If it is known that the initial conditions presented to the optimisation algorithm is close to an optimum, a convergence can be obtained within a faster time if the first step is restricted. This is a useful tool when a number of debugging runs have been performed.

In debugging runs, the first step is left unrestricted. This is so that the diversity of geometric configurations can be well explored. On rare occasions, a debugging run might even converge on an optimum. If it does not converge, however, the data created in the debugging run can be put to good use by selecting initial conditions that are considered to be closer to the optimum. Depending on the confidence of the initial conditions, the first iteration step can be restricted to decrease the optimisation computational time.

The *conTolMin* parameter determines a percentage value of tolerance regarding the constraints. It stipulates that an optimum can be defined, even though a constraint is violated but only if the constraint violation falls within the tolerance zone. This is useful if the output power, for example is calculated to be 2995 W instead of the constraint value of 3000 W. If such a design is found that adheres to the definitions of convergence, except for this constraint, the optimisation can terminate without performing unnecessary evaluations that will ultimately only waste time.

4.5.4 Simulation Wrapper

The Simulation Wrapper is outlined in red in Figure 4.6. It is written and compiled in a 64 bit version of *Python*. The purpose of the Simulation Wrapper is to communicate information from the Optimisation Wrapper to the Simulation Script.

Upon initialisation, the Simulation Wrapper does nothing except watch the Model File location. The Simulation Wrapper will only perform an action when the pickle file in the Model File location is changed.

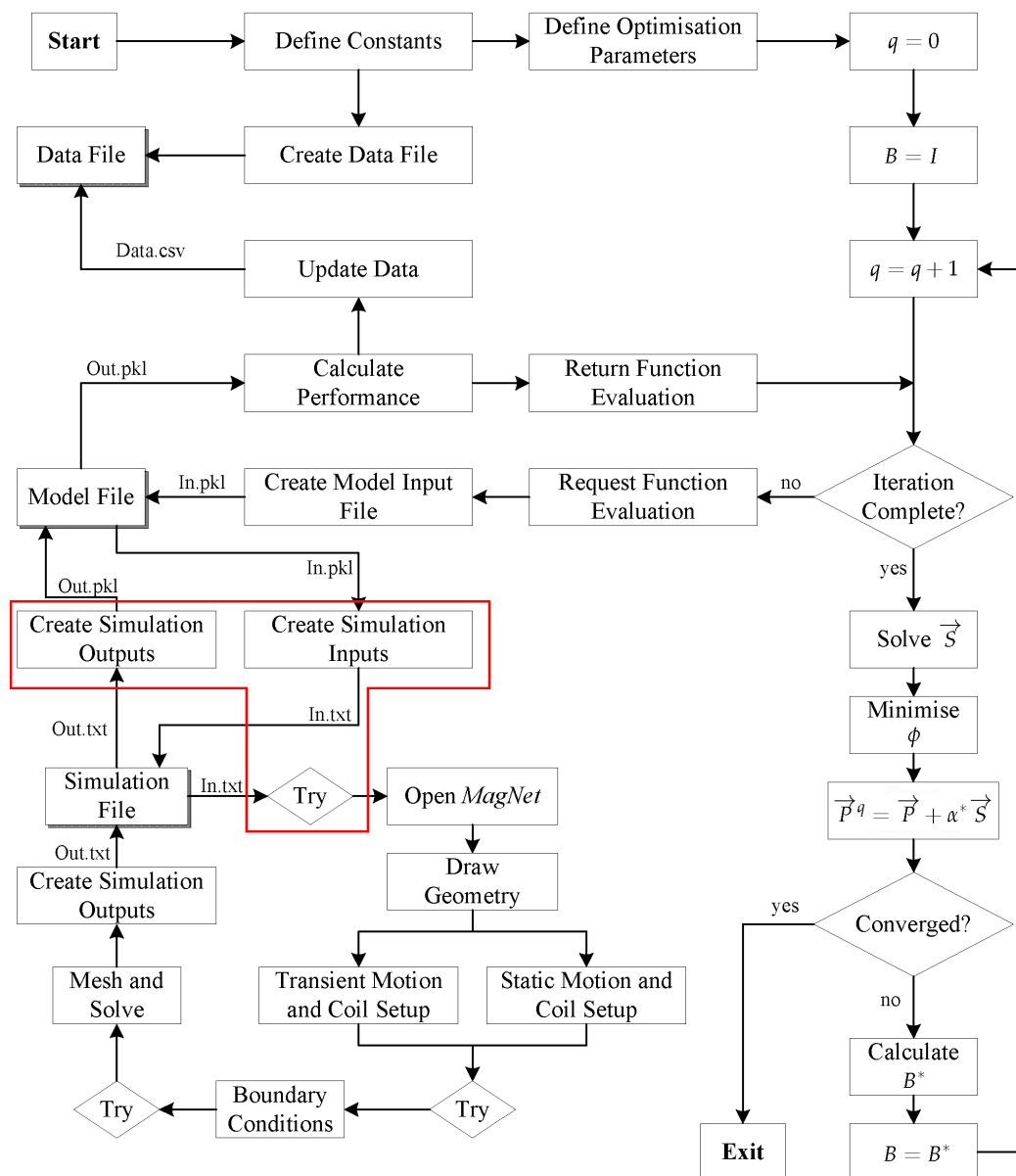


Figure 4.6: Simulation Wrapper within the optimisation structure.

The Simulation Wrapper contains three processes as shown in Figure 4.6. These three processes are the Create Simulation Inputs process, the Create Simulation Outputs process and a Try routine. The Try routine will be described when discussing the Create Simulation Inputs process.

Create Simulation Inputs

As soon as the pickle file in the Model File location is changed to a file named "In.pkl", the Create Simulation Inputs process retrieves the information contained within this file. The information is related to a form that can be understood by the Simulation Script and is then written to a text file named "In.txt".

The In.txt text file is saved in the Simulation File location. This information is now safe. Any process down the line can crash or can be terminated without effecting the information in this file. Consequently a break point is established.

In a separate routine, illustrated by the Try diamond within the red outlined area of Figure 4.6, the Create Simulation Inputs process reads the information that has just been written to the Simulation File location and tries to use this information in the initialisation of an executable file. If unsuccessful, it tries again. This executable file is the Simulation Script.

Create Simulation Outputs

Upon the successful completion of the executable file (the Simulation Script), a text file, Out.txt is written to the Simulation File location. When this happens, the Create Simulation Outputs opens the Out.txt file and reads the information contained within it. If the information contains any errors, the Try process reinitialises the executable file with the information contained within the In.txt file, only using slightly different mesh parameters.

If the text file Out.txt does not contain any recognizable errors, the information is processed and written to an Out.pkl file in the Model file location. Recall that when the pickle file in the Model File location is changed, the Optimisation Wrapper's Calculate Performance process is initialised.

After writing the Out.pkl file, the Simulation Wrapper once again enters a waiting loop. The waiting loop is terminated when the In.pkl file appears once more in the Model File location and the Create Simulation Inputs process begins.

4.5.5 Simulation Script

The Simulation Script is written and compiled in a 64 bit version of *Microsoft® Visual Basic®* as mentioned earlier. The Simulation Script facilitates direct communication to the 64 bit simulation software *MagNet®*.

The structure of the Simulation Script has already been discussed in Section 3.3. In pursuit of clarity, Figure 4.7 illustrates precisely where the Simulation Script fits into the holistic optimisation algorithm, by outlining it in red.

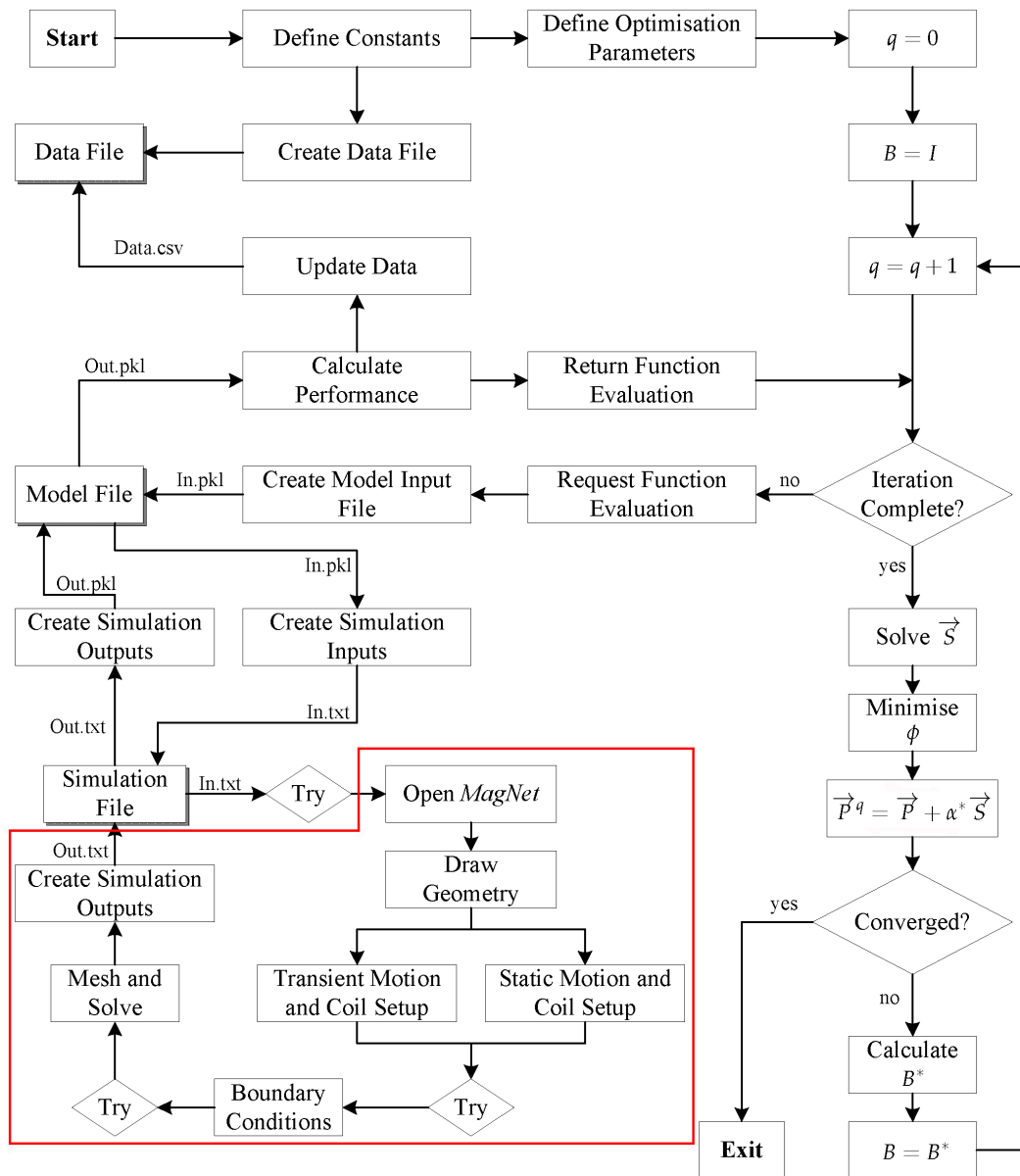


Figure 4.7: Simulation Script within the optimisation structure.

4.6 Conclusive Remarks

In this chapter, the optimisation of the electrical machine is described. The goal of the optimisation and the different types of algorithms that can accomplish this goal have been discussed. A detailed evaluation of the sequential quadratic programming algorithm has also been presented.

The final part of the chapter described the practical implementation of the optimisation algorithm. This implementation describes how the optimisation algorithm communicates with the simulation software that performs the function evaluations.

Chapter 5

Design Evolution

5.1 Overview

The modelling and optimisation described in the previous chapters were used to evaluate and compare different machine topologies. With a quantification of mass, power and losses, different designs can be directly compared to each other. Based on optimisation results and observations, design decisions were made to improve on prior designs. This process of design evaluation and improvement is reported in this chapter.

Over the course of this project, more than sixty optimisations were performed. This computes to roughly estimated 600 days of actively running simulations (excluding the time required to write and debug the algorithms). The resulting data from forty of these optimisations were kept, the rest were discarded as being less important. The structure of this chapter was therefore compiled to give the majority of these forty optimisations, while explaining the evolutionary improvement of the linear generator topologies.

Five stages are selected as important steps in the design evolution. These five stages are evaluated in the following sections, starting with the Initial Design in Section 5.2. The Initial Design is the design of Schutte *et al.* [25] that has already been described in Section 2.4. A more detailed evaluation of this machine is presented here.

The First Design is then described in Section 5.3. In this design, the translator structure is changed and the optimisation is performed with more geometric freedom than was allowed in the Initial Design.

In Section 5.4, an optimisation is performed on a design with geometric freedom along the axis of translator motion. Variations on this design are optimised with an increased number of coils. An investigation on the effect of the design efficiency is then performed and a transient simulation of the optimised design is performed to better understand the different loss mechanisms.

In Section 5.5, the translator structure is changed once again. The translator structure of

the design described on this section uses magnets in a quasi-Halbach array mounted on a laminate steel structure. Six- and eight coil variants of this design are also optimised and a transient simulation is performed.

The optimisation of the Fourth Design is described in Section 5.6. This design incorporates a translator that is only comprised of magnets. Six- and eight coil variants are optimised and the results are shown.

In Section 5.7, the design described in Section 5.6 is optimised using a transient finite element method to perform function evaluations. This is the final design in the evolutionary process.

5.2 Initial Design

The design by Schutte *et al.* [25] is depicted in Figure 5.1 with specifications tabulated in Table 5.1. This topology was chosen as the starting point.

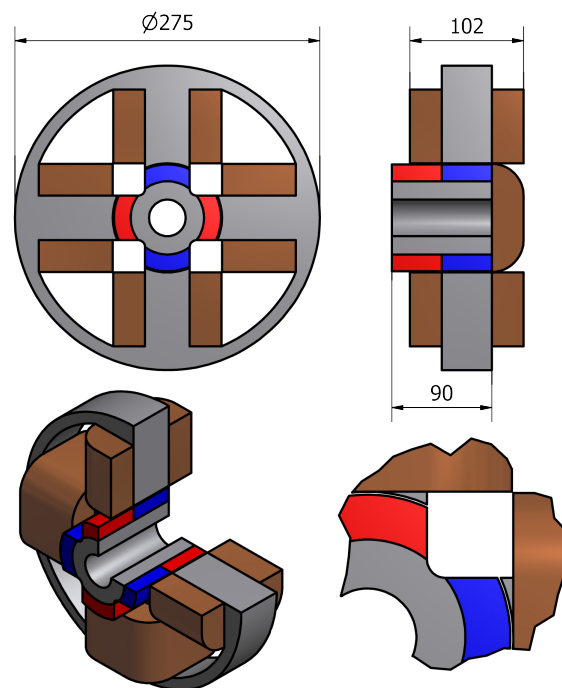


Figure 5.1: Configuration of the Initial Design.

Figure 5.1 shows the transverse flux topology with a moving magnet translator. The translator has the permanent magnets affixed to a laminate silicon steel structure. The performance measures shown in Table 5.1 are identical for subsequent designs (with the exception of the current density) in order to be able to properly compare different topologies.

Table 5.1: Initial Design properties.

Mass Component	Value
Steel	12,4 kg
Copper	10,0 kg
Magnets	1,8 kg
Total	24,2 kg
Performance Measure	Value
Input power	3125 W
Copper loss	125 W
Output power	3000 W
Efficiency	96,0 %
Current density	2,4 A/mm ²

The most significant distinction where the Initial Design by Schutte differs from that of the machines described later in this chapter, is the stroke-length. The stroke-length of the Initial Design is set at 45 mm. The stroke-length of subsequent designs was chosen as 30 mm. The decision to shorten the stroke-length by a third has two motivations.

Firstly, difficulties in testing this machine at high frequencies demanded that a change be made. A large mass oscillating at 50 Hz over a distance of 45 mm, has inertial forces that become difficult and dangerous to test.

Secondly, it is found from reviewing literature that 45 mm is an unusually long stroke length for Stirling engines of this size. To better conform to standard free-piston Stirling engine designs, a stroke-length of 30 mm was selected.

The only other distinction that sets the Initial Design apart from those evaluated later, is the grade of the permanent magnets. Permanent, rare earth magnets (*NdFeB*) with a rating of *N42* were used the Initial Design, while magnets of a weaker rating, *N35*, were subsequently employed.

The reason for choosing a weaker magnetic material relates to concerns regarding the robustness of the design. *N35* magnets, while less capable than *N42* in terms of magnetic field strength, are less susceptible to demagnetisation due to high temperatures (typically in excess of 80 °C at the cold side of free-piston Stirling engines)

Even under proper operating conditions, the temperature that the magnets are subjected to, can become dangerously high for these types of rare-earth magnets. Under faulty conditions the temperature can become much higher. As such, a more robust magnet is deemed necessary.

5.3 First Design

5.3.1 Overview

The first design to be investigated in this project is shown in Figure 5.2. This design is subject to specifications and conditions identical as for the Design with two exceptions, namely the stroke-length and the magnetic material changes mentioned earlier.

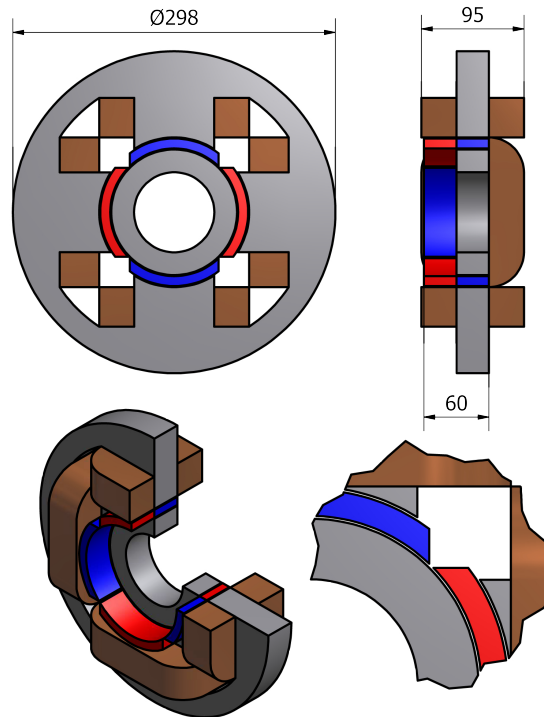


Figure 5.2: Configuration of the First Design.

Two design changes were also implemented in this First Design. Geometric restrictions on the coil were removed as discussed in Section 5.3.2 and the structure of the translator was changed as discussed in Section 5.3.3. The results of optimisation are discussed in Section 5.3.4

5.3.2 Geometric Restrictions

A geometric restriction was initially imposed on the optimisation because of the specific shape of the stator laminations. The coils had to be wound separately of the stator, to be mounted at a later stage.

This was done because the circular stator laminations have "teeth" or "spokes" protruding towards the centre of the machine. The optimisation was restricted to remain within

dimensional parameter sets where it was possible to insert the coils into the central gap and slide them over the stator teeth.

In the First Design it was proposed to divide the stator into segments, thereby making any set of dimensions regarding the coils and teeth that do not occupy the same volume, to be manufacturable. This is due to the conception of a new manufacturing technique whereby the stator can be segmented.

This manufacturing technique uses four identical laminations where the prototype of the Initial Design uses one lamination. These laminations are asymmetrical segments that are placed in an overlapping pattern. The laminations are located by dowel pins. Figure 5.3 shows this manufacturing technique. In this figure, it can be seen that the stator segments are inserted into the coils. Here the coils are wound onto bobbins to secure them in place.

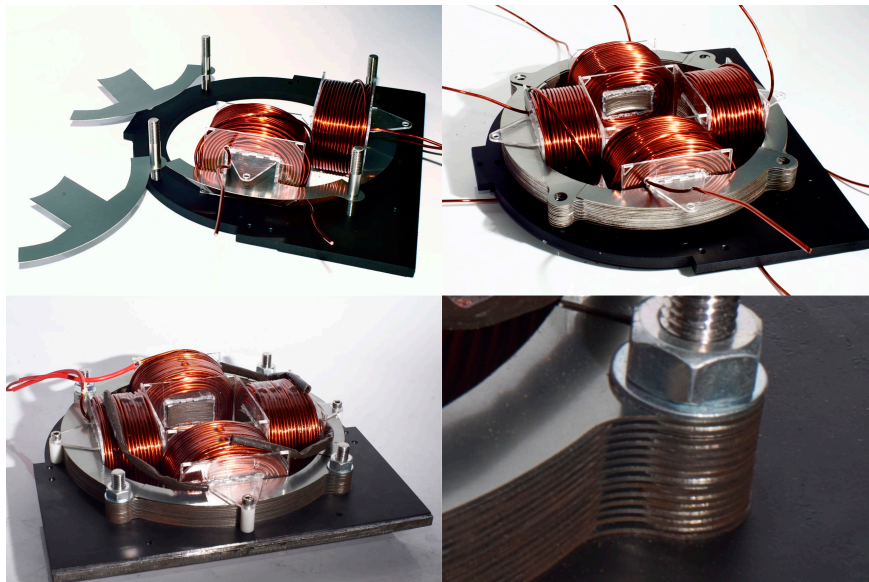


Figure 5.3: Manufacturing technique that allows for a segmented stator.

In Figure 5.2, the top left image shows a sectioned front view of the First Design. It can be observed that the coils (shown in brown) cannot be wound off of the stator, inserted and fitted over the stator teeth. The geometry of the stator teeth would interfere if this was attempted. In the top left image of Figure 5.1, it can be observed that the coils can barely be fitted using conventional stator laminations. The geometric restriction that allows the machine to be manufactured restricted both the height and the width of the coils for the Initial design. Logically then, the First Design would have a coil geometry that is better suited because it is only restricted by the performance measures of the optimisation.

5.3.3 Translator Structure

The laminate structure on the translator was removed and shortened to form an inner stator. The magnets then form the only electromagnetically active component on the translator with dual air-gaps. One air-gap is located between the inner stator and the magnets, the other air-gap is located between the outer stator and the magnets. This design change is illustrated in Figure 5.4.

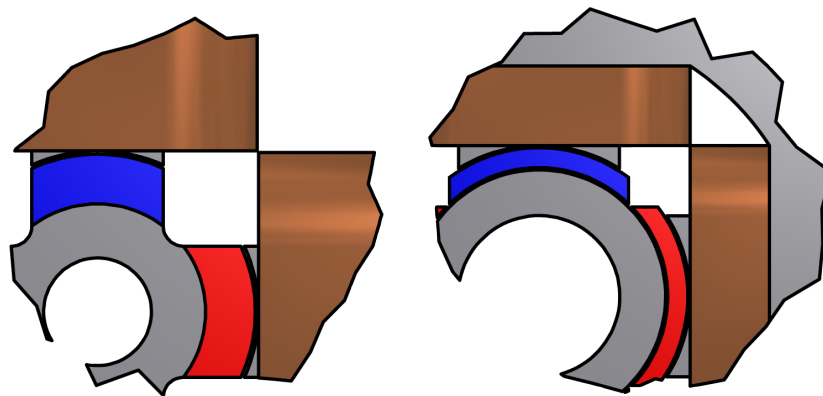


Figure 5.4: Translator comparison from that of Schutte and the First Design.

This change was implemented to eradicate a parasitic permeance path shown in Figure 5.5. This figure shows a sectioned isometric view of the translator from the Initial Design. The translator has been sectioned to best illustrate the parasitic permeance path. The parasitic permeance path is eradicated in the First Design, because the inner laminate structure (shown in grey) no longer spans the length of the translator but rather remains static and is located directly across from the outer stator. This can be seen in the top right and bottom left of Figure 5.2.

From Figure 5.4 it can further be observed that for the First Design, the width of the magnets are not the same as the width of the stator teeth. In the Initial Design, the width of the stator teeth and the width of the magnets are identical. This is because Schutte defined the geometry of the machine in this manner. By assigning an independent optimisation variable to the magnet width, more magnetic material can be used without having an adverse effect on the diameter of the generator.

Because of these design changes, the difference in permeance between the two extreme positions of the translator is increased. Consequently the change in magnetic flux-linkage across the coils increases, thereby inducing a voltage with a greater amplitude.

From Figure 5.4, it can further be observed that the inner laminate structure from the Initial Design is not entirely circular. The shape of Schutte's laminate structure was chosen

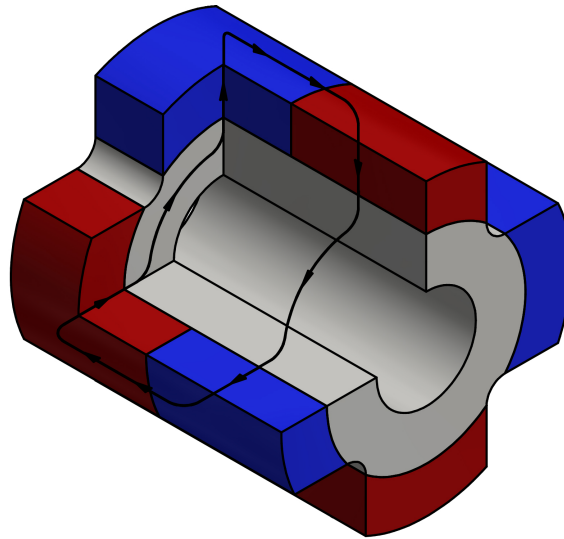


Figure 5.5: Parasitic permeance path of the translator from the Initial Design.

in an attempt to better direct the magnetic flux within that region.

The shape is changed to that of a circular structure for the First Design because Schutte's initial premise proved unnecessary. In fact, it only created a region of increased magnetic flux density. A circular structure better utilises the laminate steel volume.

5.3.4 Optimisation Results

The geometric model, along with the optimisation variables used in the First Design is illustrated in Figure 5.6. This optimisation converged after 67 iterations, performing 681 function evaluations. The results are tabulated in Table 5.2.

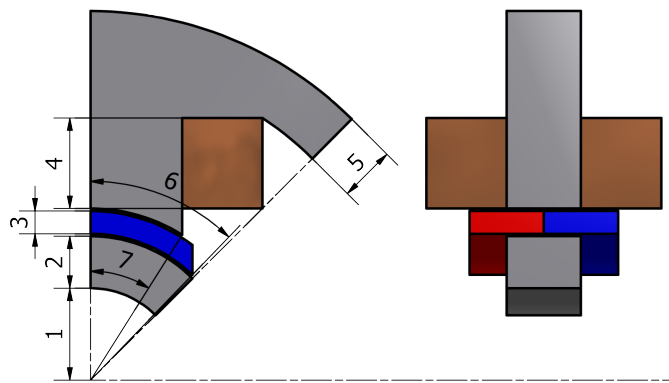


Figure 5.6: Optimisation parameters of the First Design.

The design changes implemented in this First Design, decreases the total electromagnetically active mass from 24,2 kg to 18,4 kg. The electrical output remains practically un-

Table 5.2: First Design optimisation results.

Mass Component	Value
Steel	10,5 kg
Copper	5,4 kg
Magnets	1,5 kg
Total	18,4 kg
Optimisation Parameter	Value
1) Inner stator radius	37,1 mm
2) Inner stator height	21,0 mm
3) Magnet height	9,2 mm
4) Coil height	36,5 mm
5) Outer stator height	36,5 mm
6) Magnet arc	43,9 deg
7) Pole arc	32,2 deg
Performance Measure	Value
Input power	3131 W
Copper loss	125 W
Output power	3006 W
Efficiency	96,0%
Current amplitude	2940 A
Current density	2,57 A/mm ²

changed. Table 5.3 directly compares the mass components of the Initial Design to that of the First Design. It is clearly illustrated in this table, that the mass components decreased in all aspects for the First Design.

Table 5.3: Initial Design vs. First Design mass components.

	Initial Design	First Design
Steel	12,4 kg	10,5 kg
Copper	10,0 kg	5,4 kg
Magnets	1,8 kg	1,5 kg
Total	24,2 kg	18,4 kg

These are considered to be promising results in view of the fact that this design uses weaker magnets that oscillate over a significantly shortened stroke-length. An in-depth analysis of these results was cut short because an in-depth evaluation of the next design discussed in Section 5.4 is equally applicable to this First Design as it is to the next.

5.4 Second Design

5.4.1 Overview

With this step of the design evolution, only one change is made to the design. This change relates to geometric freedom along the axis of motion and is discussed in Section 5.4.2.

With the design change in place, an optimisation is performed and the results thereof are discussed in Section 5.4.3. This design is evaluated further by optimising it in configurations with increased coil-pairs in Section 5.4.4.

The effect of optimising this Second Design to operate at different efficiency levels, is evaluated in Section 5.4.5. This analysis is performed on the four coil configuration.

The analysis of varying efficiency levels led to concerns regarding the losses in this Second Design. Consequently the different loss mechanisms within the linear alternator are evaluated in Section 5.4.6.

5.4.2 Geometric Freedom Along the Axis of Motion

As previously described, the linear alternator is a single phase design with the current sinusoidally driven in phase with the electromotive force. It is therefore logical that the optimisation variables strive to create the best possible voltage waveform using the least amount of electromagnetically active mass, i.e. the voltage waveform that will in combination with the current waveform yield the highest average power.

The profile and amplitude of the voltage waveform is entirely dependent on the magnetic flux-linkage, as it is derived from the flux-linkage waveform. The magnetic flux-linkage waveform is again directly dependent on the geometry, as it is created by the components that the geometry describes. Logically then, the profile and amplitude of the voltage waveform is dependent on the geometry that defines the components of the electrical machine.

It is found in every publication of research on transverse-flux linear machines, that the author is aware of, that there is a fixed relationship between the stroke length, the length of the stator (along the axis of motion) and the length of the translator, i.e. the stroke-length is equal to the stator length and the magnet lengths. Certainly this is because it is common practice in rotating electrical machines to have the rotor and stator lengths equal. It would seem that it has never been considered to deviate from this norm for a linear transverse flux machine design.

It stands to reason that having independent optimisation parameters assigned to the stator and translator lengths, regardless of the stroke length, would have a profound effect on the profile of the flux-linkage and consequently the profile of the induced voltage waveform. Naturally these lengths would influence the electromagnetically active mass as well.

The Second Design investigates this line of thought by incorporating the length of the stator and the length of the translator as independent variables in the optimisation algorithm. Figure 5.7 shows the configuration of the Second Design. Figure 5.7 shows this design change in the top right. The stator, in grey, is shown to have a length different to that of the magnets. This can clearly be seen when compared to the top right of Figure 5.2. This is the only distinction between the First Design and the Second Design.

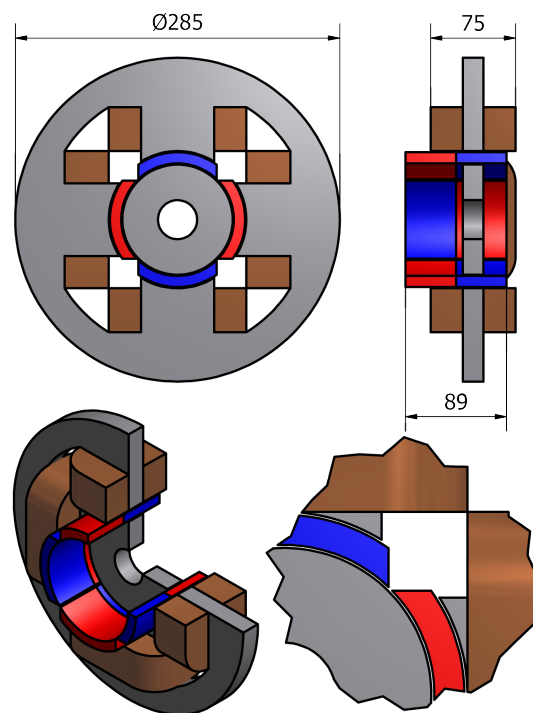


Figure 5.7: Configuration of the Second Design.

5.4.3 Optimisation Results

Figure 5.8 shows the geometric model and optimisation parameters used in this design. Apart from the geometric freedom along the axis of motion, the design and operating conditions are identical to that of the First Design. The optimisation converged after 45 iterations, performing 551 function evaluations. The results are tabulated in Table 5.4.

Figure 5.9 compares the magnetic flux linkage of the First and Second Design on the left and the voltages derived from these flux linkages on the right.

The resulting flux-linkages and voltages shown in Figure 5.9 support two contributing aspects of the design method. Firstly, the First- and Second Designs have strong similarities in terms of their respective outputs. The Second Design achieves this however with 28,8%

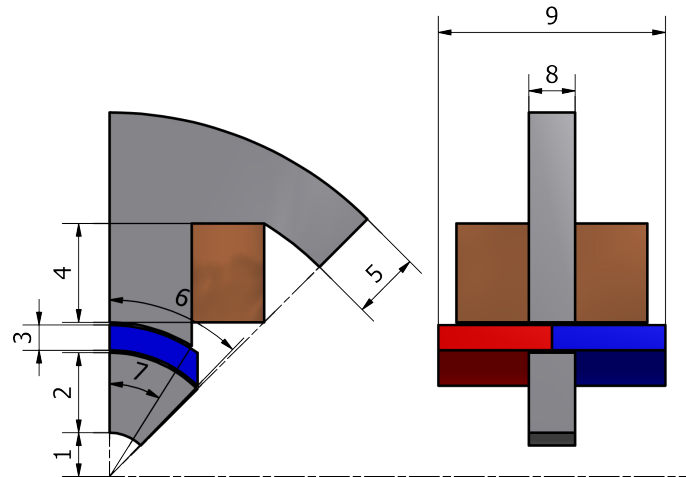


Figure 5.8: Optimisation parameters of the Second Design.

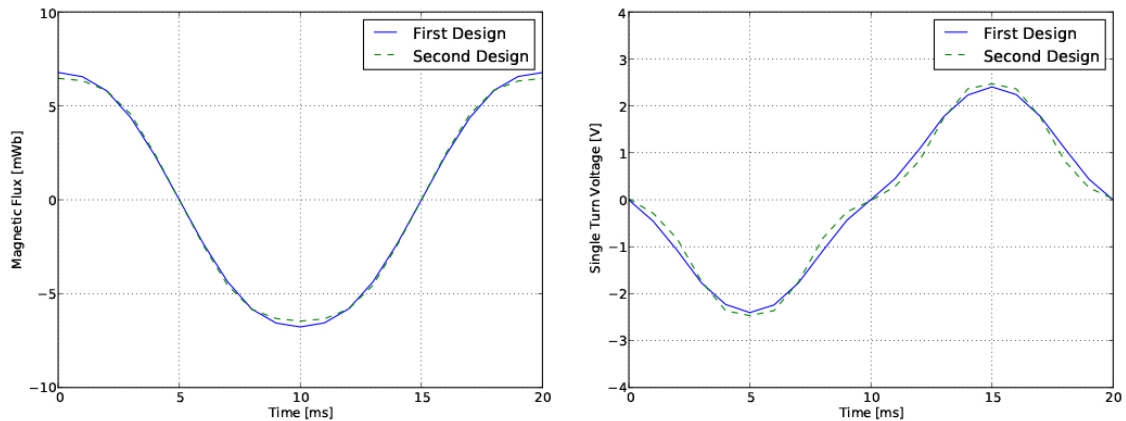


Figure 5.9: No-load magnetic flux-linkage and voltage waveform comparison of the First- and Second Design.

less electromagnetically active mass than the First Design, as can be seen in the results from Table 5.4. This supports the decision to incorporate the optimisation parameter freedoms. A substantial amount of electromagnetically active mass from the First Design is thus not required.

Secondly, it supports the likelihood that both designs are at a near optimal design point within their restrictions. With a smaller laminate stack length in the stators of the Second Design, it stands to reason that the conductor length required to enclose the flux-linkage is shorter. This implies that the coil resistance is lower. For the same efficiency as the first design, the driven current amplitude of the Second Design can therefore be larger (3140 A as opposed to 2940 A), thereby requiring a smaller induced voltage amplitude. This appears to be the only difference between the two designs' electrical output characteristics. As such, it is unlikely that both optimisations would strive towards such a similar no-load flux-linkage profile (entirely dependent on the geometry), if such a profile did not represent

Table 5.4: Second Design optimisation results.

Mass Component	Value
Steel	6,2 kg
Copper	4,9 kg
Magnets	2,0 kg
Total	13,1 kg
Optimisation Parameter	Value
1) Inner stator radius	17,2 mm
2) Inner stator height	31,3 mm
3) Magnet height	10,0 mm
4) Coil height	38,7 mm
5) Outer stator height	26,5 mm
6) Magnet arc	44,0 deg
7) Pole arc	32,1 deg
9) Magnet length	58,8 mm
10) Pole length	18,1 mm
Performance Measure	Value
Input power	3134 W
Copper loss	125 W
Output power	2999 W
Efficiency	96,0%
Current amplitude	3140 A
Current density	2,97 A/mm ²

a near-optimum state. The optimisation process therefore gains credence from these results.

5.4.4 Evaluation of Increased Coil Pairs

In an effort to thoroughly investigate the design environment, a six- and eight coil design was also optimised in the hope that the results lead to a better understanding of the machine topology. This was not only done to investigate the design space, but also to increase confidence in the optimisation process.

A truly optimum design logically requires a specific amount of electromagnetically active mass for these performance measures. The amount of required mass should not vary dramatically between identical designs in slightly different configurations. This hypothesis is tested with the optimisation of six- and eight coil configurations.

The geometry of these optimisations are illustrated in Figure 5.10 and the optimisation results are tabulated in Table 5.5 in direct comparison to the four coil configuration. These

results increase the confidence of the optimisation process because the output performance measures are all of a similar magnitude.

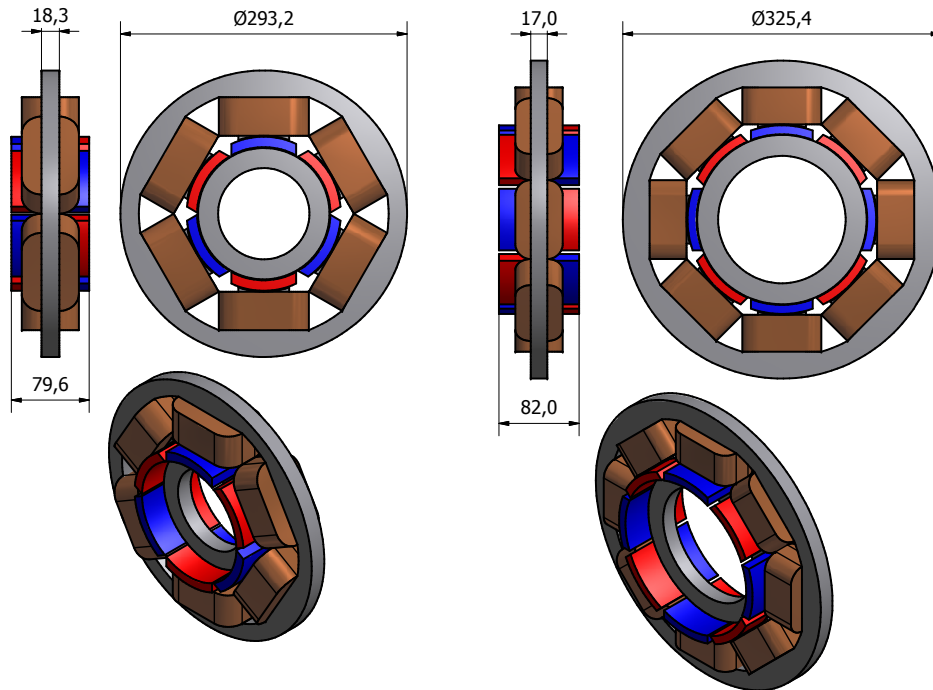


Figure 5.10: Optimised geometry of the Second Design in a six- and an eight coil configuration.

Table 5.5: Design comparison of multiple coil optimisation results.

	Four Coil	Six Coil	Eight Coil
Steel Mass [kg]	6,2	5,7	6,4
Copper Mass [kg]	4,9	4,1	3,6
Magnet Mass [kg]	2,0	2,6	2,9
Total Mass [kg]	13,1	12,3	12,9
Input Power [W]	3124	3129	3124
Copper Loss [W]	125	125	125
Output Power [W]	2999	3004	2999
Efficiency [%]	96	96	96
Current Density [A/mm^2]	2,97	3,26	3,51

Even though it was found that the six- and eight coil designs perform marginally better than the four coil counterpart as can be seen in Table 5.5, this investigation remains focused

on the four coil configuration. This is done to ensure an accurate comparison between preceding and subsequent designs.

It is further observed, that the six- and eight coil designs have an increased magnet mass. This means that the translator mass will be higher than that of the four coil design. Within the Stirling engine application this a negative aspect of these configurations. The increased translator mass increases the total mass of the Stirling engine's moving member. Magnetic material is also currently the most expensive material within the electrical machine's components. These two aspects lead to the conclusion that the four coil configuration is the superior design.

5.4.5 Investigation on the Effect of Machine Efficiency

The efficiency of the machine, set at 96%, is chosen as the design point because that is the efficiency at which Schutte set the efficiency for the previous project. The effect of the efficiency on the machine's mass remains unexplored.

The primary reason for investigating the linear alternator efficiency is related to the application. As one of the possible applications for this machine is in the astronautical industry where the mass is critically important, the machine is optimised at different efficiencies to gauge the effect thereof on the mass.

A secondary reason for this study is to further develop the design environment. This could possibly lead to different insights as well as increasing the confidence of the optimisation process. This investigation is confined to the four coil design. The results are tabulated in Table 5.6.

Table 5.6: Study of optimisations at different efficiencies.

Efficiency	90%	91%	92%	93%	94%	95%	96%
Steel Mass [kg]	2,9	4,6	4,4	4,9	5,0	4,5	6,2
Copper Mass [kg]	2,0	2,0	1,9	2,2	2,4	3,1	4,9
Magnet Mass [kg]	2,8	2,5	2,9	3,0	3,7	3,8	2,0
Total Mass [kg]	7,7	9,1	9,2	10,1	11,1	11,4	13,1
Input Power [W]	3339	3310	3259	3225	3200	3159	3124
Copper Loss [W]	333	297	261	226	191	158	125
Output Power [W]	3006	3013	2989	2999	3009	3001	2999
Current Density [Amm ²]	7,44	7,09	6,80	5,88	5,4	4,17	2,97

The data from this investigation leads to several observations. First of all, it seems that a decrease of 6% efficiency could lead to a machine design with 41% less mass. This result is questionable.

Secondly, the optimisation results show some variance. Generally a trend can be seen in the results, however, the composition of the mass components differ from one efficiency to the next.

The mass component variance could simply be attributed to saturation in the silicon steel laminations but this would certainly reveal a trend in the variance were there is none. This is observed in the 91% efficiency optimisation with a steel mass of 4,6 kg and the 95% efficiency optimisation with a steel mass of 4,5 kg. This is not consistent with the premise of magnetic saturation.

Furthermore, the observation that the 95% optimisation has nearly double the magnet mass of the 96% optimisation is not logical. Results that had first appeared to be logically congruent, now hold less credence.

These results could simply be explained by a relatively flat goal function, i.e. different configurations of the dimensional parameters yield similar or even identical results. This is arguably a very good thing because in that case a restriction can be placed on, for instance, the magnet mass without significantly influencing the overall mass.

It has already been mentioned in Section 4.4.4 that the use sequential quadratic programming has a drawback. Sequential quadratic programming minimised an auxiliary function that expresses the search direction, it does not minimise the goal function itself. This can possibly lead to a convergence on a near-optimum point instead of a true optimum point. If the the goal function is relatively flat, this drawback can possibly account for the results shown in Table 5.6.

However, there appears to be an influence on the optimisation that is not taken into account within the design environment. These results demand further investigation.

5.4.6 Investigation of Logically Inconsistent Results

As mentioned earlier, the only loss mechanism that is taken into account within the optimisation, is that of the copper losses incurred within the coil. It is assumed that this is the dominant loss mechanism and that the frequency dependent losses, as a result of magnetic flux variations are negligible. This assumption was originally made on the basis that a 50 Hz operating frequency tends toward the lower end of frequency dependent losses in general.

At this stage a new resource was made available, namely the ability to perform transient analysis on the machine designs. A transient three-dimensional finite element analysis was therefore performed on the 96% optimised design to asses the validity of the assumption that the frequency dependent losses are negligible.

Figure 5.11 shows the copper losses of the coils along with the eddy current losses induced within the magnets for the four coil, 96% efficiency design. A deconstruction of the

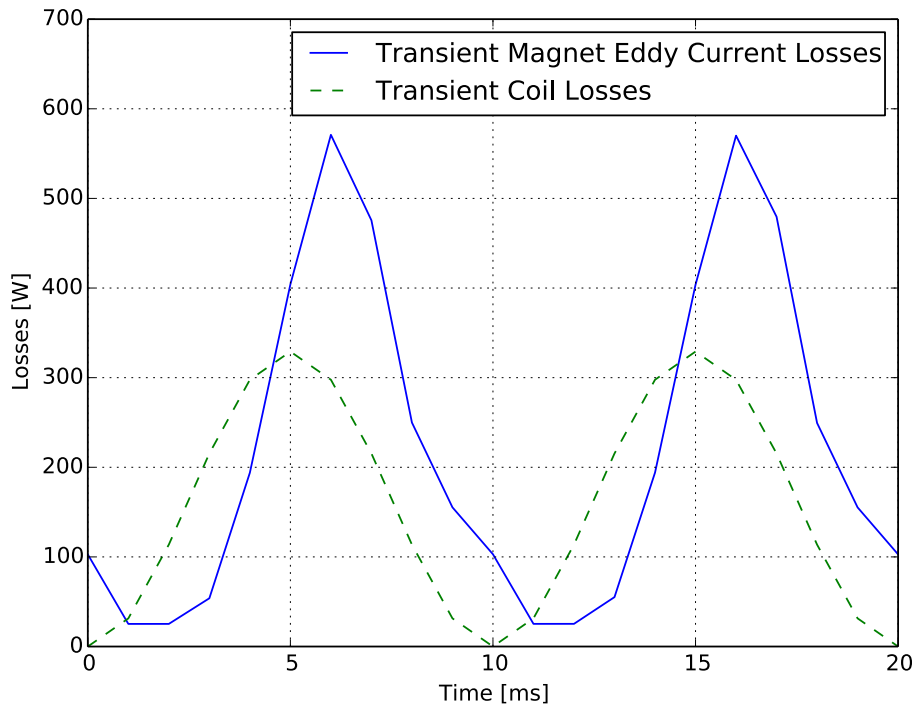


Figure 5.11: Transient losses of the Second Design.

different loss mechanisms is given in Table 5.7.

Table 5.7: Transient analysis to determine loss mechanisms.

Loss Mechanism	Static	Transient
Copper Losses [W]	125	158
Ohmic Losses in Magnets [W]	-	230
Hysteresis Losses in Core [W]	-	15
Eddy Losses in Core [W]	-	6
Total [W]	125	409

It should be noted that the copper losses from the static and transient analysis differ. The copper losses in the static simulation are calculated at 125 W and the transient simulation calculates the losses at 158 W. Initially this caused alarm. Recall that in optimisation, the copper losses are calculated analytically from the geometry. Should these calculations be erroneous, the entire study would be rendered irrelevant.

It was found however, that the analytical copper loss calculations were consistently conservative by exactly the same factor (0,79) when compared to the finite element simulation loss calculations. The reason for this remains unclear but as this is a comparative study, the error was ignored. Subsequent optimisations were performed using the same calculations

as previous optimisations. This is so that the designs can still be directly compared to each other and this can be done because the copper losses in optimisation are always conservative by exactly the same factor when compared to the copper losses simulated in the transient finite element environment. An investigation of the discrepancies between the calculated and simulated losses is presented in Appendix B.

More importantly, the transient simulation shows that the copper losses are not the dominant loss mechanism in this machine design. The eddy currents induced within the magnets are much greater than initially assumed. This can be seen in Figure 5.11. Table 5.7 shows that the eddy losses in the magnets contribute to 56,2% of the total losses. This reveals several problems with the design.

Firstly, the performance measures are degraded. The output power is reduced to 2725 W as opposed to the desired 3000 W and the efficiency is 87% instead of the desired 96%. The losses in the magnets are also of such a magnitude that the risk of demagnetisation becomes a real concern.

There are ways in which this problem can be addressed without significantly changing the design. The magnets could be segmented in a manner similar to that proposed by Wills and Kamper [39]. This would, however, adversely effect the mechanical integrity of the magnets.

The mechanical integrity of the magnets are already a matter of concern in this design. The design is similar to that depicted in illustrations of the design used by Infinia Corporation [9] (shown in Figure 2.9), but it remains unclear as to how this magnet configuration is incorporated into a mechanical design.

To facilitate translator motion between two stators, the magnets would have to be fixed to some sort of magnet carrier. This magnet carrier would have to be constructed out of a material that does not conduct electricity. Failing to do so, could result in a mechanical design that "short-circuits" the magnetic flux-linkage. This could result in a degradation of the voltage induced within the coils.

The use of materials that do not conduct electricity, presents a mechanical problem. The translator is subject to repetitive mechanical loading and consequently subject to mechanical fatigue. Materials that do not conduct electricity are all, to the author's knowledge, susceptible to mechanical fatigue. Polymer compounds are subject to mechanical "creep" under repetitive loading and the brittle nature of ceramics makes them susceptible to the propagation of structural fractures under repetitive loading. These qualities adversely effect the design life of the mechanical sub-structure. A segmented magnet design would compound these mechanical concerns.

Instead of attempting to facilitate this drawback in the magnet design, it was decided to investigate a different translator configuration in the hope of eliminating the problem. This led to the Third Design.

5.5 Third Design

5.5.1 Overview

Some important decisions had to be made at the onset of the Third Design. With the realisation that the frequency dependent losses have a significant effect on the design, the simulation method had to be reconsidered. This is discussed in Section 5.5.2.

The design itself also required some much needed changes. The mechanical integrity of the design is questionable. It is not considered practical to attempt a mechanical design on the previous configuration. Even if it were practical, serious concerns regarding the composition of losses need to be addressed. Section 5.5.3 describes the changes that are implemented to address the issue of eddy losses in the magnets. Section 5.5.4 discusses the mechanical aspects of the Third Design.

In Section 5.5.5, the results of the optimisations are discussed. Once again, the six- and eight coil configurations are optimised along with the four coil configuration.

The different loss mechanisms are then evaluated as described in Section 5.5.6. In this section, conclusive remarks on the Third Design are also made.

5.5.2 Simulation Method

Simulating a single machine design with a transient three dimensional finite element analysis is a relatively simple task. Incorporating such a technique into the existing optimisation structure is rather complex.

Increasing the number of parameters of an optimisation quadratically increases the magnitude of the problem defined by the sequential quadratic programming algorithm and it would logically then require more iterations to converge. Because there are more parameters, more function evaluations are now required to produce gradient information for each iteration in this problem of increased complexity. Individual function evaluations would now take of the order of three times longer to complete as the simulated cycle is more than doubled and a single time-step requires more time to evaluate in a transient environment. Sequential quadratic programming constants need to be tuned once more, mesh setting need to be revisited and the simulation script and the model outputs need to be rewritten.

A decision is made to proceed with the static structure rather than changing to a transient one. This decision is made considering that the current static optimisation structure is already in place and that this system can produce a result within only around ten days while the transient optimisation would probably require more than a month and also considering that the task of creating a transient optimisation environment would require significant time.

This decision is based on the original goal of the project, i.e. to advance this technology

of linear machines. The finite element environment is merely a design tool used to serve this goal. A better design of the machine with a careful consideration of the pitfalls in the modelling technique would better serve the technology than redesigning the design tool at this stage of the project.

5.5.3 Loss Targeted Design

In order to produce the magnetic flux-linkage that is largely responsible for the specific power improvement of the First- and Second Design, the magnets constantly move between two reluctance networks with significantly different reluctance magnitudes. These two reluctance networks are that of the low reluctance path between the inner and outer stators and that of the high reluctance paths of air on either side of the stators. This results in flux variations within the magnets and consequently the eddy currents responsible for the losses.

In the Initial Design, the magnitude of this problem is lessened by the fact that the magnets are mounted on a laminate silicon steel stack. While this lessens the reluctance difference across the stroke-length, it creates a parasitic flux path that degrades the flux-linkage across the coils as shown in Figure 5.5.

By revisiting the design of Schutte *et al.*, but changing the configuration of the magnets on the translator to that of a quasi-Halbach array, the magnetic flux can be shaped and directed away from the parasitic path and through the coil-enclosed stator core. The configuration of the Third Design is shown in Figure 5.12.

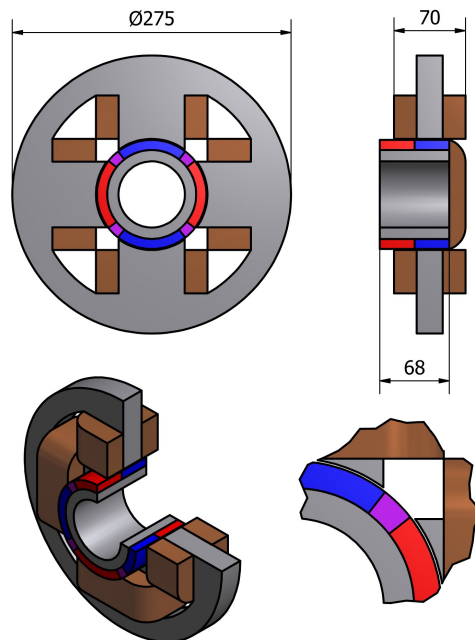


Figure 5.12: Configuration of the Third Design.

In this design configuration, it is expected that the magnetic flux-linkage will be increased compared to the Initial Design and the magnetic flux variance within the magnets will be decreased compared to the First- and Second Design.

The benefits of geometric freedom along the axis of motion within an optimisation environment are established. This is naturally also included in the optimisation of the Third Design.

5.5.4 Mechanically Targeted Design

A mechanical support structure to this design can be fairly simple in comparison to the First- and Second Design. There is no longer an inner stator as can be seen in Figure 5.12.

Apart from the fact that the mechanical structure can now be of a less complicated configuration, an air-gap has also been eradicated. This has implications in the force profile in the radial direction of the translator. Figure 5.13 compares the translators of the Second- and Third Designs. In this figure, one air-gap of the Second Design is seen to be removed for the Third Design.

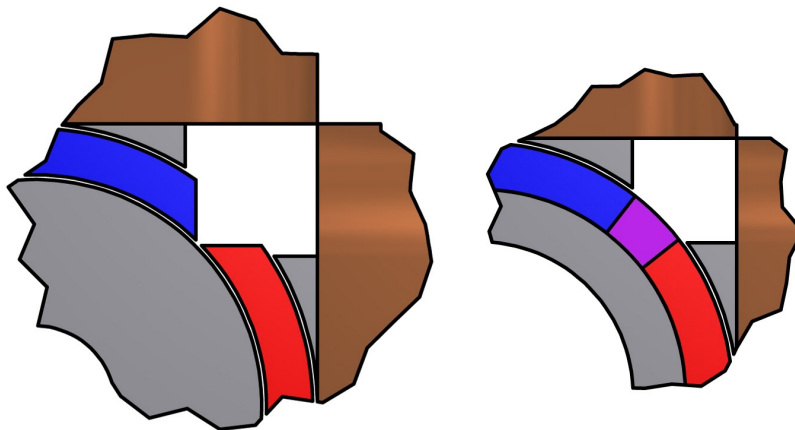


Figure 5.13: Configuration of the Third Design

A dual air-gap machine would require in the range of twice the mechanical stiffness in-order to maintain air-gap tolerances. Within the limited space and with the mechanical limits of various materials, this could have proved impossible in the previous designs. The reason for this is because this linear generator is an inherently unstable mechanical structure.

If the translator structure is assumed to be perfectly stiff and manufactured to the perfect dimensions, no resultant radial forces are present on the translator as all the forces cancel each other out. However, should the translator shift in any radial direction, an imbalance of the forces acting on the translator force the translator further into that specific direction. The more the translator deviates from the radial centre, the greater the imbalance of the forces becomes.

In the first two designs, the forces act on both sides of each magnet. The magnet carrier would likely have to be constructed from an engineering plastic, which is more flexible than steel. An inner stator would have to be located inside the linear oscillating structure. Considering the mechanical instability, it is not clear how this can be accomplished, even though a similar design by Qiu *et al.* [9] does exactly that as illustrated in Figure 2.9.

The Third Design eliminates most of these mechanical problems while hopefully maintaining similar electrical performance measures. This is the primary improvement of the Third Design. The laminate translator stack can simply be fixed to a stainless-steel shaft and only one air-gap per magnet needs to be considered.

5.5.5 Optimisation Results

Figure 5.14 illustrates the optimisation variables employed in this design. The performance measures are tabulated in Table 5.8.

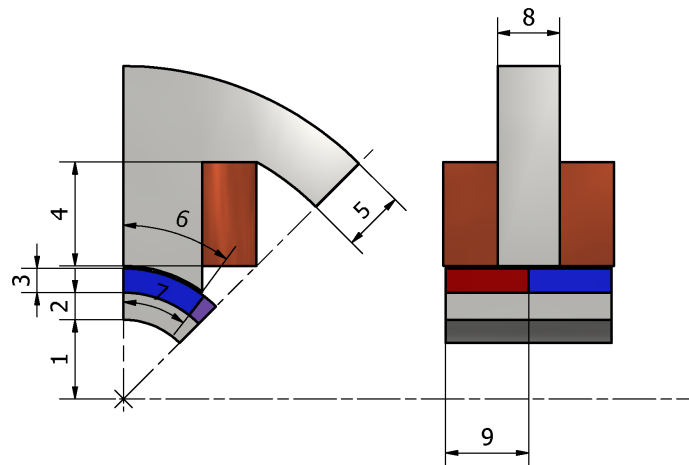


Figure 5.14: Optimisation parameters for the Third Design.

This optimisation converged in 375 iterations, performing 4505 function evaluations. The reason why this optimisation took more than three times longer to converge than the previous optimisations remains unclear. It could be attributed to the change in design and consequently the design environment, which would require some parameter tuning for the sequential quadratic programming algorithm.

The specific reason, however, is not the main focus of this study. Subsequent optimisations for the six and eight coil configurations converged within the expected time frame and the mystery remains unsolved. Perhaps a single function evaluation produced inaccurate results, thereby driving the optimisation temporarily in the wrong direction. This is possible as the geometric freedom in the design environment is purposefully as unrestricted as possible. Finding such a flaw requires a careful analysis of over 4500 simulations and this was

Table 5.8: Third Design optimisation results.

Mass Component	Value
Steel	8,6 kg
Copper	4,2 kg
Magnets	1,6 kg
Total	14,4 kg
Optimisation Parameter	Value
1) Inner stator radius	32,7 mm
2) Inner stator height	11,2 mm
3) Magnet height	10,0 mm
4) Coil height	42,9 mm
5) Outer stator height	25,1 mm
6) Magnet arc	42,9 deg
7) Pole arc	36,3 deg
8) Magnet length	68,4 mm
9) Pole length	25,6 mm
Performance Measure	Value
Input power	3138 W
Copper loss	125 W
Output power	3013 W
Efficiency	96,0%
Current amplitude	3103 A
Current density	3,2 A/mm ²

considered to be an unnecessary allotment of resources. This decision was based on the fact that a better design configuration had already been envisioned and such an investigation would not serve the main goal of the project.

From this optimisation based in a static simulation environment, the design appears to be an improvement on the previous efforts. Similar performance measures are observed, while some design problems are eliminated as discussed in the previous sections.

The six- and eight-coil variants on the design were optimised for similar reasons as that of the previous design. Added to the reasons of exploring the design environment, it was also considered that the quasi-Halbach configuration might perform marginally better in these configurations.

The optimisation results from the six- and eight coil configurations are shown in Figure 5.15. The performance measures of these machines are listed in Table 5.9.

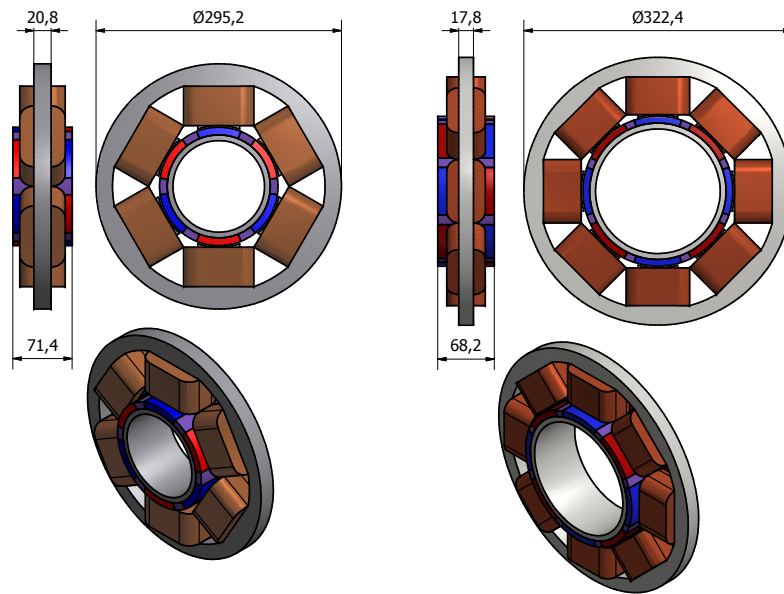


Figure 5.15: Optimised geometry of the Third Design in six- and eight coil configuration.

Table 5.9: Comparison of multiple coil optimisation results.

	Four Coil	Six Coil	Eight Coil
Steel Mass [kg]	8,6	6,9	7,0
Copper Mass [kg]	4,2	3,9	3,7
Magnet Mass [kg]	1,6	2,1	2,2
Total Mass [kg]	14,4	12,9	12,9
Input Power [W]	3138	3146	3138
Copper Loss [W]	125	125	125
Output Power [W]	3013	3021	3013
Efficiency [%]	96	96	96
Current Density [A/mm^2]	3,2	3,4	3,5

By analysing the results from this study, it is realised that the problematic optimisation of the four coil configuration probably did not find the optimum. In Table 5.9, the total mass of the four coil configuration is more than a kilogram greater than the mass of the other two configurations. While it is possible that this is an accurate representation of the machine optimisation goal function for increased coil configurations, it is unlikely. This optimisation could have been repeated with different initial values to possibly find a better design but as an improved design was already envisioned, this would just have wasted time. Instead, a transient analysis is performed on the design.

As the four coil design is still considered to be of a near-optimum configuration, the

machine characteristics should still be applicable. A transient analysis would therefore allow the machine evolution to continue onto the next logical step without hindrance.

5.5.6 Transient Analysis

Figure 5.16 shows the composition of losses in this four coil configuration of the Third Design. Table 5.10 contains the data from these losses.

From the transient analysis, it is observed that the losses in the magnets are diminished compared to previous efforts. However, these losses are still a concern in the design. The risk of demagnetisation is still present and the efficiency of the machine is still degraded beyond the intended scope.

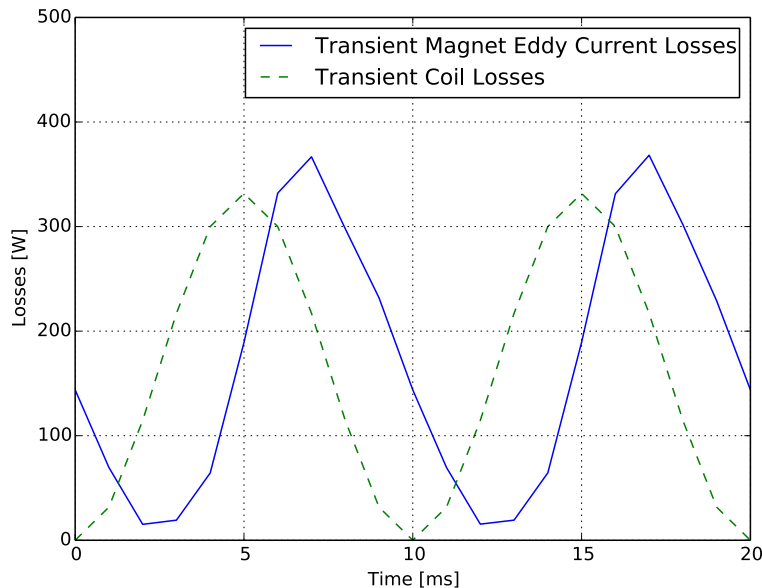


Figure 5.16: Loss components in the Third Design.

Table 5.10: Transient analysis to determine loss mechanisms

Loss Mechanism	Static	Transient
Copper Losses [W]	125	158
Ohmic Losses in Magnets [W]	-	165
Hysteresis Losses in Core [W]	-	16
Eddy Losses in Core [W]	-	6
Total [W]	125	345

The output power is degraded to 2793 W and the efficiency to 89%. Even though this is only a marginal improvement on the Second Design's 87%, most of the issues regarding

the manufacturability of the machine have been resolved. This machine can be built using conventional construction methods. This is the primary improvement that this step in the machine evolution yields.

5.6 Fourth Design

5.6.1 Overview

The fourth design follows the next logical step in translator design. The inner laminate stack of electric steel on the translator, that inherently forms a parasitic flux path, is not a required part of the design and can therefore be discarded. The configuration of the fourth design is shown in Figure 5.17.

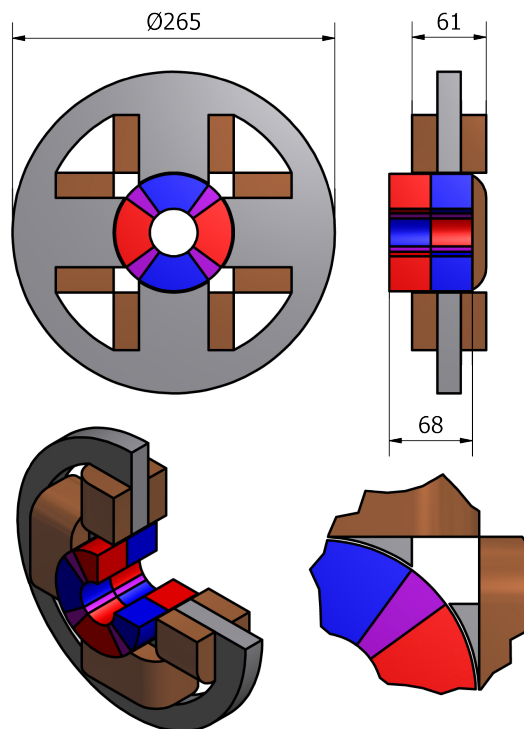


Figure 5.17: Configuration of the Fourth Design.

In Section 5.6.2 results from the Fourth Design optimisation are discussed. In this section the six- and eight coil configurations are optimised as well. This is not only done to increase confidence in the optimisation but additionally because it is considered that the translator structure could yield interesting results for the six- and eight coil configurations.

A transient simulation is performed on the optimised design of the four coil configuration of this Fourth Design. The results of the transient simulation are analysed in Sec-

tion 5.6.3. The machine durability is evaluated in Section 5.6.4 with consideration to the practical implementation of this design.

5.6.2 Optimisation Results

The optimisation converged after 20 iterations performing 231 function evaluations. The optimisation parameters are shown in Figure 5.18. The results are shown in Table 5.11.

In this optimisation, there was one less parameter to be considered as a component was completely removed. Observe that the inner laminate structure, shown in grey for the Third Design in Figure 5.14, is no longer present in Figure 5.18.

Table 5.11: Fourth Design optimisation results.

Mass Component	Value
Steel	4,8 kg
Copper	3,9 kg
Magnets	4,5 kg
Total	13,2 kg
Optimisation Parameter	Value
1) Inner stator radius	20,8 mm
2) Magnet height	27,1 mm
3) Coil height	47,8 mm
4) Outer stator height	22,0 mm
5) Magnet arc	35,2 deg
6) Pole arc	34,1 deg
7) Magnet length	101,6 mm
8) Pole length	20,1 mm
Performance Measure	Value
Input power	3131 W
Copper loss	125 W
Output power	3006 W
Efficiency	96%
Current amplitude	3254 A
Current density	3,3 A/mm ²

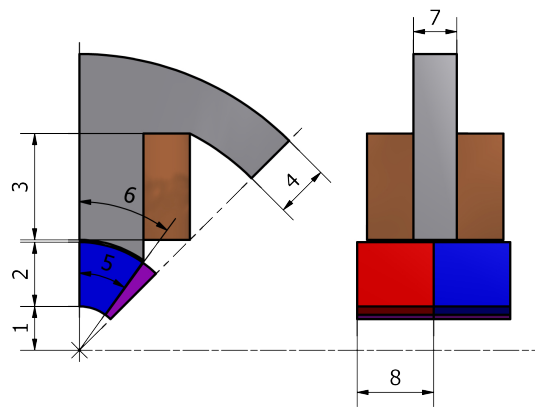


Figure 5.18: Optimisation variables of the Fourth Design.

The fact that this optimisation converged after performing only 231 function evaluations illustrates how removing a single optimisation parameter can decrease the time required to perform an optimisation. Recall that other optimisations performed 681, 551 and 4505 function evaluations for the First-, Second- and Third Designs respectively.

The design changes incorporated into this optimisation reflect the process followed in the previous design. It is from consideration of the problem during the unusually long optimisation of the Third Design that this translator was envisioned.

The translator structure of the Fourth design results in several advantages to the performance and practicality of the machine. The durability, the electrical properties and the mechanical design all profit from this design change as is evaluated in the following sections. This translator structure does however have a large permanent magnet material mass and this is a drawback.

Figure 5.19 and Table 5.12 shows the results of the six- and eight coil variations.

The analysis of increased coil designs was done specifically here, because it was considered that the quasi-Halbach translator of the six- and eight coil variations would perform better. Surprisingly, this was not the case. In this study, for the first time, the four coil configuration out-performs the six- and eight coil configurations. This could be due to the fact that the inner diameter of the translator needs to be larger for additional coil configurations in order for the quasi-Halbach array to be properly utilised.

This study, however, shows a clear trend in performance between the configurations of the Fourth Design. This is perhaps because the optimisations should better represent the machines as a result of the composition of losses or because the optimisation process itself has been refined to the point where it is reliably repeatable.

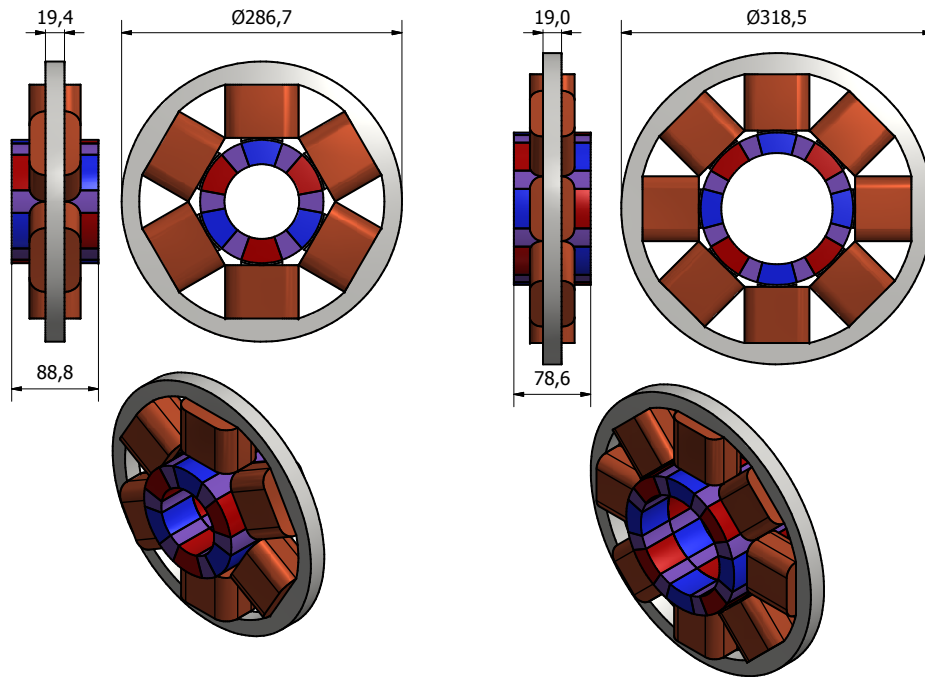


Figure 5.19: Optimised geometry of the Fourth Design in six- and eight coil configuration.

Table 5.12: Comparison of multiple coil optimisation results.

	Four Coil	Six Coil	Eight Coil
Steel Mass [kg]	4,8	4,6	5,4
Copper Mass [kg]	3,9	3,8	3,8
Magnet Mass [kg]	4,6	5,3	5,3
Total Mass [kg]	13,2	13,7	14,5
Input Power [W]	3131	3137	3147
Copper Loss [W]	125	125	125
Output Power [W]	3006	3012	3022
Efficiency [%]	96	96	96
Current Density [A/mm ²]	3,3	3,3	3,3

5.6.3 Transient Analysis

A transient simulation of the optimised configuration of the Fourth Design confirms that the losses within the magnets are lowered even further as illustrated in Figure 5.20 and tabulated in Table 5.13.

In this Fourth Design, the output power is only degraded to 2870 W and the efficiency to

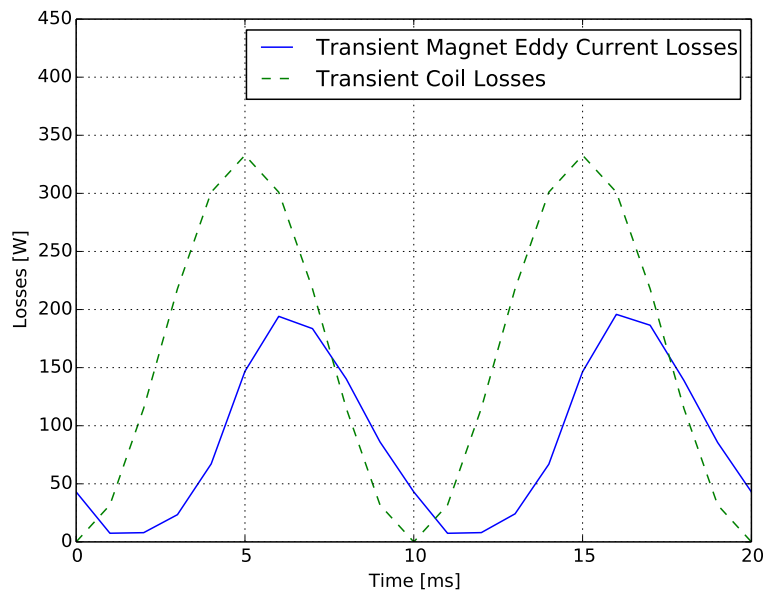


Figure 5.20: Loss components in the Fourth Design.

92%. The design process of maintaining a static simulation in optimisation, but designing specifically to reduce the losses that the simulation cannot account for, has worked to an extent.

Table 5.13: Transient analysis to determine loss mechanisms in the Fourth Design.

Loss Mechanism	Static	Transient
Copper Losses [W]	125	158
Ohmic Losses in Magnets [W]	-	86
Hysteresis Losses in Core [W]	-	12
Eddy Losses in Core [W]	-	5
Total [W]	125	261

In the Fourth Design the copper losses in the coils is the dominant loss mechanism and account for 61,5% of the total losses. While this is an improvement on previous efforts, it is still not ideal.

At this stage in the design process, no further design changes can be envisioned that will force the optimisation away from loss mechanisms that the simulation environment cannot account for.

Figure 5.21 clearly shows that there has been a steady decline in time variant losses from the Second Design to the Fourth Design. The tactic of a loss "targeted design configuration" can however not improve on the composition of losses any more than it already has.

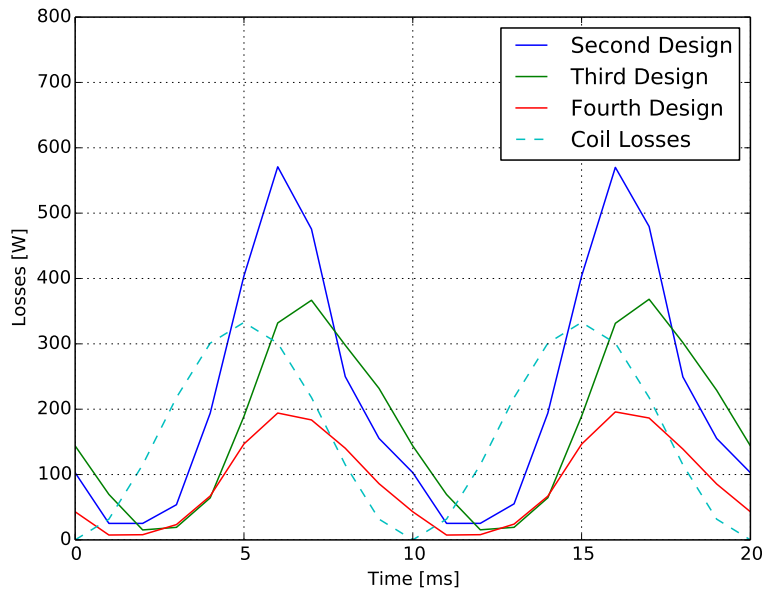


Figure 5.21: Comparison of loss components.

5.6.4 Machine Durability

The permeability of a magnetic material is comparable to that of air (within a 2% error for modern magnets) [40]. As such, the effective air-gap of this design is increased. Magnets located across the stator are therefore not subjected to a significantly different reluctance to magnets located away from the stator. As the translator oscillates, the magnets do not experience a significant change in magnetic flux.

The eddy currents induced within the magnets are therefore of a smaller magnitude and consequently the losses within the magnets decrease. This directly effects the temperature at which the magnets operate, because the eddy losses manifest in the form of heat.

With the increase in effective air-gap between adjacent stator coils, the amplitude of driven current that can demagnetise the translator, increases as well. The risk of translator demagnetisation is therefore decreased for the translator configuration in this Fourth Design. This increases the durability.

In mechanical design, no manufacturing process exists that can produce components with perfect dimensions [41]. Mechanical tolerances are specified in designs to ensure a quality control that restrict these manufacturing errors to magnitudes that do not interfere with the operation of the machine.

The most complicated mechanical aspect of the design, is that of the air-gap. By eliminating a component situated between the shaft and the air-gap, the task of ensuring that mechanical tolerances fall within the operation bounds of the machine becomes easier.

This implies that the machine is less expensive to manufacture due to more relaxed man-

ufacturing tolerances. Or alternatively, it is just as expensive but with better tolerances that strive closer to the exact dimensions. The mechanical design of this fourth machine therefore benefits from the translator configuration.

The increase in the effective air-gap, changes the effective series inductance of the machine. The proposed operation of this family of generators, where the current is driven in phase with the electromotive force, requires power electronics to do so. A smaller series inductance for this design simplifies this task compared to previous designs. The electrical properties of a generator that incorporates this translator configuration is therefore more desirable than that of previous efforts. However, the cost of the materials will be more expensive than previous efforts due to the high permanent magnet material mass.

5.7 Fourth Design with Optimisation Based on Transient Function Evaluations

With the project nearing completion, one more optimisation is performed to produce a design that can be built and tested. This optimisation is performed on the same configuration illustrated in Figure 5.17 and with the same optimisation variables as the Fourth Design illustrated in Figure 5.18 with one additional optimisation parameter, the driven current amplitude.

A consistent problem with the optimisation of the machine throughout this project is that of the time-dependent losses. These losses can be minimised to an extent by changing the design itself, however, the optimisation algorithm cannot account for these losses.

In this Fifth Design, it is therefore attempted to optimise the machine with a transient simulation as the method for solving function evaluations. This presents several challenges to the optimisation process, as discussed earlier in Section 5.5.2.

This optimisation could only be attempted in the final stage of this project due to the stable, existing sub-structure in place for the static optimisation. Within the debugging process, it can be assumed that the sub-structure is stable and that new issues arise only from the implementation of the transient simulation into the optimisation process. Had this been attempted from the start of the project, it would have been a difficult task to establish conditions wherein the optimisation algorithm could obtain convergence.

In available literature, an optimisation based in a static three dimensional finite element environment is very rare. Because of this, the pitfalls of this process are not well documented. An example of a transient three dimensional finite element optimisation could not be found in the field of electrical machine design that allows total geometric freedom to all the parameters as described in this thesis. It is for this reason that the transient finite element simulation was not incorporated into the optimisation from the beginning of the

project. There is no reference to what the possible problems of such an optimisation might be.

The required time for a function evaluation more than doubled for this transient optimisation. However, with the experience gained from all the previous optimisations, the debugging process progressed with surprisingly few errors.

On the second debugging run, the optimisation performed 1727 function evaluations in 144 iterations before an error was revealed. The duration of this debugging run was just short of a month. This is mentioned only because it is from this debugging run that the initial values were chosen for the final optimisation. Those initial values were at a near-optimum point. For this reason, the final optimisation converged after performing only 164 function

Table 5.14: Transient based optimisation results.

Mass Component	Value
Steel	3,8 kg
Copper	3,7 kg
Magnets	3,7 kg
Total	11,2 kg
Optimisation Parameter	Value
1) Inner stator radius	12,8 mm
2) Magnet height	26,4 mm
3) Coil height	46,5 mm
4) Outer stator height	17,0 mm
5) Magnet arc	30,0 deg
6) Pole arc	29,1 deg
7) Magnet length	105,2 mm
8) Pole length	21,9 mm
9) Current amplitude	4197 A
Performance Measure	Value
Input power	3349 W
Copper loss	234 W
Magnet eddy loss	66 W
Hysteresis loss	10 W
Core loss	4 W
Total loss	314 W
Output power	3035 W
Efficiency	90,6%
Current density	4,2 A/mm ²

evaluations in 13 iterations. The results of this optimisations are shown in Table 5.14.

This is a surprisingly short optimisation. It should also be noted, that even the debugging run started with initial values taken from the Fourth Design, which put it at a near optimum point as well.

In an attempt to maintain consistency throughout the design evolution, the desired efficiency of the optimisation was set at 90% as this generally relates to the obtained efficiency of previous efforts after the frequency dependent losses are taken into account.

In the case of this design, the magnets are proposed to be mounted on a hollow stainless steel shaft. The mass of this shaft (with a wall thickness of 2 mm) is taken into account as well as the eddy losses incurred within this shaft.

Figure 5.22 shows the two main loss components. The hysteresis and core losses are decoupled from the energy balance during transient analysis and only given as the single values of 10 W and 4 W, respectively by *MagNet*[®].

From the figure it can clearly be seen that the eddy losses in the magnets are much smaller in relation to the copper losses in the coils, compared to previous efforts. The obvious reason for this is that the optimisation could account for these losses and minimise them.

The eddy losses in the magnets contribute 21% of the total losses. While this is still not ideal, it is considered that this machine can practically be built and incorporated into a free-piston Stirling engine.

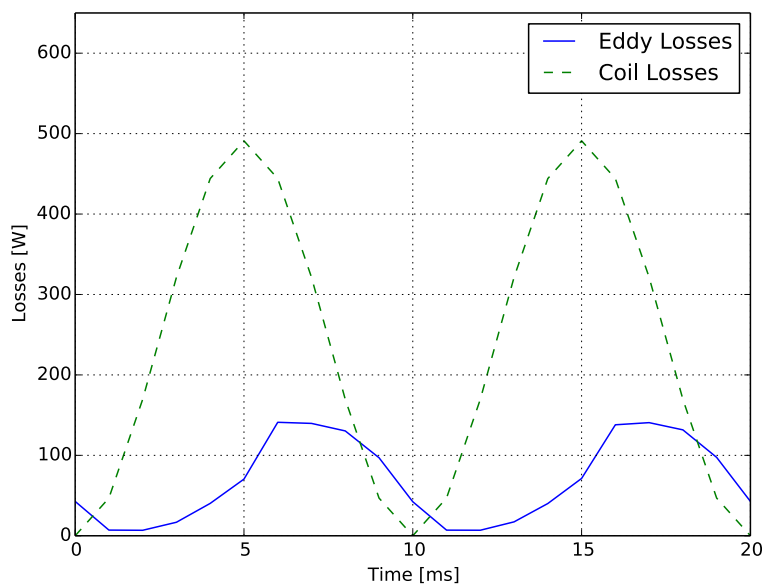


Figure 5.22: Comparison of loss components.

5.8 Design Review

In conclusion to this chapter a brief concluding overview of the design process is presented. This is done to illustrate the progress made by this project in the design of this specific electrical machine.

Table 5.15 shows a summary of the progress of the project and Table 5.16 shows a more detailed comparison. The initial design by Schutte, a machine design produced by a project that preceded this study, had a stroke length of 45 mm and magnets of a N42 grade. The First Design, with a stroke length of 30 mm and magnets of a N36 grade, improved on this design by eliminating a parasitic flux path in the translator.

Table 5.15: Summation of the design evolution.

Design	Target Efficiency [%]	Simulated Efficiency [%]	Mass [kg]	Specific Power [W/kg]
Initial Design	96	-	24,2	124
First Design	96	-	18,4	163
Second Design	96	87	13,1	208
Third Design	96	89	14,4	194
Fourth Design	96	92	13,2	217
Final Design	90	90	11,2	271

The Second Design was optimised, allowing the magnet lengths and stator stack length to be variables independent of the stroke length. To the author's knowledge, this is an innovation previously undocumented in this field.

The Third Design resolved issues in the manufacturability of the Second Design while maintaining similar output performance measures. Additionally, losses in the magnets were marginally reduced.

The Fourth Design further reduced losses in the magnets, improving the mechanical and the electrical properties by eliminating the laminate steel structure on the translator.

The final design is optimised while taking the loss mechanisms caused by time-varying magnetic flux into account. This design also takes losses incurred on the mechanical sub-structure into account.

Conclusively, the final design of this project has an output power of 3 kW at 90% efficiency, over a stroke length of 30 mm and a frequency of 50 Hz. This is accomplished with an active mass of 11,2 kg. The initial design had a longer stroke length and better magnets. It delivered similar output power characteristics, but with an active mass of 24,2 kg.

Table 5.16: Detailed design optimisation progress.

	Init	1	2	3	4	5
Steel Mass [kg]	12,4	10,5	6,2	8,6	4,8	3,8
Copper Mass [kg]	10,0	5,4	4,9	4,2	3,9	3,7
Magnet Mass [kg]	1,8	1,5	2,0	1,6	4,5	3,7
Total Mass [kg]	24,2	18,4	13,1	14,4	13,2	11,2
Material	N42	N35	N35	N35	N35	N35
Stroke [mm]	45	30	30	30	30	30
Input Power [W]	3125	3131	3134	3138	3131	3349
Losses [W]	125	125	409	345	261	314
Output Power [W]	3000	3006	2725	2793	2870	3035
Efficiency [%]	96	96	87	89	92	90
Current Density [A/mm ²]	2,4	2,57	2,97	3,2	3,3	4,2
Power Density [W/kg]	124	163	208	194	217	271

Chapter 6

A Brief Evaluation and Comparative Study

6.1 Overview

In this chapter, the main goal of the project is evaluated. The integration of the machine design into a free-piston Stirling engine is considered and the electrical and mechanical properties are reviewed with the application in mind.

The design is also directly compared to the linear oscillating machine of an industry leader, *Q-drives*, at the time of publication. The design that is compared to the commercial machine is the result of a new optimisation. This optimisation was performed to match the specifications of the commercial machine. The data sheet of the commercial machine is included in Appendix C.

6.2 Project Goal

At the onset of this project, it was proposed to design a linear oscillating electrical machine specifically to be integrated into a free-piston Stirling engine. In this regard, a single phase configuration was chosen with the current driven in-phase with the electromotive force. This decision was based on the mechanical interaction that this configuration has on the Stirling engine namely, that of a simple mechanical spring and damper combination.

Figure 6.1 shows the profile of the force with regard to time in green and the position with regard to time in blue. In-order to evaluate this machine, the two force components are separated.

The no-load force profile of the machine is shown in Figure 6.2. This force profile is obtained by simulation the machine under no-load conditions. That is, the amplitude of the

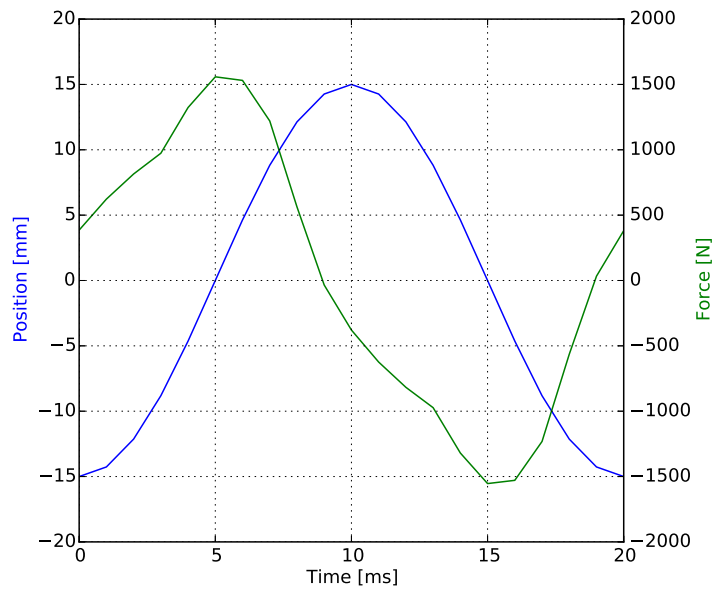


Figure 6.1: Full-load force profile with position.

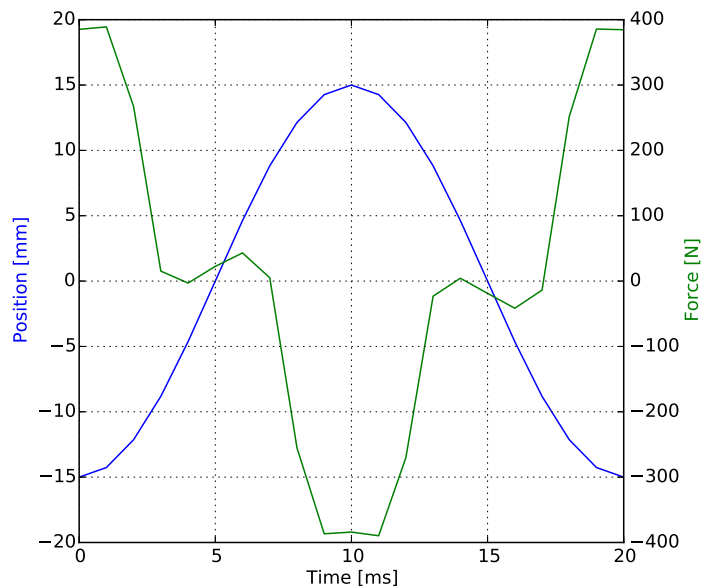


Figure 6.2: No-load force profile with position.

driven current is zero.

This force profile shown in Figure 6.2 is plotted as a function of time in green. This force profile follows the force profile of a non-linear mechanical spring. The position is plotted on the same axis as a function of time in blue.

With the time value of zero, the translator is in position "-15 mm" or displaced 15 mm

from the centre of the stator. At this position, there is a force of 385 N in the direction of the stator. At the time interval of 10 ms, the translator is displaced 15 mm to the other side of the stator with a resulting force in the opposite direction with a magnitude of 384 N.

The profile of the reluctance force curve with regard to time is highly non-sinusoidal. This is not unexpected and not specifically undesired, however, the irregular profile as the translator passes through the central position is not ideal.

In general, however, it appears that the reluctance forces of the machine can roughly be correlated to a spring with a spring constant, k of

$$k = \frac{F}{x} = \frac{385}{0,015} = 25,7 \text{ kN/m}. \quad (6.2.1)$$

For the translator combined with the shaft and power piston, an estimate of 6 kg can roughly be taken as the total motion component mass. From this mass, the natural frequency of the generator can be estimated at

$$f_n = \frac{1}{2\pi} \sqrt{\frac{k}{m}} = \frac{1}{2\pi} \sqrt{257006} = 10,4 \text{ Hz}. \quad (6.2.2)$$

This is only a very rough estimate, but a natural frequency of around 10 Hz is a good value. There are more spring components in the Stirling engine, such as the bounce space (which acts like a pneumatic spring) and the flexural bearings. As long as the addition of these spring components do not push the natural frequency beyond the 50 Hz mark (the design frequency), the design can be implemented.

A final addition to complete the design generally involves a "tuning spring" to adjust the natural frequency to the approximate operating frequency. This tuning spring can, however, only increase the natural frequency to a higher value and not decrease it to a lower value. This is why the low natural frequency of around an estimated 10 Hz for the linear generator is a positive aspect of the design.

While it is true that the natural frequency of the system can be lowered by increasing the suspended mass (this can simply be done by adding a "tuning weight"). This approach is not desirable. If the suspended mass needs to be increased to adjust the natural frequency, it would be better to increase the mass of the translator with electromagnetically active materials to improve on the linear alternator efficiency. Increasing the electromagnetically active mass on the translator however, would then effect the spring constant. This would result in a back-and-forth iterative design. It is therefore better to have a low spring constant than a high spring constant for the electrical machine.

The "final" spring constant, k_f for a machine operating at 50 Hz will have to be around

$$k_f = m(2\pi f)^2 = 6(2\pi 50)^2 = 592 \text{ kN/m}. \quad (6.2.3)$$

The additional spring elements in the Stirling engine can therefore roughly contribute 566 kN/m to the existing 26 kN/m without jeopardizing the design point. This resolves most of the issues regarding the irregular profile of the reluctance force shown in Figure 6.2. The reluctance forces of the electrical machine contributes less than 5% to the final spring forces. The specific profile of such a small contribution therefore becomes less important.

In-order to obtain the load-resulting force, the force resulting from the current driven in the coils, the no-load force profile is subtracted from the full-load force profile. Figure 6.3 shows this load-resulting force as a function of time in green, along with the velocity of the translator in blue.

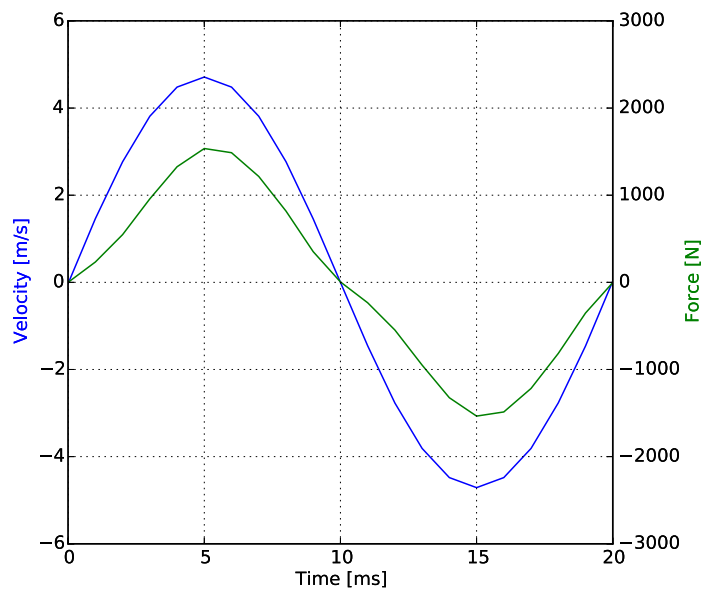


Figure 6.3: Load-resulting force profile with velocity.

From this figure, it is noted that the load-resulting force closely follows the characteristics of a damper. At the time interval of zero, the velocity of the translator is zero and the load-resulting force is likewise zero.

When the velocity is at its maximum, 4,7 m/s, at the time of 5 ms, a resulting force of 1536 N acts on the translator. At the optimum operating point, the machine can be represented by a damper with a damping coefficient of

$$c = \frac{F}{\dot{x}} = \frac{1536}{4,7} = 327 \text{ Nm/s.} \quad (6.2.4)$$

With regard to integration into a Stirling engine, more information is required to determine if this electrical machine can be successfully implemented with regards to the dampening capabilities.

Because the current is to be driven in phase with the electromotive force, the effective series inductance of the machine needs to be evaluated. It is evaluated to assess whether it falls within the acceptable range for the power electronic circuitry that is typically used. The effective series inductance is obtained by subtracting the no-load flux linkage from the full-load flux linkage and dividing this current resulting flux linkage by the instantaneous current value. These points are plotted in Figure 6.4.

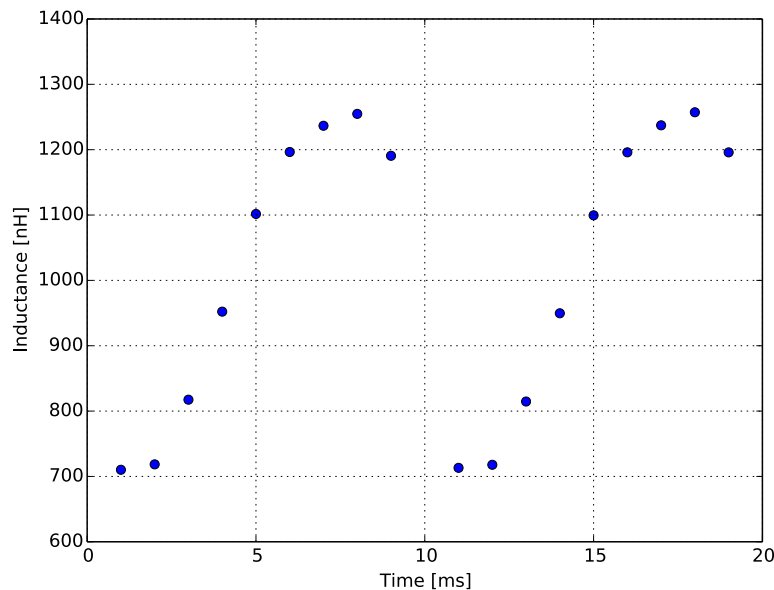


Figure 6.4: Single-turn equivalent series inductance.

This is a discrete curve because the current value is sometimes zero. The curve represents the single turn equivalent series inductance. It can be seen that the laminate iron core saturates at some intervals. This is to be expected, as the mass was minimised.

In construction, the inductance is scaled by the square of the number of turns in the coil. If 125 turns are chosen in construction, the effective series inductance, L , will be roughly 15,6 mH. At this stage it is unclear if this inductance value is acceptable as the power electronics are designed in a different project.

The correlating current amplitude would then be 34 A and the peak induced voltage, 380 V. The specific number of turns (125) are selected because this represents a good balance for the output parameters. A lower number of turns would have a lower voltage and a higher current. A higher number of turns would have a higher voltage and a lower current.

The peak electromotive force voltage, V_{EMF} is simulated at 240 V. Using this voltage and

the inductance, the root mean square of the short-circuit current can be calculated as

$$I_{RMS(s)} = \frac{V_{EMF}}{2\pi fL} = 49,0A. \quad (6.2.5)$$

which correlates to a peak short-circuit current of about 70 A. Figure 6.5 shows a magnetic flux plot in open-circuit. Here the magnetic flux path can clearly be seen to be oriented in an upwards direction.

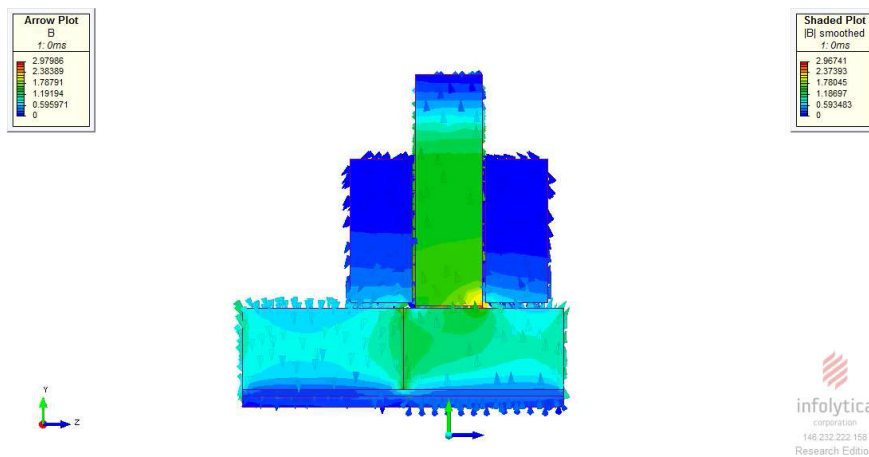


Figure 6.5: Open-circuit magnetic flux plot.

Figure 6.6 shows a magnetic flux plot under short-circuit conditions. It can clearly be seen that the magnetic flux plot in the stator is oriented in the opposing direction to the magnet beneath it. The magnetic flux plot on the magnet does not appear to be significantly effected by the short-circuit conditions.

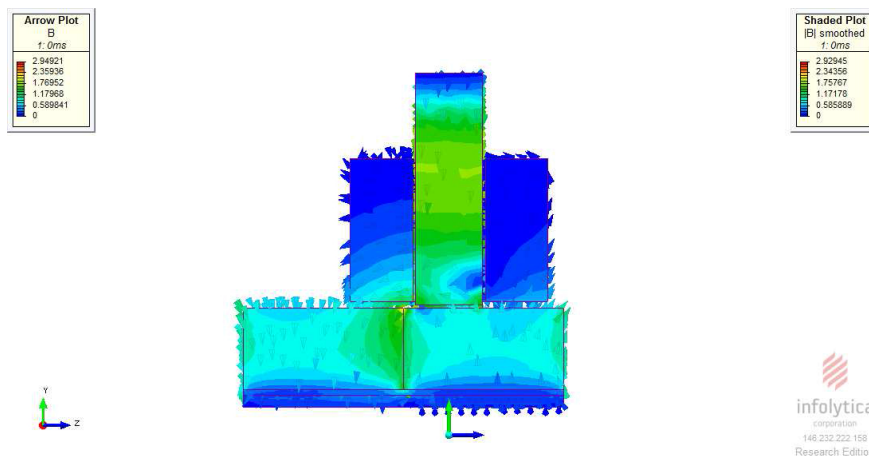


Figure 6.6: Magnetic flux plot under short-circuit conditions.

A built-in demagnetisation prediction function in *MagNet*[®] can produce a plot of problem areas concerning demagnetisation. Figure 6.7 shows such a plot under short-circuit

conditions.

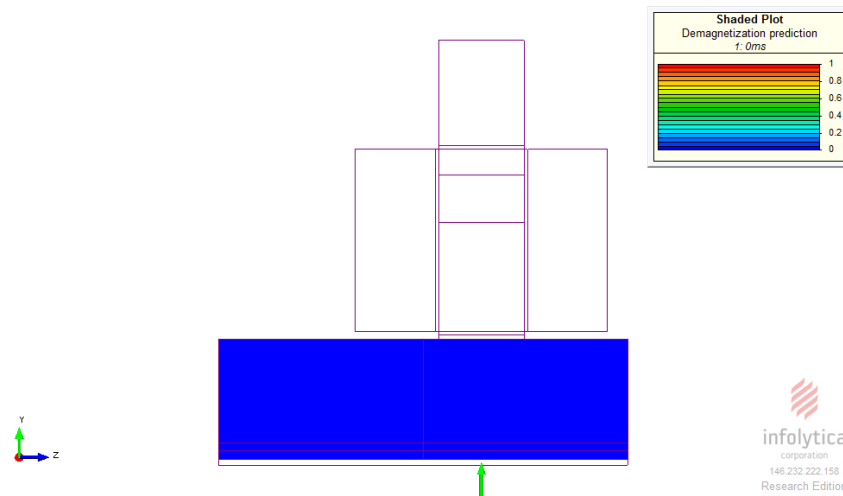


Figure 6.7: Predictive demagnetisation plot by *MagNet*® under short-circuit conditions.

When a current of 140 A is simulated, twice the magnitude of the short-circuit current, the *MagNet*®, demagnetisation predictive plot starts to show signs of demagnetisation. This is shown in Figure 6.8.

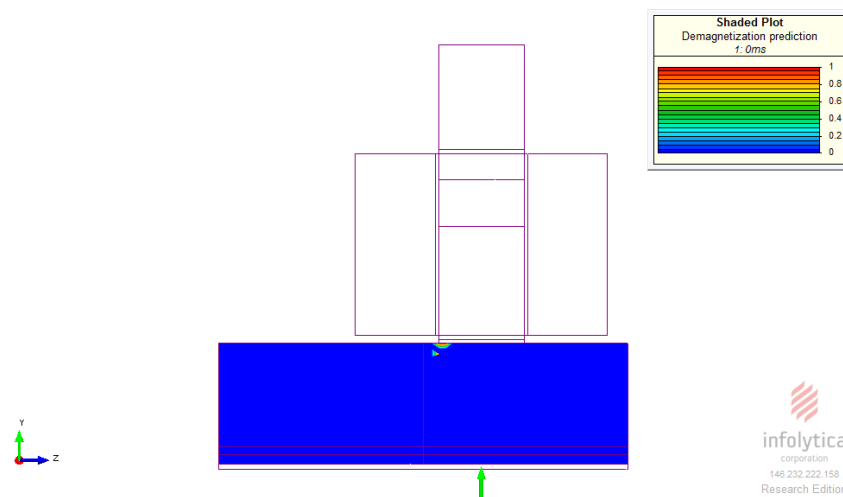


Figure 6.8: Predictive demagnetisation plot by *MagNet*® with a simulated current of 140 A.

Short-circuit conditions result in a current density of approximately $12,5 \text{ A/mm}^2$. Even though this should result in the coils overheating, it should be noticed that short-circuit conditions will result in the immediate stoppage of the power piston motion. The coils will therefore not overheat under short-circuit conditions.

6.3 Comparison with a Commercial Linear Oscillating Machine

As of 2008, the machine used by the *National Aeronautics and Space Administration* in prototypes for proposed Lunar and Mars surface station power plants, is designed by the commercial company, *Q-drives* [28].

No academic documentation on this machine could be found, however, from the company website [27], the specifications are given in Table 6.1 and shown in Appendix C.

Table 6.1: Q-drives machine specifications as shown on the website.

Specification	Value
Rated Power	5000 W
Stroke	25 mm
Frequency	60 Hz
Efficiency	80%-90%
Moving Mass	9,4 kg
Overall Mass	27,5 kg

Using these design input parameters, an optimisation was performed on the final design presented in this thesis. This optimisation was of a four-coil configuration and the optimisation was based on a transient simulation analysis. The results are shown in Table 6.2.

Table 6.2: Machine optimised to Q-drives' specifications.

Mass Component	Value
Steel	5,4 kg
Copper	5,2 kg
Magnets	6,2 kg
Total	16,8 kg
Performance Measure	Value
Input power	5579 W
Eddy losses	126 W
Total losses	560 W
Output power	5019 W
Efficiency	90,0 %
Current density	4,46 A/mm ²

The results compare well with the machines from *Q-drives*. With input parameters identical to the *Q-drives* machine achieves a total mass of 16,8 kg. The *Q-drives* machine lists a

total mass of 27,5 kg.

A few points need to be highlighted. First of all, the mass values listed by *Q-drives* are total mass values and the values listed by the author's design are only the electromagnetically active components. The images on the website [27], shows that the total mass of the *Q-drives* machine will not differ drastically from the active mass, but the total mass must of course be higher than the electromagnetically active mass.

The author's design has not been experimentally verified, while the *Q-drives* design is a commercially available product. As such, a direct comparison is unfair.

It should also be observed, however, that the author's design was optimised for 90% efficiency and the *Q-drives* design lists an efficiency ranging from 80% to 90%.

At these increased output power levels, a six-, eight- or even a ten coil configurations could perform better than the four coil configuration. This could be investigated in future.

6.3.1 Conclusive Remarks

It appears that this machine design has, in theory, achieved the goal of designing specifically for Stirling engine applications. The results appear to be that of a machine that can be practically implemented.

The design performs well, when compared to a machine that is commercially available. Specifically the power density of this design appears to be competitive. Experimental verification of these results are required.

Chapter 7

Prototype Design

7.1 Overview

In this section, the design and construction of a prototype machine is described. Design challenges are described and shortcomings of previous projects are studied. A new approach to the problem is evaluated and the implementation thereof is described.

7.2 Design Challenges

Short stroke linear machines are difficult test. This is primarily due to the nature of the mechanical input. The easiest way to describe these difficulties is to relate it to a rotating machine.

If one considers rotating machines, the mechanical input has forces that relate to a torsion around a fixed axis. This torsion is generally uniform in the direction of its application for relatively long periods of time.

Consider now, a rotating machine that needs to start up, brake and stop at a specific angle, start up in the opposite direction, brake and then stop back at it's original staring position fifty times in one second. A system such as this deviates from what is generally expected in the testing of electrical machines.

A test bed for linear machines therefore has to be designed that deals with problems normally not considered in the testing of electrical machines. It is observed in literature that many projects fall short of testing linear machines at the design frequency for this reason [26], [32].

There are three test bed configurations that are considered in this study as possible solutions to the problems involved in testing these machines. A crank mechanism with a rotating electrical machine to drive it is considered in Section 7.2.1. A rhombic drive with a rotating electrical machine to drive it is considered in Section 7.2.2 and a linear test bed setup considered in Section 7.2.3.

7.2.1 Crank Type Test Bed

A crank type test bed is a relatively simple solution to the problem. A rotating electrical machine can be fixed to a fly-wheel and crank with the translator of the linear machine fixed to the crank.

Such a test set-up is relatively inexpensive and holds the advantage that the stroke length is fixed. Because the stroke length is fixed, such a set-up has an inherent "over-stroke" protection and test results will consistently be on the correct stroke length.

The crank mechanism can be fitted with a counter-weight that directly compensates for the linear forces involved in testing with regards to the horizontal direction. However, such a configuration will then be inherently unbalanced in the vertical direction.

High frequency testing of such a configuration is problematic. The vibration resulting from a vertically unbalanced system can make it dangerous. This was specifically a problem in project that precedes this study. The mechanical set-up for the testing of the Initial Design of Section 5.2, documented by Shutte [32] was partially designed by the author. This set-up was unable to exceed a frequency of 10 Hz because of the forces relating to the vertical unbalance. Figure 7.1 shows the test set-up for the Initial Design.



Figure 7.1: Test set-up for the Initial Design by Schutte.

Considering that low frequency test results for the Initial Design already verify some of the simulated results in the preceding study, repeating such a test bed design would serve little purpose. One of the focus points of the study described in this thesis is that of the time dependent losses. If the set-up is incapable of high frequency testing, the time dependent losses cannot be investigated experimentally.

7.2.2 Rhombic Drive Test Bed

A rhombic drive is similar to a crank type set-up, excepting that it employs two counter balance elements. These counter balance elements are situated above each other and mechanically linked to each other with gears. Pivoting arms then connect to the shaft with the translator of the linear machine.

A rhombic drive can be designed to be perfectly balanced along both the vertical and horizontal plane. The stroke length, as with a crank type set-up, can be fixed. Such a test bed would be the safest design for testing linear machines. Testing would be relatively straight forward in such a set-up. There are however issues with such a set-up.

A rhombic drive has many mechanical components and this makes it the most expensive design for a test bed. Components such as the gear connected counter balance elements would have to be contained within a casing that contains lubrication. Such a casing would have to be sealed and specialised seals would have to facilitate shaft movement in and out of the casing.

The design and fabrication costs of a rhombic test bed is predicted to exceed that of the alternatives by a significant margin. It is because of the high costs involved that this configuration is disqualified.

7.2.3 Linear Test Bed

A linear test bed set-up is proposed that employed a linear electric machine to test the linear electric generator. Such a test set-up could be significantly smaller than the alternatives.

In a linear test bed, there is only one moving part as the translator of the motor can be fixed to the same shaft as the translator of the generator. The design and fabrication costs of such a set-up is predicted to be significantly lower than that of the alternatives because it can consist of significantly fewer parts.

Even though the unbalanced forces on the shaft is predicted to present problems at high frequency testing, the mass of the unbalanced shaft is predicted to be lower than that of the crank set-up and can consequently be manageable.

For this set-up, however, the stroke length is not fixed and this could result in problems with the testing of the machine. Regardless, this test set-up was chosen to be designed and manufactured because of the lower costs involved.

7.3 Prototype Construction

The schematics of the test bed set-up is included in Appendix D. In this section, the construction of the test bed and prototype is described. There were problems in manufacturing

process that inhibited progress. These problems were eventually overcome with certain drawbacks. Due to time constraints, however, the machine could not be tested in time.

7.3.1 Stator Construction

As mentioned in Section 5.3, the stator laminations are segmented. This facilitated geometric freedoms in optimisation that would not have been possible if a solid stator lamination design had been employed.

Figure 7.2, shows the segmented stator laminations. These laminations are located on dowel pins and inserted into the coils. The coils are wound onto perspex bobbins and secured into place by bolts after the stator laminations have all been placed.

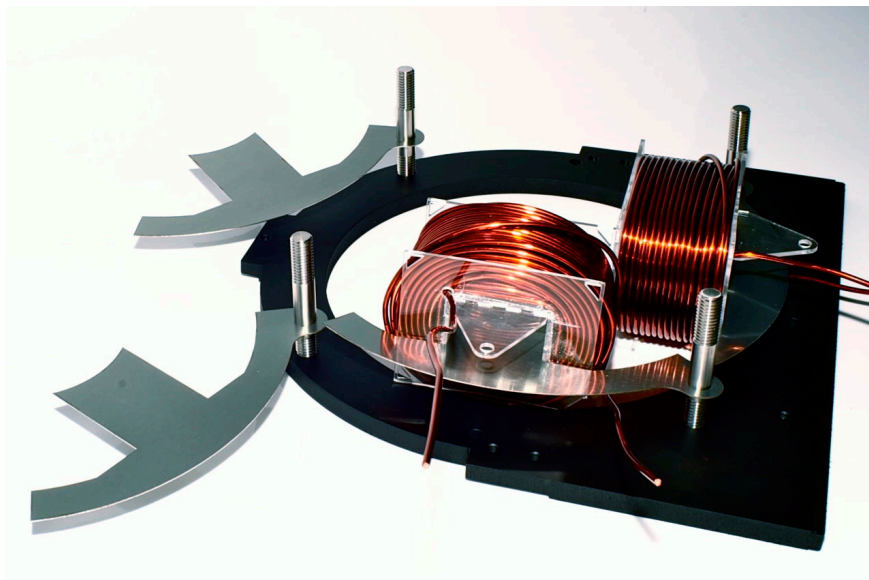


Figure 7.2: Segmented stator lamination construction.

The stator laminations are placed in an overlapping pattern. For one coil then, a lamination is inserted into the coil with the hole that locates it on the dowel to one side. The next lamination is inserted with the hole on the other side, locating it on a different dowel than the preceding lamination.

Figure 7.3 shows the completed stator. Here it can be seen how the coil bobbins are bolted into place and the series coil connections are made.

7.3.2 Translator Construction

The translator construction presented a significant problem in manufacture. It is because of this problem that the prototype could not be tested in time.

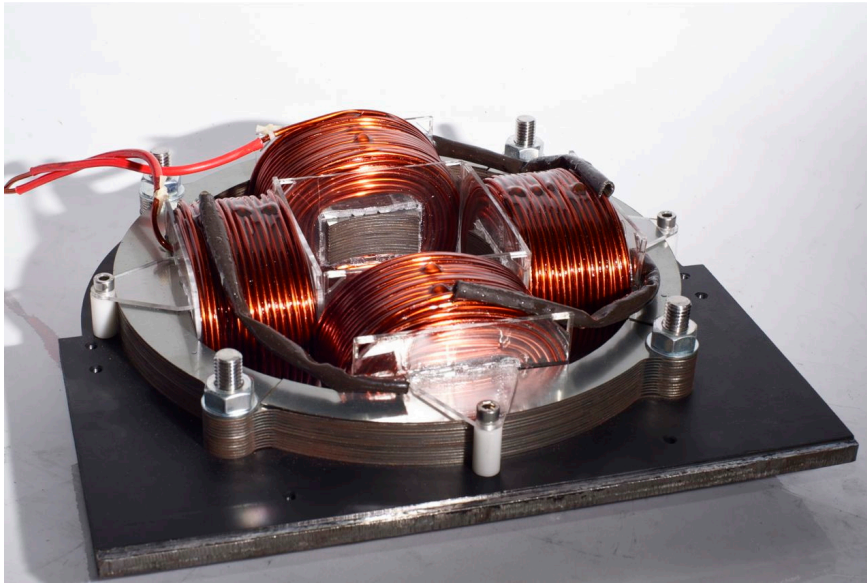


Figure 7.3: Completed stator with coils secured in place.

In the mechanical design, it is proposed to fabricate a stainless steel magnet carrier. The magnets would then be secured into place using an industrial adhesive similar to what was done in the construction of the Initial Design prototype of Schutte. This process is shown in Figure 7.4.



Figure 7.4: Process of fixing magnets in place with industrial adhesive.

The problem was that the author did not consider that the quasi-Halbach formation of the magnet configuration would exert forces that strive to break this formation. These forces are significant in magnitude.

Two attempts were made to overcome this problem. Both of the attempts were unsuc-

cessful.

The first attempt was to design radial clamps to hold the magnets in position. These clamps consist of stainless steel bars that are positioned above the magnets that are not situated across from the stator teeth. The stainless steel bars are then radially bolted into a collar that is placed over the ends of the magnet carriers.

If the bars are thin enough, they would not inhibit the operation of the machine. This is because they are located in the gap between two of the stator teeth. With a low profile, these bars would then likewise not interfere with the coils.

The obvious electrical problem with such a clamp configuration is that the stainless steel bars will enclose an electrical conduction path around the flux-linkage of the machine. This will essentially create a short circuit. In order to overcome this problem, engineering plastic components were manufactured to electrically isolate the stainless steel bars.

The problem with this proposed solution was two-fold. Firstly, it was difficult to locate these bars with precision because they had no angular mechanical reference to the magnets. Secondly, the radial clamps could not hold all the magnets in place, only half of the magnets.

Due to these two problems, the radial clamps ultimately proved to be a failure. Figure 7.5 shows an attempt at implementing the radial clamps.



Figure 7.5: Radial magnet clamping technique in the attempted process of assembly.

The second attempt to try and solve the problem of fixing the magnets in place, was to construct an axial clamp. In this proposed solution, hose clamps typically used in irrigation applications would radially force the magnets into position. With the magnets properly located, clamps would be fitted to the ends of the assembly, forcing the magnets towards each other in the axial direction. The friction between the clamps and the magnets could

then proposedly hold the assembly in place.

The end-rings used in the radial clamping attempt had holes drilled and tapped in six places along the axis. Mild steel disks would be located against the end-rings and bolts would protrude through the end-ring holes and push against the mild steel disks.

Between the mild steel disks and the magnets, aluminium disks would be placed. The aluminium disks would then deform to create a flush surface with all the individual magnets. The reason why the mild steel disks were placed between the bolts and the aluminium disks, was to prevent the bolts from simply piercing through the softer aluminium disks.

In the process of forcing the magnets into place, four hose-clamps were used. This is illustrated in Figure 7.6. The forces exerted by the magnets were of such a magnitude that four 10 mm bolts were ruined in the process. Two of these bolts were high tensile bolts. The ruined bolts are shown in Figure 7.7.

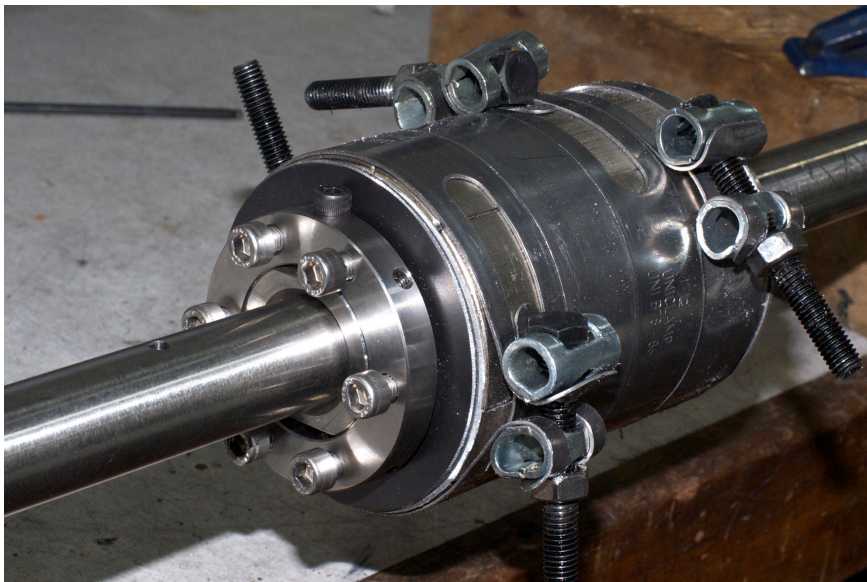


Figure 7.6: Process of locating the magnets with the use of hose clamps.

Ultimately this attempt resulted in failure. When the hose clamps were removed, the magnets slowly shifted out of position over a period of half an hour. This is shown in Figure 7.9.

As is the case in engineering problems when faced with a problem without a foreseeable practical solution, the definition of the problem must be revisited. This was the next step in the manufacture of the translator.

The only foreseeable option was to try and work with the magnetic forces instead of against these forces. In order to do this, regrettably, the structure of the translator had to be changed.



Figure 7.7: Bolts ruined in the process of locating the magnets with hose clamps.

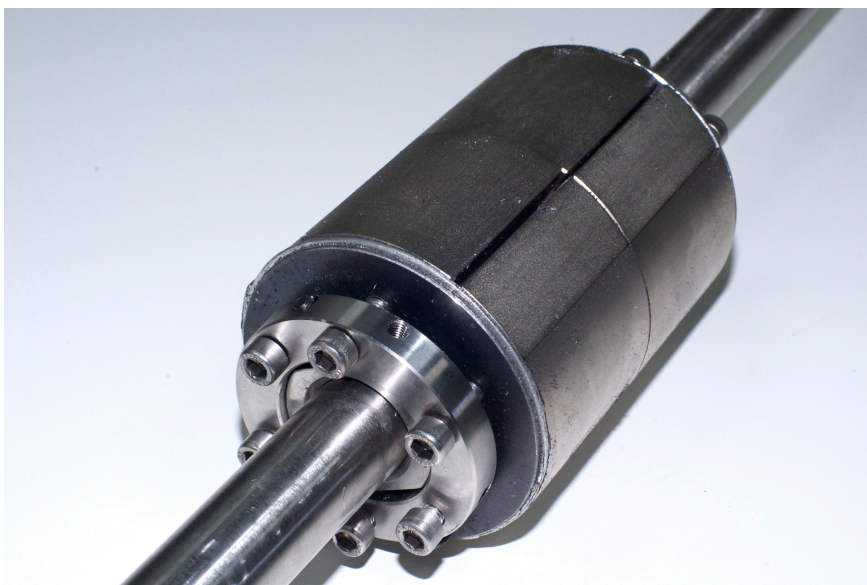


Figure 7.8: Failure of the radial clamping technique.

Mild steel wedges were fabricated to replace half of the magnets. In doing so, the quasi-Halbach configuration of the magnets would be lost, but possible test results could be performed on the electrical machine. These test results would have to be compared to simulations run of the design with representative material properties. Figure 7.9 shows the modified translator structure with mild steel wedges replacing some of the magnets.

Never the less, test results could still be performed on a machine that is fairly comparable to the one optimised in this project. Unfortunately this never occurred because there was not enough time to perform them.



Figure 7.9: Completed translator with mild steel wedges replacing some of the magnets.

Figure 7.10 shows the prototype test bed. The test bed is complete with the exception of one translator and a positional sensor. Load-cells suspend the stator of the generator. This was done so that the load cells remain stationary and do not effect the stiffness of the shaft.

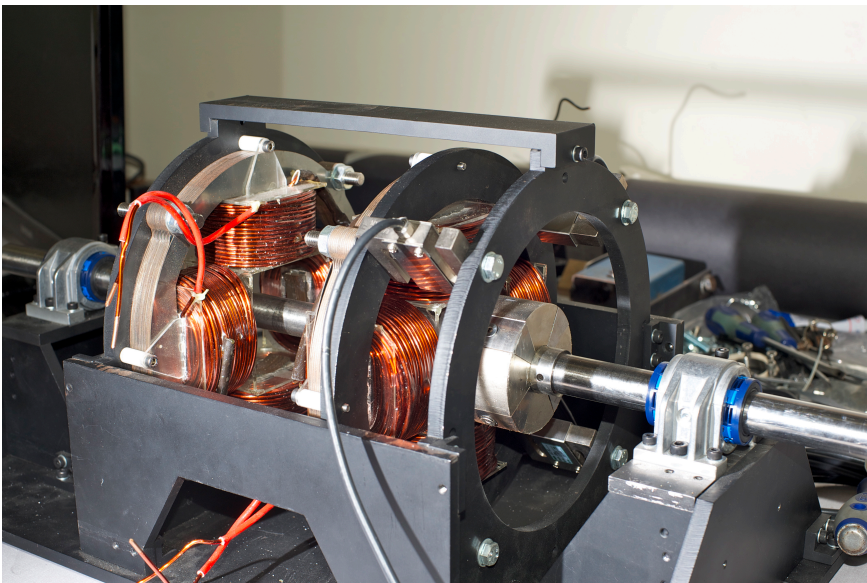


Figure 7.10: Partially completed prototype test bed.

7.4 Conclusion

The construction of the prototype and test bed could not be completed in time to test the design. The reason for this is because the quasi-Halbach magnet configuration presented

unexpected difficulties in assembly. The structure of the translator was changed and finally completed.

Because of the modified translator structure, future test results would have to be compared to a modified design of the optimised machine. This is not ideal. Future projects need to account for the forces exerted by a quasi-Halbach magnet configuration in the mechanical design.

Chapter 8

Conclusions and Recommendation

8.1 Analytical Machine Simulation

The process of optimising a machine using a three dimensional optimisation algorithm in conjuncture with an optimisation algorithm is a tedious task.

There are many pit-falls and this should not be attempted unless it is the only possible way of simulating a machine design. This project should have given more attention to analytical simulation approaches.

Proposed future work is to thoroughly investigate the possibility of representing transverse flux linear machines with an analytical simulation technique. The most promising method is a magnetic equivalent circuit representation.

8.2 Optimisation Parameters

One of the parameters that has the most significant influence on the optimisation of this type of machine is the profile of the driven current. The current is driven in the machine using power electronics. Because of this, the profile could arguable follow almost any curve.

Should the profile of the driven current become an optimisation variable, it is expected to see profound effects on the machine optimisation. Consider that the optimisation strives to create best possible output power for a given mass.

If the driven current is sinusoidal, the best output power will be delivered by a sinusoidal voltage curve. This results in a sinusoidal flux-linkage curve as the best possible solution.

The flux-linkage curve is dependent on the machine geometry. Therefore, the shape of the geometry is indirectly determined by the profile of the driven current waveform.

Should the driven current waveform become a free variable, the mass of the machine might be minimised even further. Or, arguably, the machine could produce a force profile

that is better suited to this specific application. This would have to be done using a more representative curve to describe the position of the translator.

The incorporation of a more representative positional curve can easily be implemented. The allowance to present the driven current profile in an arbitrary, variable profile is likewise easy to implement in optimisation. This is because of the instantaneous power model implemented in this project.

8.3 Summary

In this thesis a description of free-piston Stirling engines was presented. The applications of this technology were then discussed.

The development of linear electric machines for free-piston Stirling engines was discussed. A classification structure for these machines was created.

The mathematical simulation and modelling of a transverse flux linear machine was then evaluated and the automated process of simulating a machine for different geometric configurations was discussed.

Different optimisation approaches were described. The selected algorithm, sequential quadratic programming was then evaluated. The implementation of an automated optimisation process was then presented.

The design evolution of a transverse flux topology was then described. The description was based on the results from around forty optimisations.

The resulting design from this evolutionary process was compared to a commercially available machine. The design compared well with this machine.

A test bed incorporating a prototype mechanical design was completed. Difficulties in construction prevented the prototype from being tested in time.

Bibliography

- [1] R. Stirling, "Stirling air engine and the heat regenerator," Patent no. 4081, 1816.
- [2] D. Shrestha, "Numerical and experimental studies on free piston stirling engines," Master's thesis, University of Maryland, College Park, Md., 2012.
- [3] W. Beale, "Free piston stirling engines-some model tests and simulations," *SAE Technical Paper 690230*, 1969.
- [4] W. T. Beale, "Stirling cycle type thermal device," US Patent 3,552,120, Jan 1971.
- [5] J. M. Strauss, "Direct piston displacement control of free-piston stirling engines," Ph.D. dissertation, Stellenbosch University, Stellenbosch; South Africa, 2013.
- [6] R. Redlich and D. Berchowitz, "Linear dynamics of free-piston stirling engines," *Proceedings of the Institution of Mechanical Engineers, Part A: Journal of Power and Energy*, vol. 199, no. 3, pp. 203–213, 1985.
- [7] N. W. Lane and W. T. Beale, "Free-piston stirling design features," in *Eighth International Stirling Engine Conference*, 1997.
- [8] J. S. Rauch, M. D. Kankam, W. Santiago, and F. J. Madi, "A free-piston stirling engine/linear alternator controls and load interaction test facility," National Aeronautics and Space Administration, Cleveland, OH (United States). Lewis Research Center, Cleveland, OH; United States, Tech. Rep., 1992.
- [9] S. Qiu, D. L. Redinger, and J. E. Augenblick, "The new generation Infinia free-piston Stirling engine for micro-CHP and remote power applications," *proceedings of the 3rd annual IECEC, AIAA-2005-55-17, San Francisco, CA*, 2005.
- [10] D. Berchowitz, M. Richter, and D. Shade, "Development and performance of a 3 kw (e) air charged free-piston stirling engine with linear alternator," in *22nd Intersociety Engine Conversion Engineering Conference*, pp. 1835–1840, 1987.
- [11] M. T. Incorporated, "Conceptual design of an advanced striling conversion system for terrestrial power generation," Technical Report, Latham, New York, Jan 1988.
- [12] R. D. J.R. Bean, "Technical status of the dish/stirling joint venture program," DOE, Tech. Rep., 1995.

-
- [13] W. A. Wong, D. J. Anderson, K. L. Tuttle, and R. C. Tew, "Status of nasa's advanced radioisotope power conversion technology research and development," NASA Glenn Research Center, Cleveland, Ohio, Tech. Rep., 2006.
- [14] J. A. Corey, "Backing into the business: An entrepreneur in thermoacoustics," in *The 17th International Congress on Sound Vibration*, July 2010.
- [15] V. J. Lyons and A. S. Levine, "An overview of nasa's contributions to energy technology," in *Sixth International Energy Conversion Engineering Conference and Exhibit (IECEC)*, Cleveland, Ohio, July 2009.
- [16] W. T. Beale, "Some stirling engine designs for solar energy - concepts, analysis and test results (hermetically sealed stirling engines)," in *Solar/Energy Conference*, 1977.
- [17] L. G. Thieme and J. G. Schreiber, "Nasa grc technology development project for a stirling radioisotope power system," in *Energy Conversion Engineering Conference and Exhibit, 2000.(IECEC) 35th Intersociety*, vol. 1. IEEE, pp. 249 – 258, 2000.
- [18] K. Lee and W. Toscano, "Preliminary design of linear alternator dynamometer for free piston stirling engines. final report," Aspen Systems, Inc., Marlborough, MA (USA), Tech. Rep., 1985.
- [19] S.-Y. Kim and D. M. Berchowitz, "Specific power estimations for free-piston stirling engines," in *4th International Energy Conversion Engineering Conference (IECEC)*, 2006.
- [20] M. Dhar, J. Rauch, S. Huang, and R. Bolton, "Space power demonstration engine linear alternator dynamometer test results," in *Energy Conversion Engineering Conference, 1989. IECEC-89., Proceedings of the 24th Intersociety*. IEEE, pp. 1103–1107, 1989.
- [21] P. Zheng, X. Gan, and L. Li, "Analysis and design of a high power density axial flux permanent magnet linear synchronous machine used for stirling system," in *Pervasive Computing Signal Processing and Applications (PCSPA), 2010 First International Conference on*. IEEE, pp. 398–401, 2010.
- [22] S. Gerber, "A finite element based optimisation tool for electrical machines," Master's thesis, Stellenbosch: University of Stellenbosch, Stellenbosch; South Africa, 2011.
- [23] I. Boldea and S. Nasar, *Linear electric actuators and generators*. Cambridge University Press, 1997.
- [24] J. Schutte and J. Strauss, "Optimisation of a transverse flux linear pm generator using 3d finite element analysis," in *Electrical Machines (ICEM), 2010 XIX International Conference on*. IEEE, pp. 1–6, 2010.
- [25] J. Schutte, L. Joubert, and J. Strauss, "Constrained optimisation of a transverse flux pm linear generator," in *Electrical Machines (ICEM), 2012 XXth International Conference on*. IEEE, pp. 595–599, 2012.
- [26] A. Cosic, C. Sadarangani, and F. Carlsson, "A novel concept of a transverse flux linear free-piston generator," in *KTH, School of Electrical Engineering (EES), Electrical Machines and Power Electronics*, 2005.

- [27] (2014, Oct). [Online]. Available: <http://www.qdrive.com/UI/Components-STAR-Motors-Alternators-STAR-MotorsAlternators-1S297MA.aspx?type=3mclid=115pcid=115ccid=116pid=18>
- [28] S. M. Geng, L. S. Mason, R. W. Dyson, and L. B. Penswick, "Overview of multi-kilowatt free-piston stirling power conversion research at glenn research center," Space Technology and Applications International Forum, STAIF-2008,, Albuquerque, NM; United States, Tech. Rep., Feb 2008.
- [29] G. A. Yarr and J. A. Corey, "Linear electrodynamic machine," US Patent 5,389,844, Feb 1995.
- [30] T. Govindaraj, D. Chatterjee, and A. K. Ganguli, "Development, analysis and control of an axial flux permanent magnet linear oscillating motor suitable for short strokes," in *Industrial Electronics, 2009. ISIE 2009. IEEE International Symposium on*. IEEE, pp. 29–34, 2009.
- [31] R. Redlich, "A summary of twenty years experience with linear motors and alternators." Nagasaki, Japan: LDIA, Linear Drives for Industry Applications, May 1995.
- [32] J. Schutte, "Optimisation of a transverse flux linear pm generator using 3d finite element analysis," Master's thesis, Stellenbosch University, Stellenbosch; South Africa, 2011.
- [33] A. Cosic, "Analysis of a novel transversal flux machine with a tubular cross-section for free piston energy converter application," Ph.D. dissertation, KTH, Electrical Machines and Power Electronics, qC 20101102, 2010.
- [34] S. P and P. N, "Analytical computation method of transverse flux permanent magnet excited machines via nodal analysis," in *Electrical Machines (ICEM), 2014 XXIIth International Conference on*. IEEE, pp. 405–410, 2014.
- [35] G. Venter, "Review of optimization techniques," *Encyclopedia of aerospace engineering*, 2010.
- [36] K. Schittkowski and Y.-X. Yuan, "Sequential quadratic programming methods," *Wiley Encyclopedia of Operations Research and Management Science*, 2010.
- [37] V. N, *Multidiscipline Design Optimization*. Colorado Springs, CO: Vanderplaats Research and Development, Inc., 2007.
- [38] M. Powell, "A fast algorithm for nonlinearly constrained optimization calculations," in *Numerical Analysis*. Springer, 1978.
- [39] D. A. Wills and M. J. Kamper, "Reducing pm eddy current rotor losses by partial magnet and rotor yoke segmentation," in *Electrical Machines (ICEM), 2010 XIX International Conference on*. IEEE, 2010.
- [40] K. F. Rasmussen, J. H. Davies, T. Miller, M. McGelp, and M. Oлару, "Analytical and numerical computation of air-gap magnetic fields in brushless motors with surface permanent magnets," *Industry Applications, IEEE Transactions on*, vol. 36, no. 6, pp. 1547–1554, 2000.
- [41] C. H. Simmons and D. E. Maguire, *Manual of Engineering Drawing to British and International Standards*, 2nd ed. Linacre House, Jordan Hill, Oxford: Elsevier Newnes, 1995.

- [42] D. J. Inman and R. C. Singh, *Engineering vibration*. Upper Saddle River: Prentice Hall, 2001.
- [43] D. Zill, W. S. Wright, and M. R. Cullen, *Advanced engineering mathematics*. Jones Bartlett Learning, 2011.

Appendices

Appendix A

Dynamics of Resonant Motion

A.1 Principals of Undamped Harmonic Motion in Free Vibration

In order to illustrate the nature of free piston dynamics, the modelling technique and general convention of Inman [42], will be used. Consider a simple spring-mass system. The force exerted by an ideal, linear spring is the product of the specific spring's spring constant, k , and the displacement relative to the spring's relaxed length namely,

$$F_k = kx. \quad (\text{A.1.1})$$

If the spring-mass system is disturbed from its resting position and Newton's second law is applied, we find

$$\sum F_x = m\ddot{x} \quad (\text{A.1.2})$$

$$\Rightarrow -kx(t) = m\ddot{x}(t). \quad (\text{A.1.3})$$

In an ideal, frictionless environment, it can be deduced that the mass will move in an oscillatory manner. The position in time can therefore be expressed as

$$x(t) = A \sin(\omega t + \phi), \quad (\text{A.1.4})$$

where A denotes the amplitude, ω , the angular frequency and ϕ , the phase angle determined by the initial conditions of the system. The velocity can thus be derived from the position as

$$\dot{x}(t) = \omega A \cos(\omega t + \phi) \quad (\text{A.1.5})$$

and likewise the acceleration can be derived from the velocity

$$\ddot{x}(t) = -\omega^2 A \sin(\omega t + \phi). \quad (\text{A.1.6})$$

When Equations A.1.4 and A.1.6 is substituted into A.1.3,

$$-kA \sin(\omega t + \phi) = -m\omega^2 A \sin(\omega t + \phi) \quad (\text{A.1.7})$$

$$\Rightarrow (m\omega^2 - k) A \sin(\omega t + \phi) = 0. \quad (\text{A.1.8})$$

The term, $A \sin(\omega t + \phi)$, cannot be zero for the entire defined time period ($t > 0$), it is therefore the other term that needs to equate to zero, i.e.

$$\frac{k}{m} = \omega^2, \quad (\text{A.1.9})$$

which defines ω_n as

$$\omega = \omega_n = \sqrt{\frac{k}{m}}. \quad (\text{A.1.10})$$

ω_n , is the natural-, or harmonic frequency. This is the frequency at which the system will oscillate if disturbed from rest, regardless of the initial conditions described by A and ϕ . It can be noted that these equations of motion imply indefinite movement, which is certainly not the case. A dampening effect needs to be considered to accurately model reality.

A.2 Principals of Damped Harmonic Motion in Free Vibration

If a term, $c\dot{x}(t)$, is added to the model, the theory of differential equations suggest that the motion will eventually decay [42]. c is a constant called the damping coefficient. The product of the velocity and the damping coefficient, models a viscous damping force, F_c .

$$F_c = c\dot{x}(t) \quad (\text{A.2.1})$$

The force balance from Newton's second law that includes this damping force becomes

$$-F_c - F_k = m\ddot{x}, \quad (\text{A.2.2})$$

or in the standard form

$$m\ddot{x}(t) + c\dot{x}(t) + kx(t) = 0. \quad (\text{A.2.3})$$

Because A.2.3 is a homogeneous linear equation with constant coefficients, m , c and k , an exponential function or a combination of exponential functions exist that will solve it [43]. The expression of $x(t)$ can therefore be expressed as

$$x(t) = ae^{\lambda t}, \quad (\text{A.2.4})$$

with a and λ as non-zero constants that define the behaviour subject to the initial conditions. Expressions for $\dot{x}(t)$ and $\ddot{x}(t)$ then become

$$\dot{x}(t) = \lambda ae^{\lambda t} \quad (\text{A.2.5})$$

and

$$\ddot{x}(t) = \lambda^2 ae^{\lambda t}. \quad (\text{A.2.6})$$

Substituting Equations A.2.4, A.2.5 and A.2.6 into Equation A.2.3, yields

$$m\lambda^2 ae^{\lambda t} + c\lambda ae^{\lambda t} + kae^{\lambda t} = 0. \quad (\text{A.2.7})$$

Because $ae^{\lambda t} \neq 0$ for all Real values of t , Equation A.2.7 can be simplified to

$$m\lambda^2 + c\lambda + k = 0. \quad (\text{A.2.8})$$

This equation, the auxiliary equation, grants insights to the dynamics of the system. Solving it yields

$$\lambda_{1,2} = -\frac{c}{2m} \pm \frac{1}{2m} \sqrt{c^2 - 4km}. \quad (\text{A.2.9})$$

If c_r , the critical dampening is defined as

$$c_r = \sqrt{4km} = 2m\omega_n \quad (\text{A.2.10})$$

and ζ , the dampening ratio is defined as

$$\zeta = \frac{c}{c_r}, \quad (\text{A.2.11})$$

it becomes clear, when substituting Equations A.2.10 and A.2.11 into Equation A.2.9, that ζ determines whether the roots are complex or real. This can be seen from

$$\lambda_{1,2} = -\zeta\omega_n \pm \omega_n \sqrt{\zeta^2 - 1}. \quad (\text{A.2.12})$$

Three distinct conditions now become apparent: $0 < \zeta < 1$ for under damped motion, $\zeta = 1$ for critically damped motion and $\zeta > 1$ for over-damped motion. If the mass, m , and the spring constant, k , remain unchanged but the damping coefficient is variable, ζ , likewise becomes a variable and the different conditions can be applied to the system as a function of the variable damping coefficient.

A.2.1 Under Damped Motion is Free Vibration ($0 < \zeta < 1$)

In the case of under damped motion, with $0 < \zeta < 1$, Equation A.2.12, will result in a complex conjugate root pair, i.e.

$$\omega_n \sqrt{\zeta^2 - 1} = \omega_n \sqrt{(-1)(1 - \zeta^2)} = i\omega_n \sqrt{1 - \zeta^2} \quad (\text{A.2.13})$$

$$\Rightarrow \lambda_1 = -\zeta\omega_n - i\omega_n \sqrt{1 - \zeta^2} \quad (\text{A.2.14})$$

$$\Rightarrow \lambda_2 = -\zeta\omega_n + i\omega_n \sqrt{1 - \zeta^2}. \quad (\text{A.2.15})$$

Let ω_d , the damped natural frequency be defined as

$$\omega_d = \omega_n \sqrt{1 - \zeta^2}. \quad (\text{A.2.16})$$

With the roots now known, Equation A.2.4 can be expressed as:

$$x(t) = a_1 e^{-\zeta\omega_n t - i\omega_d t} + a_2 e^{-\zeta\omega_n t + i\omega_d t} \quad (\text{A.2.17})$$

$$\Rightarrow x(t) = e^{-\zeta\omega_n t} (a_1 e^{-i\omega_d t} + a_2 e^{i\omega_d t}) \quad (\text{A.2.18})$$

$$\Rightarrow x(t) = e^{-\zeta\omega_n t} [a_1 \cos(\omega_d t) - ia_1 \sin(\omega_d t) + a_2 \cos(\omega_d t) + ia_2 \sin(\omega_d t)] \quad (\text{A.2.19})$$

$$\Rightarrow x(t) = e^{-\zeta\omega_n t} [(a_2 + a_1) \cos(\omega_d t) + i(a_2 - a_1) \sin(\omega_d t)]. \quad (\text{A.2.20})$$

Now the following substitutions are chosen, namely

$$A_1 = a_2 + a_1 \quad (\text{A.2.21})$$

$$iA_2 = i(a_2 - a_1) \quad (\text{A.2.22})$$

$$\Rightarrow A_2 = a_2 - a_1 \quad (\text{A.2.23})$$

$$\Rightarrow x(t) = e^{-\zeta\omega_n t} [A_1 \cos(\omega_d t) + A_2 \sin(\omega_d t)] \quad (\text{A.2.24})$$

Now x can be expressed in another format, with the relationships:

$$A = \sqrt{A_1^2 + A_2^2}, \quad (\text{A.2.25})$$

$$\phi = \arctan\left(\frac{A_1}{A_2}\right), \quad (\text{A.2.26})$$

and

$$x(t) = Ae^{-\zeta\omega_n t} \sin(\omega_d t + \phi) \quad (\text{A.2.27})$$

with A and ϕ determined by the initial conditions.

A.2.2 Critically Damped Motion in Free Vibration ($\zeta = 1$)

In this special case, where the system is critically damped, the roots are equal, so

$$\lambda_1 = \lambda_2 = \omega_n \quad (\text{A.2.28})$$

and the solution to Equation A.2.3 is of the form

$$x(t) = (a_1 + a_2 t) e^{-\omega_n t}, \quad (\text{A.2.29})$$

with a_1 and a_2 subject to initial conditions.

A.2.3 Over Damped Motion in Free Vibration ($\zeta > 1$)

In the over damped case, the roots from the auxiliary equation, Equation A.2.8, are real and expressed as

$$\lambda_1 = -\zeta\omega_n - \omega_n\sqrt{\zeta^2 - 1} \quad (\text{A.2.30})$$

and

$$\lambda_2 = -\zeta\omega_n + \omega_n\sqrt{\zeta^2 - 1}. \quad (\text{A.2.31})$$

The solution to Equation A.2.3, then becomes

$$x(t) = e^{-\zeta\omega_n t} \left(a_1 e^{-\omega_n t \sqrt{\zeta^2 - 1}} + a_2 e^{\omega_n t \sqrt{\zeta^2 - 1}} \right), \quad (\text{A.2.32})$$

with a_1 and a_2 determined by the initial conditions.

A.3 Principals of Undamped Motion in Forced Vibration

Consider now, a system where a spring-mass system once again has negligible dampening but a harmonic excitation is applied. If the harmonic excitation is represented by the cosine

function, i.e.

$$F(t) = F_0 \cos(\omega t), \quad (\text{A.3.1})$$

the application of Newton's second law finds

$$m\ddot{x}(t) + kx(t) = F_0 \cos(\omega t). \quad (\text{A.3.2})$$

Dividing by the mass and applying the definition of ω_n from Equation A.1.10 yields

$$\ddot{x}(t) + \omega_n^2 x(t) = f_0 \cos(\omega t), \quad (\text{A.3.3})$$

where f_0 is simply $\frac{F_0}{m}$. It is noted that this is a linear, non-homogeneous differential equation where the solution is the sum of a particular solution, x_p and the general- or complimentary solution, x_c [43], that is

$$x(t) = x_p(t) + x_c(t). \quad (\text{A.3.4})$$

To find the particular solution, using the method of undetermined coefficients, it is assumed that form of the particular solution, x_p , is the same as that of the harmonic excitation, Equation A.3.1, such that

$$x_p(t) = X \cos(\omega t) \quad (\text{A.3.5})$$

and thereby

$$\ddot{x}_p(t) = -\omega^2 X \cos(\omega t). \quad (\text{A.3.6})$$

Substitution this into Equation A.3.3, yields

$$-\omega^2 X \cos(\omega t) + \omega_n^2 X \cos(\omega t) = f_0 \cos(\omega t). \quad (\text{A.3.7})$$

Upon rearrangement, this becomes

$$\left(\omega_n^2 X - \omega^2 X - f_0\right) \cos(\omega t) = 0. \quad (\text{A.3.8})$$

Since $\cos(\omega t)$ cannot be equal to zero for all of the defined time ($t > 0$), it is the $(\omega_n^2 X - \omega^2 X - f_0)$ component that must be zero, which solves X as

$$X = \frac{f_0}{\omega_n^2 - \omega^2}. \quad (\text{A.3.9})$$

The particular solution to A.3.3, is therefore

$$x_p(t) = \frac{f_0}{\omega_n^2 - \omega^2} \cos(\omega t). \quad (\text{A.3.10})$$

Where it can clearly be seen that the amplitude of the oscillation becomes excessively large as the excitation frequency, ω , approaches the natural frequency, ω_n to an undefined point where they are equal to each other.

The general- or complimentary solution, x_c from Equation A.1.4 and A.1.10 is

$$x_c(t) = A \sin(\omega_n t + \phi). \quad (\text{A.3.11})$$

With the relationships expressed in Equations A.2.25 and A.2.26, Equation A.3.11 can be expressed in the form

$$x_c(t) = A_1 \cos(\omega_n t) + A_2 \sin(\omega_n t). \quad (\text{A.3.12})$$

If Equations A.3.10 and A.3.12 are implemented in Equation A.3.4,

$$x(t) = \frac{f_0}{\omega_n^2 - \omega^2} \cos(\omega t) + A_1 \cos(\omega_n t) + A_2 \sin(\omega_n t). \quad (\text{A.3.13})$$

If the initial position and velocity is expressed as constants x_0 and v_0 ,

$$x(0) = \frac{f_0}{\omega_n^2 - \omega^2} + A_1 = x_0 \quad (\text{A.3.14})$$

$$\Rightarrow A_1 = x_0 - \frac{f_0}{\omega_n^2 - \omega^2} \quad (\text{A.3.15})$$

$$\dot{x}(0) = A_2 \omega_n = v_0 \quad (\text{A.3.16})$$

$$\Rightarrow A_2 = \frac{v_0}{\omega_n} \quad (\text{A.3.17})$$

and Equation A.3.13 becomes

$$x(t) = \frac{f_0}{\omega_n^2 - \omega^2} \cos(\omega t) + \left(x_0 - \frac{f_0}{\omega_n^2 - \omega^2} \right) \cos(\omega_n t) + \frac{v_0}{\omega_n} \sin(\omega_n t) \quad (\text{A.3.18})$$

A.4 Principals of Damped Motion in Forced Vibration

The first step in solving the damped motion problem, is to express it in the general form,

$$m\ddot{x}(t) + c\dot{x}(t) + kx(t) = F_0 \cos(\omega t). \quad (\text{A.4.1})$$

Then, to divide by the mass and apply the definitions for ω_n , ζ and f_0 to deliver

$$\ddot{x}(t) + 2\zeta\omega_n\dot{x}(t) + \omega_n^2x(t) = f_0 \cos(\omega t). \quad (\text{A.4.2})$$

As with the undamped case, a particular and a complimentary solution needs to be found. The format of the particular solution is assumed to be the same as that of the forcing function, with an expected phase shift, θ , as a result of the damping, i.e.

$$x_p(t) = X \cos(\omega t - \theta), \quad (\text{A.4.3})$$

or in the format

$$x_p(t) = B_1 \cos(\omega t) + B_2 \sin(\omega t). \quad (\text{A.4.4})$$

Similar to that of Equation A.3.12. The next step is to derive $\dot{x}_p(t)$ and $\ddot{x}_p(t)$ to yield

$$\dot{x}_p(t) = -\omega B_1 \sin(\omega t) + \omega B_2 \cos(\omega t) \quad (\text{A.4.5})$$

and

$$\ddot{x}_p(t) = -\omega^2 B_1 \cos(\omega t) - \omega^2 B_2 \sin(\omega t). \quad (\text{A.4.6})$$

If these equations are then implemented into Equation A.4.2, it becomes

$$\begin{aligned} & -\omega^2 B_1 \cos(\omega t) - \omega^2 B_2 \sin(\omega t) - 2\zeta\omega_n\omega B_1 \sin(\omega t) + 2\zeta\omega_n\omega B_2 \cos(\omega t) \\ & + \omega_n^2 B_1 \cos(\omega t) + \omega_n^2 B_2 \sin(\omega t) - f_0 \cos(\omega t) = 0. \end{aligned} \quad (\text{A.4.7})$$

$$\begin{aligned} \Rightarrow & \left(\omega_n^2 B_2 - 2\zeta\omega_n\omega B_1 - \omega^2 B_2 \right) \sin(\omega t) \\ & + \left(\omega_n^2 B_1 + 2\zeta\omega_n\omega B_2 - \omega^2 B_1 - f_0 \right) \cos(\omega t) = 0 \end{aligned} \quad (\text{A.4.8})$$

This equation is defined for all $t > 0$, so the components of $\sin(\omega t)$ and $\cos(\omega t)$ cannot ensure that the sum equates zero, it is both the $(\omega_n^2 B_2 - 2\zeta\omega_n\omega B_1 - \omega^2 B_2)$ and the $(\omega_n^2 B_1 + 2\zeta\omega_n\omega B_2 - \omega^2 B_1 - f_0)$ terms that must equal zero simultaneously in-order to satisfy Equation A.4.8. Therefore,

$$\omega_n^2 B_2 - 2\zeta\omega_n\omega B_1 - \omega^2 B_2 = 0 \quad (\text{A.4.9})$$

$$\Rightarrow B_1 (-2\zeta\omega_n\omega) + B_2 (\omega_n^2 - \omega^2) = 0 \quad (\text{A.4.10})$$

and

$$\omega_n^2 B_1 + 2\zeta\omega_n\omega B_2 - \omega^2 B_1 - f_0 = 0 \quad (\text{A.4.11})$$

$$\Rightarrow B_1 (\omega_n^2 - \omega^2) + B_2 (2\zeta\omega_n\omega) = f_0. \quad (\text{A.4.12})$$

Alternatively, this can be expressed in the matrix format as

$$\begin{bmatrix} -2\zeta\omega_n\omega & \omega_n^2 - \omega^2 \\ \omega_n^2 - \omega^2 & 2\zeta\omega_n\omega \end{bmatrix} \begin{bmatrix} B_1 \\ B_2 \end{bmatrix} = \begin{bmatrix} 0 \\ f_0 \end{bmatrix}. \quad (\text{A.4.13})$$

From matrix algebra [43], it is known that (subject to a non-zero determinant) and therefore

$$\begin{bmatrix} B_1 \\ B_2 \end{bmatrix} = \begin{bmatrix} -2\zeta\omega_n\omega & \omega_n^2 - \omega^2 \\ \omega_n^2 - \omega^2 & 2\zeta\omega_n\omega \end{bmatrix}^{-1} \begin{bmatrix} 0 \\ f_0 \end{bmatrix}. \quad (\text{A.4.14})$$

Hence, the inverse

$$\begin{bmatrix} -2\zeta\omega_n\omega & \omega_n^2 - \omega^2 \\ \omega_n^2 - \omega^2 & 2\zeta\omega_n\omega \end{bmatrix}^{-1} = \frac{1}{-4\zeta^2\omega_n^2\omega^2 - (\omega_n^2 - \omega^2)^2} \begin{bmatrix} 2\zeta\omega_n\omega & \omega^2 - \omega_n^2 \\ \omega^2 - \omega_n^2 & -2\zeta\omega_n\omega \end{bmatrix} \quad (\text{A.4.15})$$

substituted into Equation A.4.14, simplifies to

$$B_1 = \frac{f_0 (\omega_n^2 - \omega^2)}{(2\zeta\omega_n\omega)^2 + (\omega_n^2 - \omega^2)^2} \quad (\text{A.4.16})$$

and

$$B_2 = \frac{2f_0\zeta\omega_n\omega}{(2\zeta\omega_n\omega)^2 + (\omega_n^2 - \omega^2)^2}. \quad (\text{A.4.17})$$

Which, when substituted into Equation A.4.4 and simplified, yields the particular solution,

$$x_p(t) = \frac{f_0}{(2\zeta\omega_n\omega)^2 + (\omega_n^2 - \omega^2)^2} \left[(\omega_n^2 - \omega^2) \cos(\omega t) + 2\zeta\omega_n\omega \sin(\omega t) \right]. \quad (\text{A.4.18})$$

It is known from the response of the free vibration case, that the complimentary function is dependent on the dampening ratio, ζ . Three cases exist that yield three possible answers

to x : under damped, ($0 < \zeta < 1$),

$$x(t) = \frac{f_0}{(2\zeta\omega_n\omega)^2 + (\omega_n^2 - \omega^2)^2} \left[(\omega_n^2 - \omega^2) \cos(\omega t) + 2\zeta\omega_n\omega \sin(\omega t) \right] + e^{-\zeta\omega_n t} [A_1 \cos(\omega_d t) + A_2 \sin(\omega_d t)] \quad (\text{A.4.19})$$

critically damped, ($\zeta = 1$),

$$x(t) = \frac{f_0}{(2\zeta\omega_n\omega)^2 + (\omega_n^2 - \omega^2)^2} \left[(\omega_n^2 - \omega^2) \cos(\omega t) + 2\zeta\omega_n\omega \sin(\omega t) \right] + (a_1 + a_2 t) e^{-\omega_n t} \quad (\text{A.4.20})$$

and over damped, ($\zeta > 1$),

$$x(t) = \frac{f_0}{(2\zeta\omega_n\omega)^2 + (\omega_n^2 - \omega^2)^2} \left[(\omega_n^2 - \omega^2) \cos(\omega t) + 2\zeta\omega_n\omega \sin(\omega t) \right] + e^{-\zeta\omega_n t} \left(a_1 e^{-\omega_n t \sqrt{\zeta^2 - 1}} + a_2 e^{\omega_n t \sqrt{\zeta^2 - 1}} \right). \quad (\text{A.4.21})$$

It is observed that with increasing time, x , approaches the particular solution, x_p . Because of this, the first term (the particular solution) of Equations A.4.19, A.4.20 and A.4.21, is called the steady state solution and x_c , the second term (the complimentary solution) is called the transient solution. The transient solution may become inconsequential very quickly and can often be ignored completely. This is, however not always the case so it has to be considered especially were active control is implemented on the system.

If r , the frequency ratio is expressed as

$$r = \frac{\omega}{\omega_n} \quad (\text{A.4.22})$$

and the normalised amplitude of oscillation is calculated as

$$\frac{Xk}{F_0} = \frac{1}{\sqrt{(1 - r^2)^2 + (2\zeta r)^2}} \quad (\text{A.4.23})$$

A dynamic response curve can be plotted and is shown in Figure A.1. This dynamic response shows the normalised amplitude with regards to the frequency ratio for different values of ζ .

From this figure, the effects of damping on the oscillation amplitude for a forced vibra-

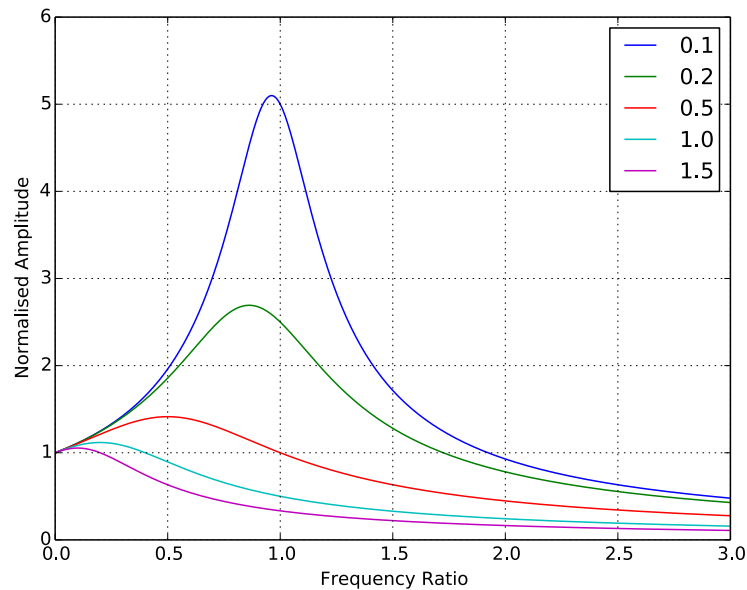


Figure A.1: Dynamic response curve showing plots for varying values of ζ .

tion problem can clearly be seen. If this system were to operate at a natural frequency resonance ($r = 1$), the amplitude of oscillation can be well controlled by varying the damping coefficient.

A.5 Free Piston Stirling Engine Dynamics

This analysis has only considered a simple, single degree-of-freedom problem. The dynamics of a free-piston Stirling engine, however are more complex.

The development of the linear dynamics of a free-piston Stirling engine is a formidable task that requires intricate knowledge of thermodynamics. As such it falls beyond the scope of this project. The principals developed in this Appendix apply to the free-piston Stirling engine dynamics, only in a more complicated manner.

What this Appendix does illustrate however, is the advantage of choosing a single-phase design with the current driven in phase with the electromotive force. In doing so, the damping coefficient can be changed and oscillation amplitude can be controlled

The nature of the mechanical input power is also illustrated in the mathematical development of the Appendix. Generally, electrical machines rotate. The nature of mechanical energy in rotation is very simple. When designing a linear oscillating machine, the complex dynamics of linear motion needs to be understood. That is the main reason for the analysis in this Appendix.

Appendix B

Loss Discrepancy Investigation

While evaluating the results of optimisation, it was found that there was a difference between the analytically calculated copper losses and the copper losses provided by the simulation software. The reason for this difference is investigated here. Firstly, the analytically loss calculations need to be described.

The mean conductor length, l_{Cu}

$$l_{Cu} = 2C_w + 2C_l + \pi C_t \quad (\text{B.0.1})$$

in a single coil is calculated using the geometry of the coil, where C_l , C_w and C_t are shown in Figure B.1.

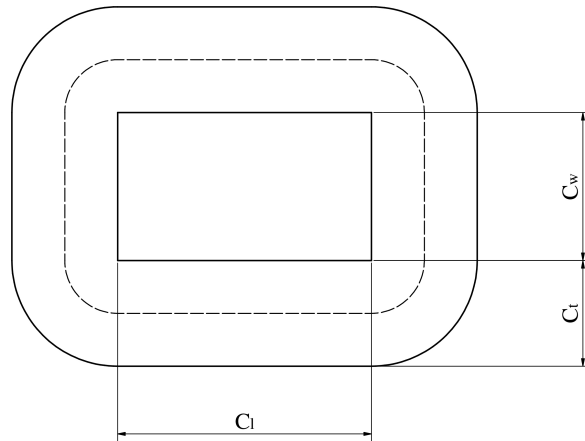


Figure B.1: Dimensions of a coil used to calculate the mean conductor length.

The combined resistance of all the coils,

$$R = \frac{n_{coils} \rho_{Cu} l_{Cu}}{k_{fill} A_{Cu}} \quad (\text{B.0.2})$$

is calculated using the number of coils, n_{coils} , the copper resistivity, ρ_{Cu} and a fill factor, k_{fill} .

The cross sectional area of the coil,

$$A_{Cu} = C_t C_h \quad (\text{B.0.3})$$

is the product of the coil height, C_h , defined from the geometry and the coil thickness, C_t shown in Figure B.1.

The copper losses, P_{loss} , are then calculated as

$$P_{loss_A} = I_{RMS}^2 R \quad (\text{B.0.4})$$

The copper losses obtained from the simulation software was calculated from the loss curve of *MagNet*[®] using the same curve fit and numerical integration technique described in Section 3.3.4 while taking a fill factor into account. That is

$$P_{loss_S} = \frac{1}{k_{fill} T} \int_0^T p_{loss} dt. \quad (\text{B.0.5})$$

These two loss values, the analytically calculated P_{loss_A} and the simulated P_{loss_S} , were not equal to each other. An investigation is now documented that attempts to establish why this is.

Repeatability

A number of different geometric configurations and design layouts were simulated along with the analytical loss calculations. In every instance investigated, the analytically calculated losses were conservative in relation to the simulated losses by exactly the same factor. That is

$$P_{loss_A} = 0,791 P_{loss_S} \quad (\text{B.0.6})$$

for every instance. This indicated that discrepancy is constant and not variable.

Current

As copper losses are a function of the current and the resistance in a coil, the current was the next aspect to be investigated.

An error could manifest in the calculations here due to the fact that the analytical calculations use a root mean square value for the current in the calculations.

A variable in optimisation is the current amplitude. It was investigated if the amplitude was not accidentally used in these calculations instead of the root mean square. This was not

the case. If it had been the case, the analytically calculated losses would have been greater than the simulated losses.

The root mean square of the sinusoidally driven current, I_{RMS} was calculated from the current amplitude I , as

$$I_{RMS} = \frac{I}{\sqrt{2}}. \quad (\text{B.0.7})$$

Constants

It stands to reason that if there is a constant discrepancy between two calculations, a constant factor might be the cause for this discrepancy. In the analytically calculated resistance, the constants are the fill factor, k_{fill} , the copper resistivity, ρ_{Cu} , and the number of coils, n_{coils} .

The constants used in simulation and the constants used in the analytical calculations were investigated to reveal that all these constants are the same for both. The number of coils, n_{coils} was consistently communicated, a fill factor, k_{fill} of 0,5 was consistently communicated and the copper resistivity, ρ_{Cu} , defined in the analytical calculations was taken directly from the value used in simulation. *MagNet*[®] defines the material to have a resistivity of 0,17241 $n\Omega m$.

Mean Conductor Length

The mean conductor length, l_{Cu} calculation was checked. This calculation is shown in Equation B.0.1. It is considered to be accurate.

Equal Current Distribution

Now that many of the regular culprits in miscalculation have been eliminated as the cause for discrepancy, the investigation moves on to look at less obvious aspects.

In simulation, a single turn equivalent model is used. The coil is therefore simulated as a solid copper volume. The effects of a multitude of turns can, however, be accounted for. In order to determine that this has been defined correctly, the current density in the coil can be plotted on a cross-section of the coil. This was done and an equal distribution of the current density was observed. Additionally, a fill-factor was accounted for as can be observed in Equation B.0.5.

Thermal Influences

Losses manifest in the form of heat. As a conductor is heated, the resistance of the conductor increases, generating higher losses. If the simulation software takes this into account, it

could easily account for the discrepancies between the simulated losses and the analytically calculated losses.

This appears not to be the case. The discrepancy was constant with varying geometry. With varying geometry the surface area of the coil changes, changing the thermal properties of the coil. A larger surface area facilitates better heat exchange which would reduce the temperature of the conductor which in turn reduces losses. Some coil geometries would therefore be less effected by this factor than others.

It is possible that *MagNet*[®] simply accounts for this with a constant. This is unlikely and there is nothing that suggests it in the *MagNet*[®] *help* files.

Transient Losses

The possibility exists that *MagNet*[®] accounts for eddy current losses resulting from magnetic fields where the magnets are in motion close the coils.

To determine if this is the cause for the discrepancy, a no-load simulation can be performed on a transient simulation to observe if any losses are induced in the coils. Such a simulation was performed but the results showed no such losses.

Coil Resistance

MagNet[®] must at some stage calculate the resistance of the coil in order to calculate the copper losses. This resistance value is never given. There is no available literature in the *MagNet*[®] *help* files that shows how the resistance of the coil is calculated.

Without this information, it cannot be determined if there is a discrepancy between the analytically calculated coil resistance and the simulated coil resistance. At this stage in the investigation, it is becoming increasingly more likely that the discrepancy is indeed between these two values.

This brings an important question to light. If there is indeed a discrepancy between the two coil resistance values, which of the two is more representative of reality? The quick and obvious answer to that question must be that *MagNet*[®] calculates the resistance in a more representative manner than the author.

One other factor needs to be considered, however. Three dimensional finite element software is extremely complicated. It has already been established in Section 3.3.4 that *MagNet*[®] uses a forwards difference method to derive the output voltage which caused an erroneous phase shift in this specific application of the software. This method of deriving the voltage is presumably used because it is a robust method.

The analytical coil resistance equations were specifically created for this particular application. It is not inconceivable that *MagNet*[®] uses a different method that is applicable to

a very wide range of applications which could cause an error similar in nature to the one shown in Section 3.3.4.

Arguably, *MagNet*[®] could also add coefficients to the resistance calculations that account for impurities in typical production copper wire or some sort of temperature constant. These coefficients could be implemented specifically to obtain a more representative coil resistance value than typical analytical calculations could yield.

Without direct access to the information on how the coil resistance is calculated in simulation, however, further progress on this investigation is impossible.

Conclusion

In an attempt to gain further insight, static simulations and transient simulations were directly compared. In this comparison, the copper losses from both simulations were identical.

Recall that the reason why the losses were calculated analytically instead of simply using the losses from *MagNet*[®] was to simplify the optimisation process. In this way the only optimisation constraint becomes the output power and the driven current becomes a dependent variable. This is explained in Section 3.3.4. The advantage gained in reducing optimisation time in this way is significant, especially considering that an estimated 600 days were spent in active optimisation (disregarding debugging time).

The discrepancy between calculated and simulated losses could have been realised at a much earlier stage in the project, had the analytically calculated losses been compared to the simulated losses of the static simulations. Regrettably, the discrepancy was only realised after performing the transient analysis.

A decision had to be made on how to proceed. There were three options.

The first was to repeat all the optimisations up to this point, redefining the optimisation problem with an additional parameter, the driven current, and an additional constraint, the efficiency.

The second was to repeat all the optimisations using the same structure but by scaling the analytically calculated losses by a constant factor to match the losses simulated by *MagNet*[®].

The third option was to ignore the discrepancy and proceed with the project, focusing on the design aspects of the machine. This was the option that was eventually chosen.

This choice was made on the basis of two arguments.

Firstly, because the discrepancy between the analytically calculated losses and the simulated losses are constant for every evaluation in every design, the comparative study retains its validity.

Secondly, it was always envisioned to perform a transient optimisation on a design. In the transient optimisation, the energy balance of *MagNet*[®] has to be used. The losses are

therefore taken from the simulation and not calculated. This design would then be constructed and tested. Any errors in loss calculations at this stage of the project would therefore have no effect on the final prototype and envisioned test results.

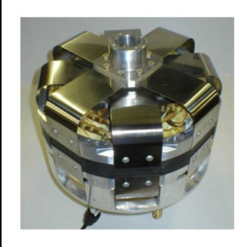
Focus was therefore directed to finding a better design for the prototype rather than repeating old work that would invariably have led to exactly the same deductions, wasting many months that could otherwise be better utilised.

Appendix C

Commercial Machine Data sheet

The data sheet of the commercial machine from *Q-drives* is shown in this Appendix.

STAR Motors/Alternators - 1S297M/A



Product Description
The 1S297M/A is a 5 kWe motor/alternator, providing 26 mm of operational stroke.

General Specifications

Rated Power (W@60Hz)	: 5000
Stroke (mm p-p)	: 25
Volts / Current (max)	: 240/28
Diameter (mm)	: 297
Length	: 130 mm
Moving Mass	: 9.4 kg
Overall Mass	: 27.5 kg
Stroke Limit	: 26 mm
Damping, Rm	: 62 N-s/m
Intrinsic Stiffness	: 169 kN/m
Rated Operating Voltage	: 208 VAC 1Ø
Rated Operating Current	: 28 amps
Input Power Maximum (60Hz; 26mm stroke)	: 5 kWe
AC Frequency	: 60 Hz
Core Impedance	: 0.4 ohms DC
Stator Inductance	: 18 mH
Stator Resistance	: 0.5 ohm @60Hz
Nominal BL Product	: 53 N/amp

info@qdrive.com

Qdrive/Chart Industries, 302 10th St., Troy, NY 12180 | Phone: 1-518-272-3565

Figure C.1: 5 kW *Q-drives* linear electric machine.

Appendix D

Prototype Schematics

The schematics of the prototype and test bed of the final design is given in this Appendix.

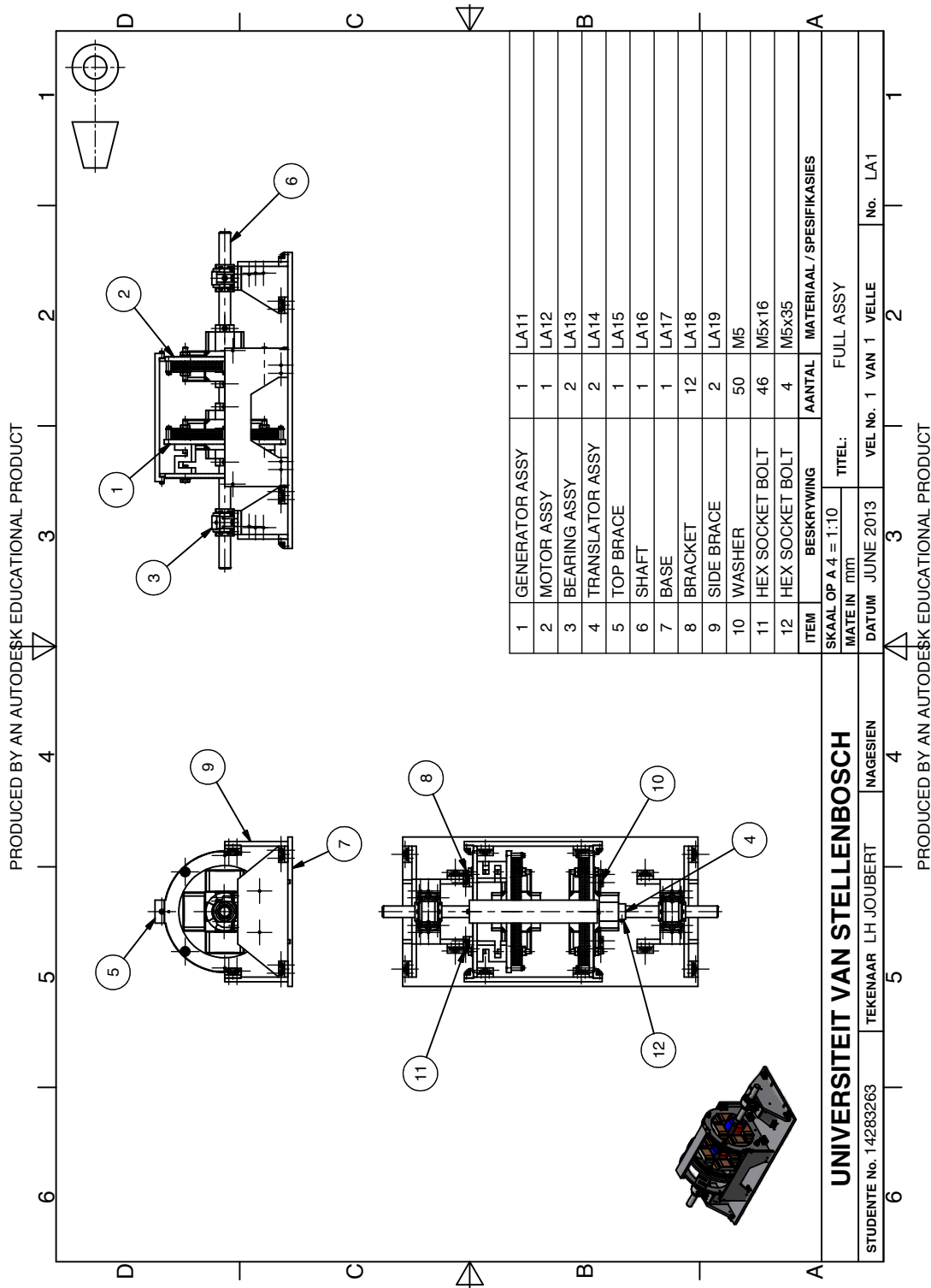


Figure D.1: Full Assembly

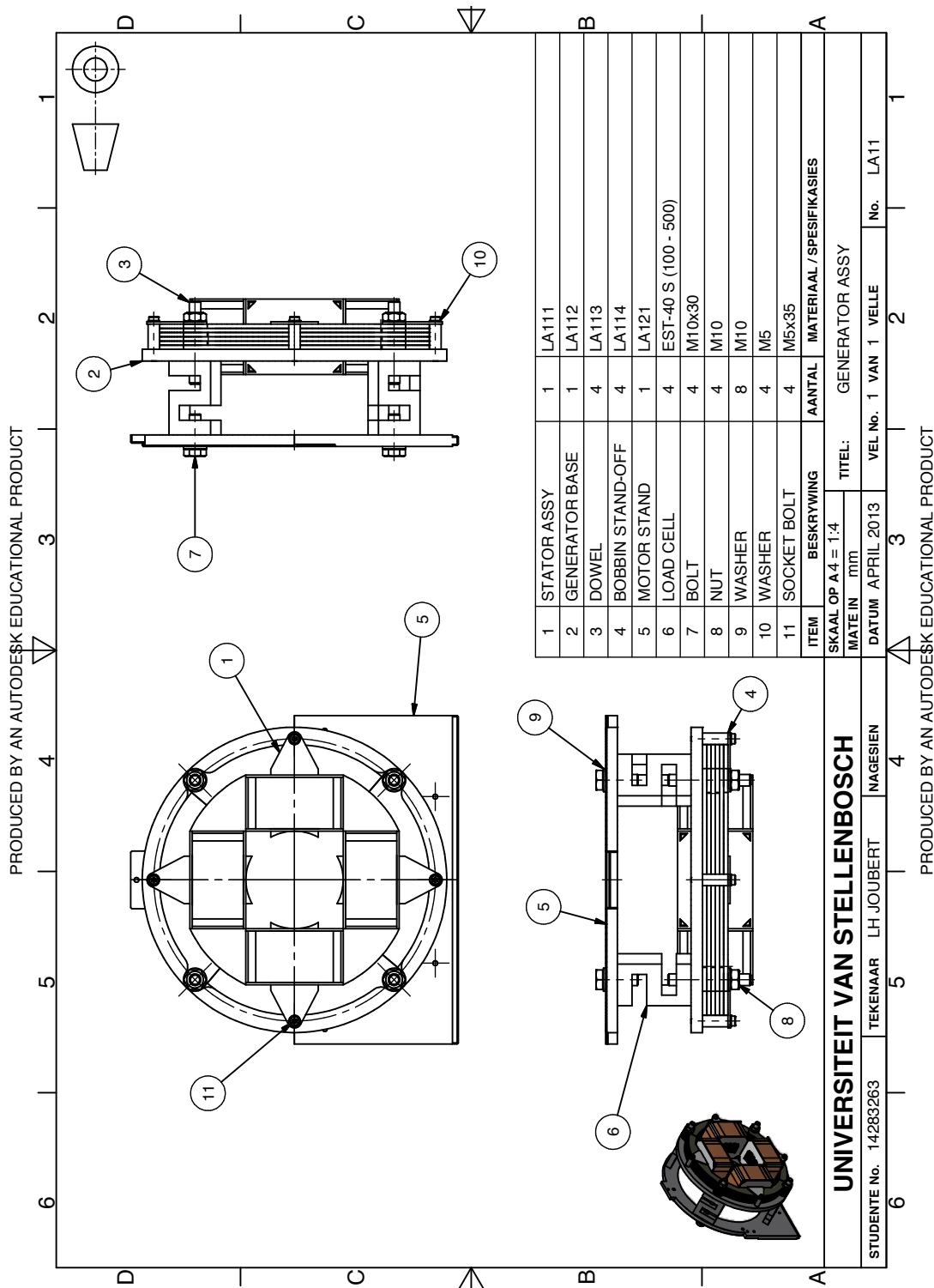


Figure D.2: Generator Assembly

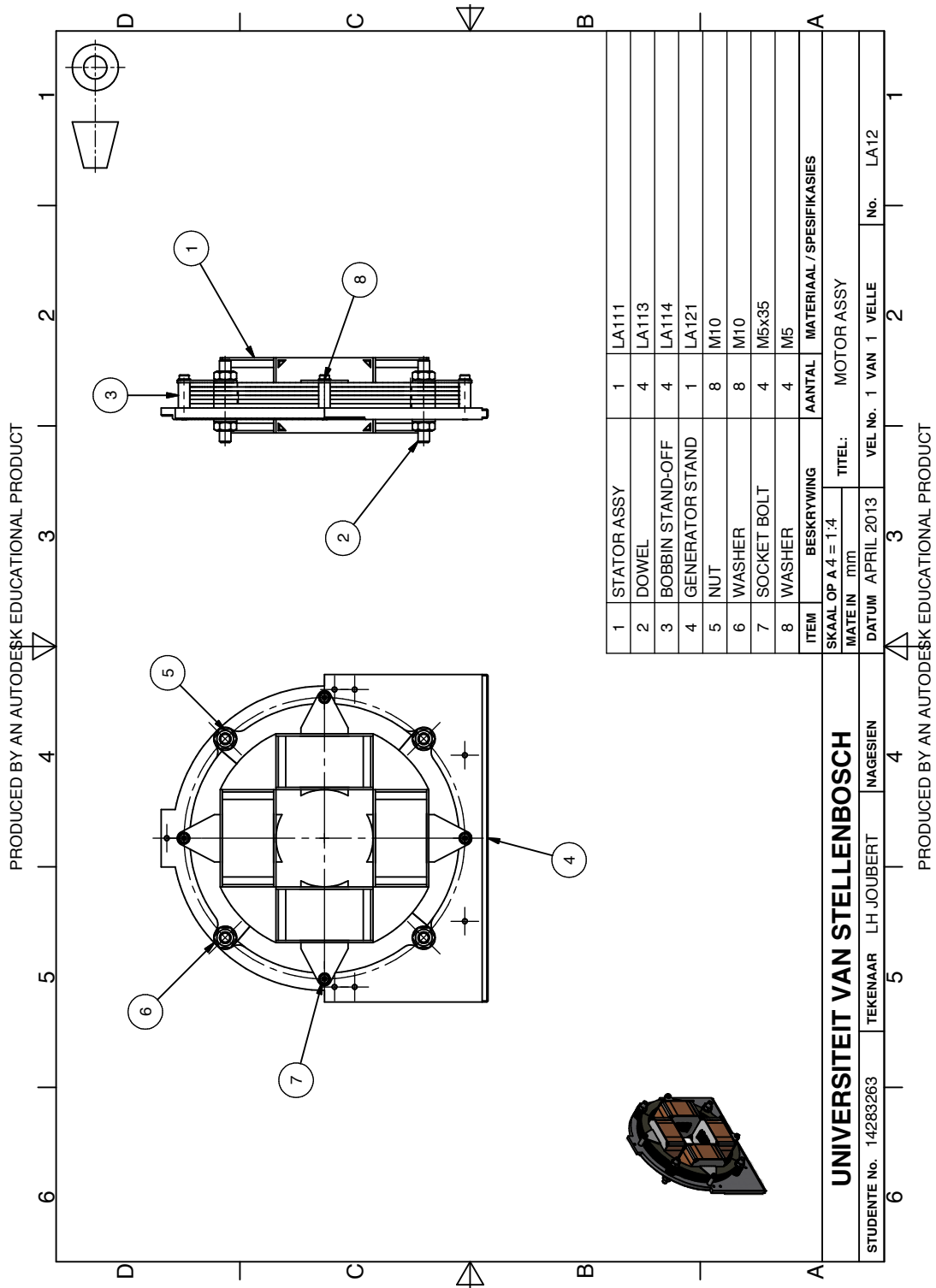


Figure D.3: Motor Assembly

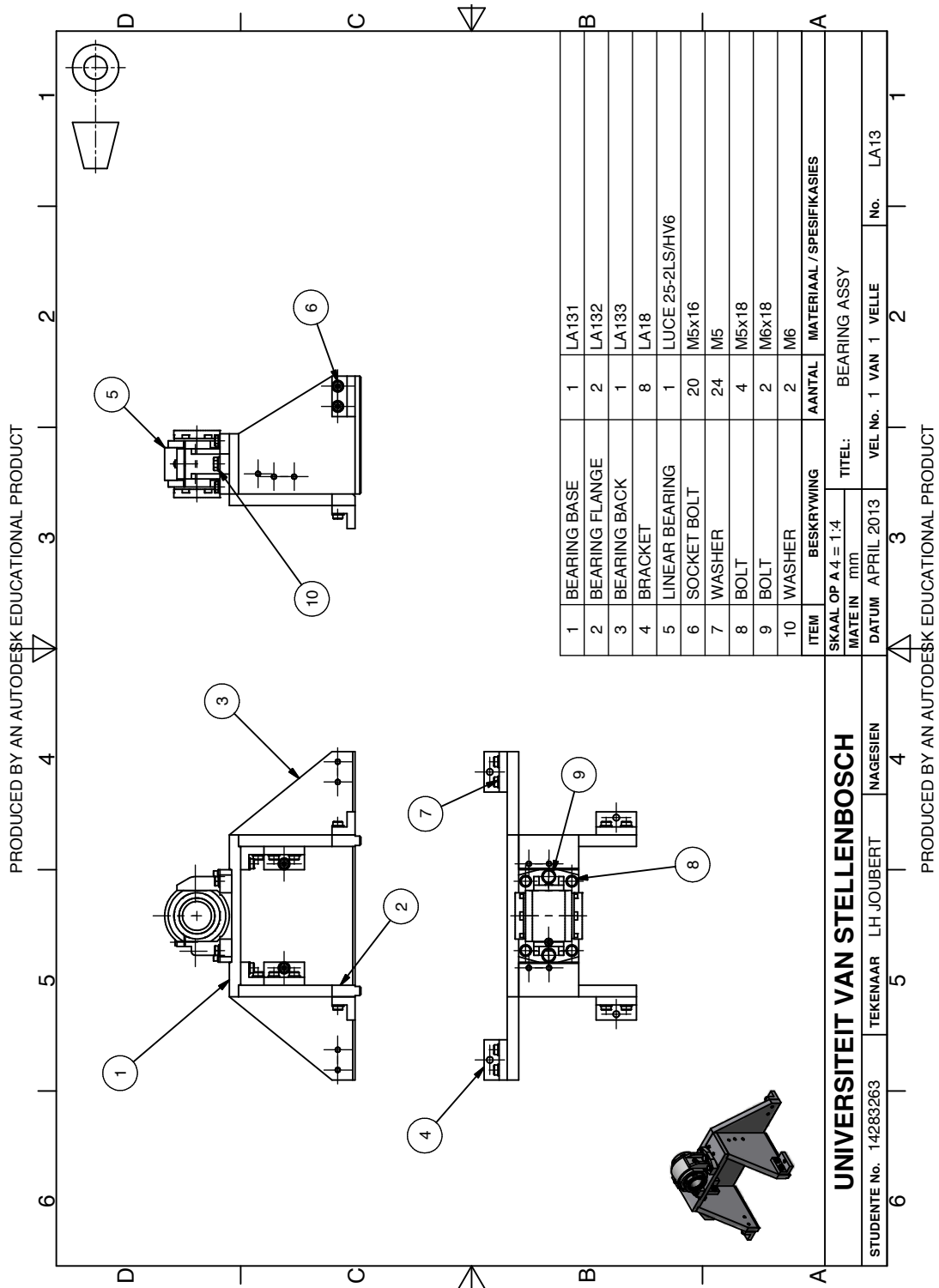


Figure D.4: Bearing Assembly

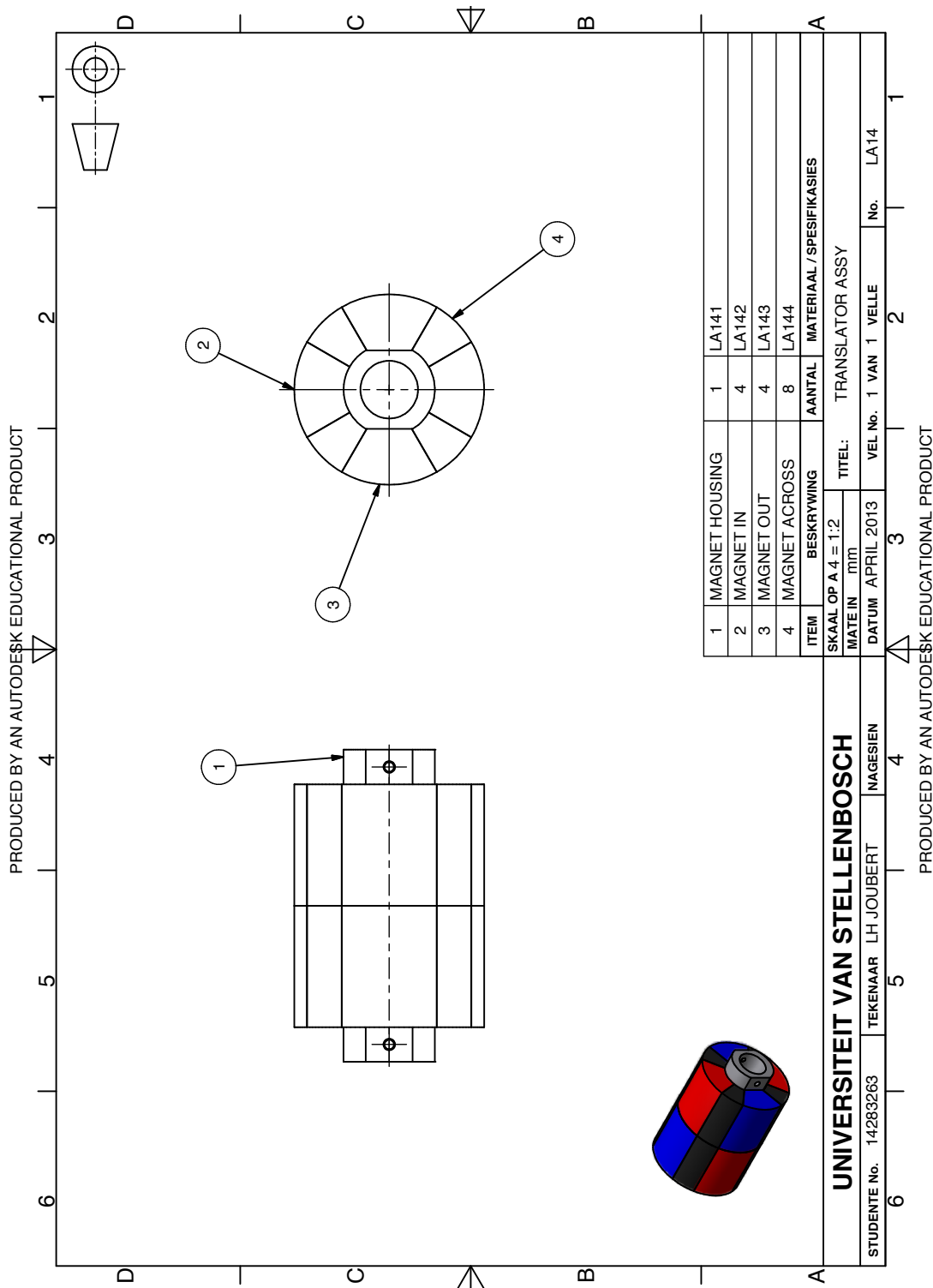


Figure D.5: Translator Assembly

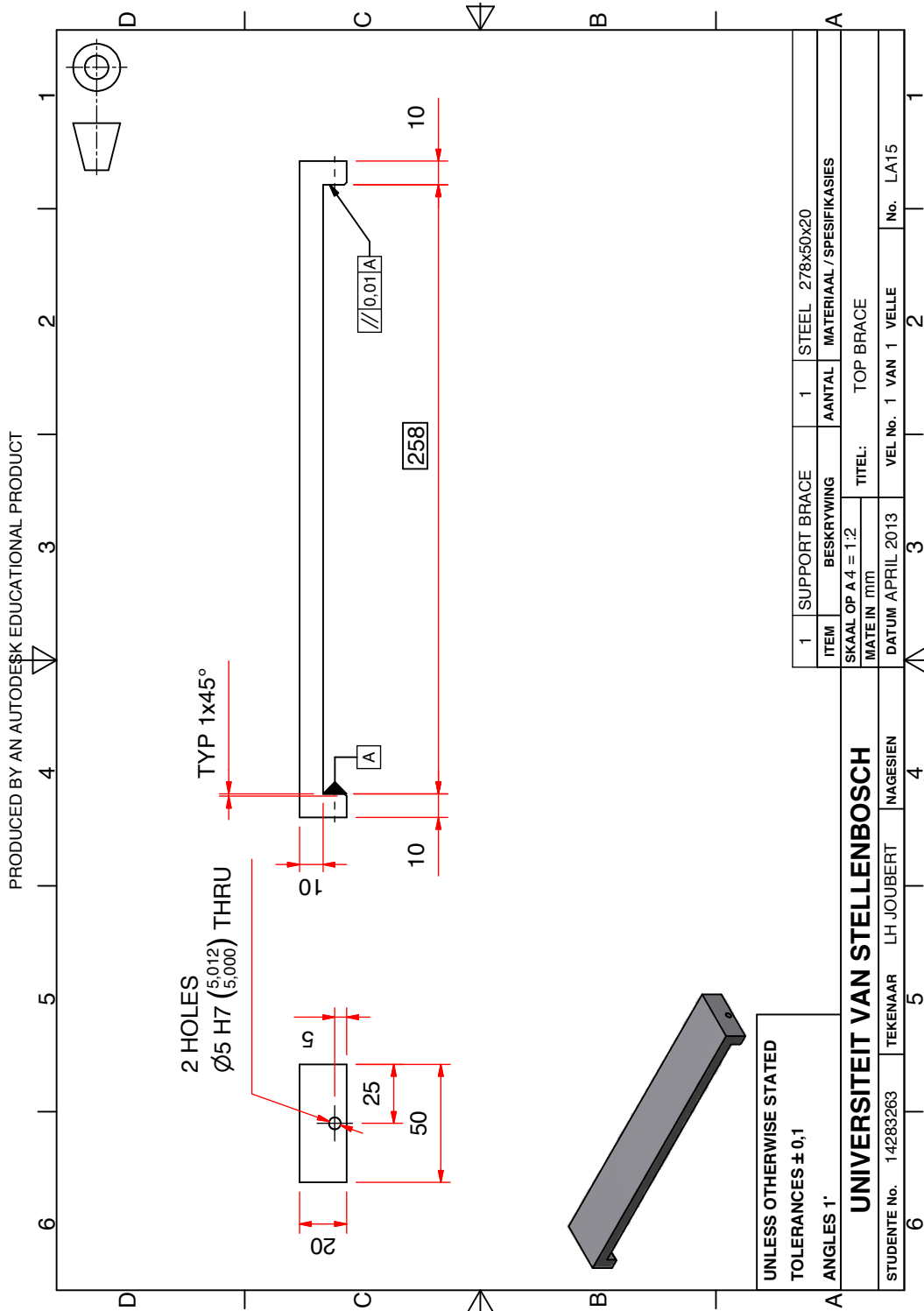


Figure D.6: Top Brace

PRODUCED BY AN AUTODESK EDUCATIONAL PRODUCT

PRODUCED BY AN AUTODESK EDUCATIONAL PRODUCT

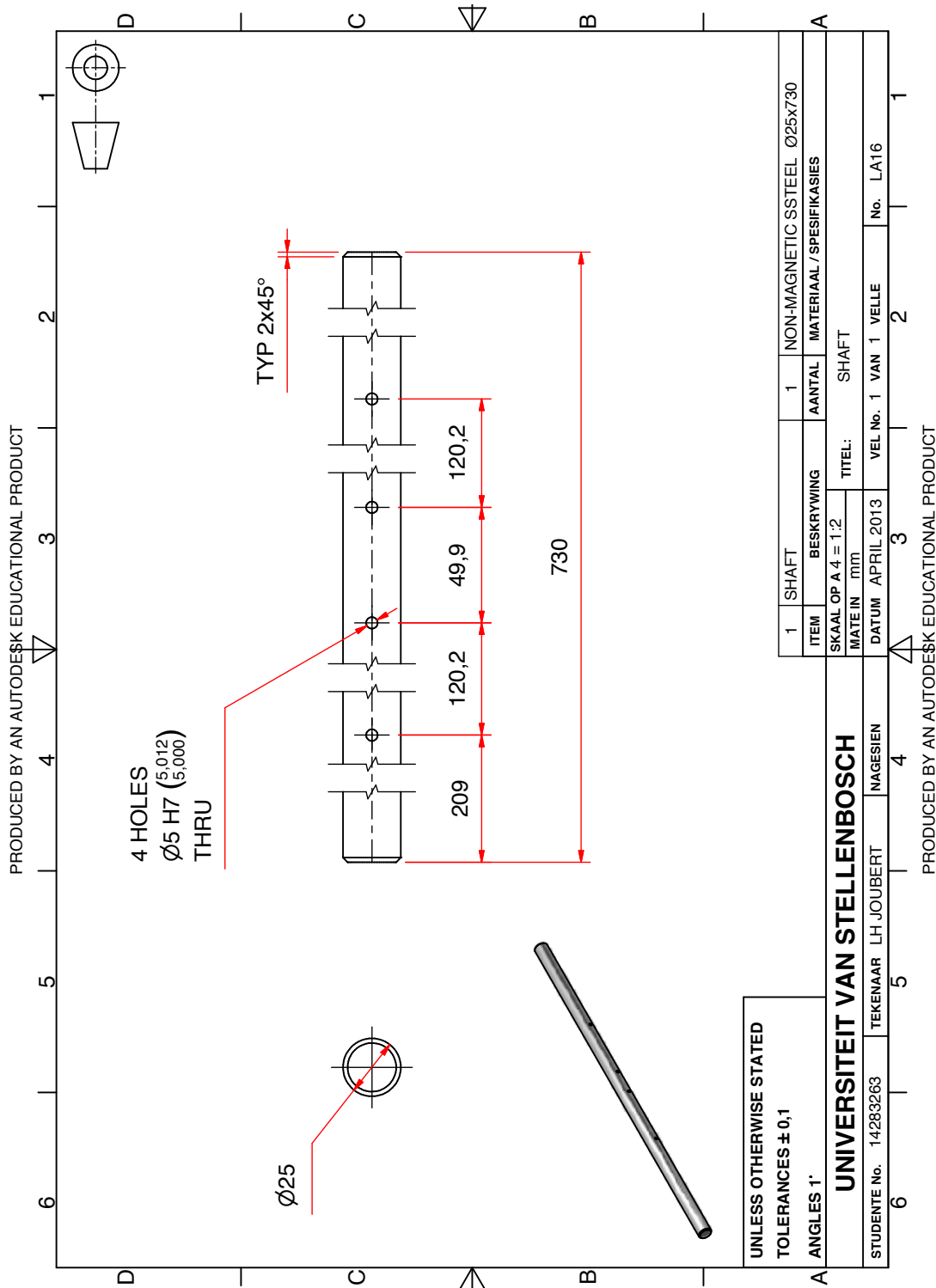


Figure D.7: Shaft

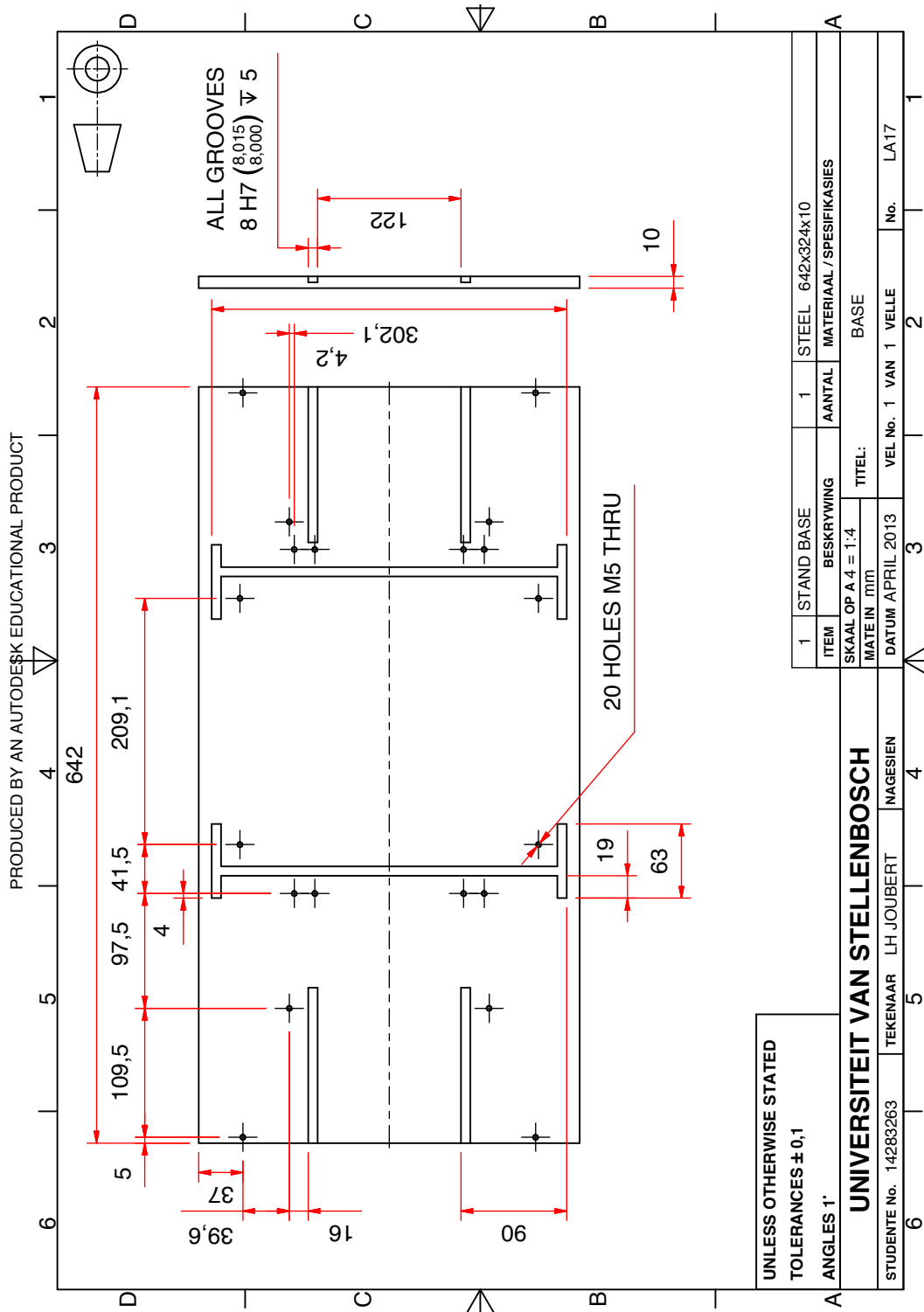


Figure D.8: Base

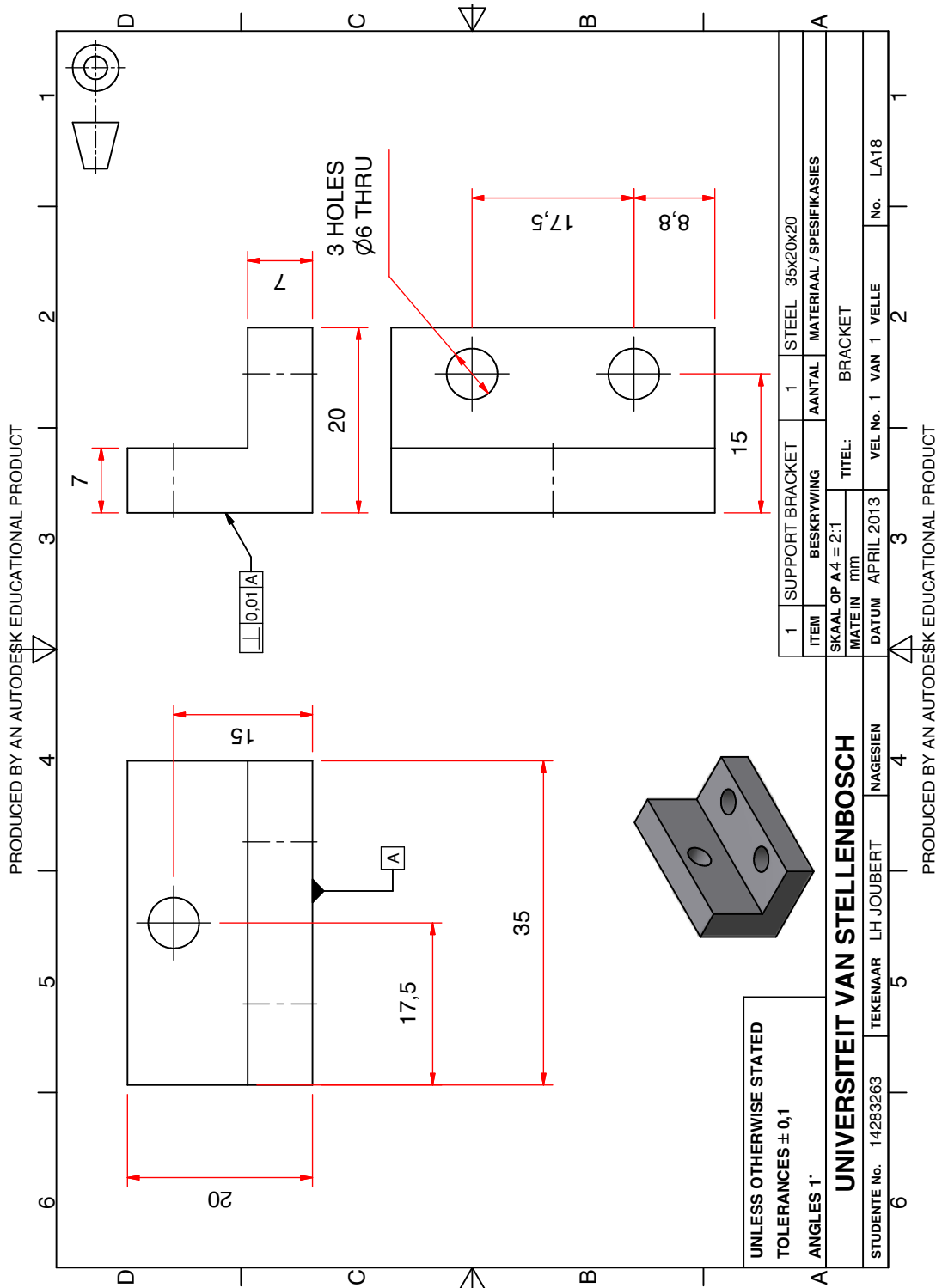


Figure D.9: Bracket

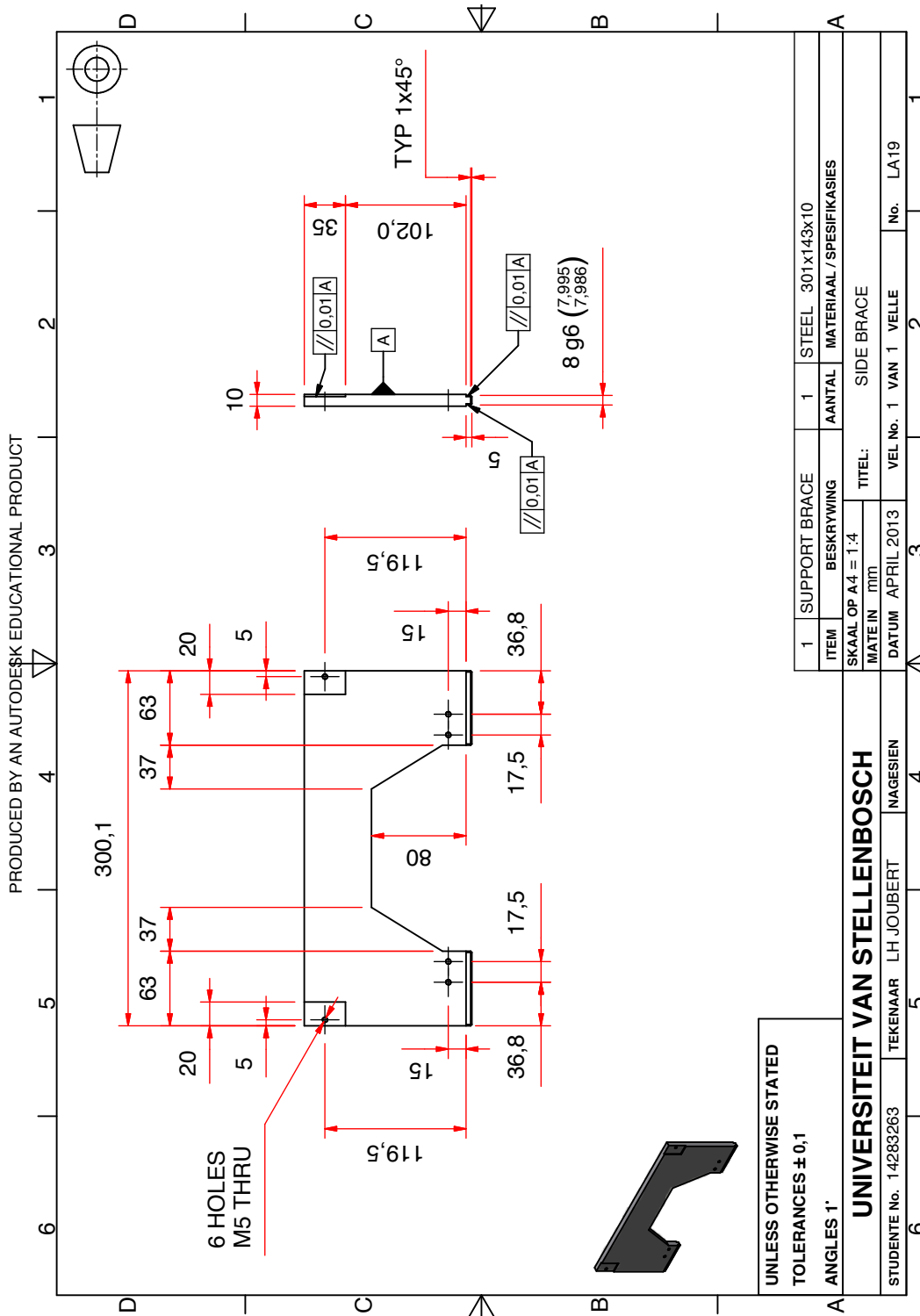


Figure D.10: Side Brace

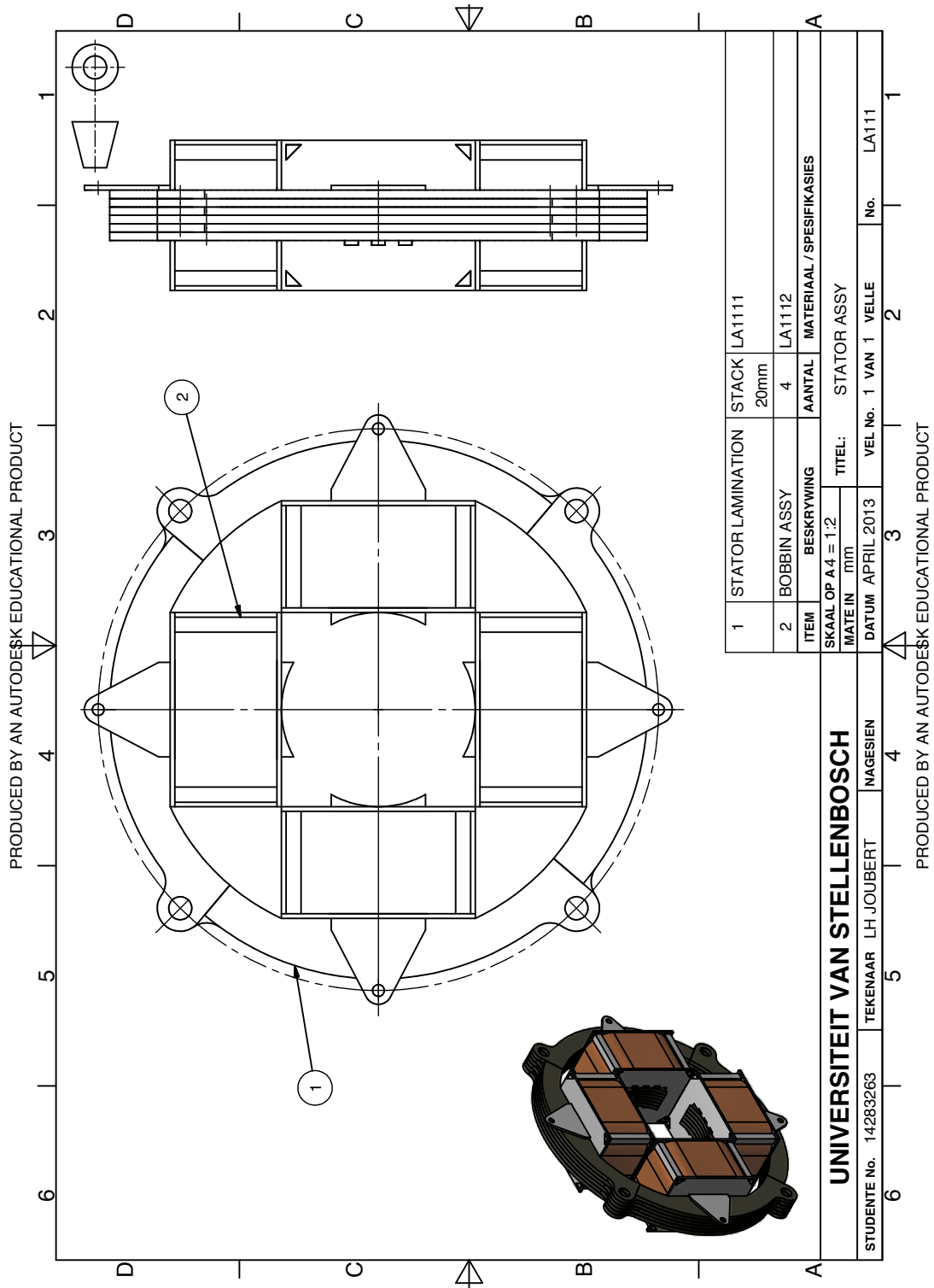


Figure D.11: Stator Assembly

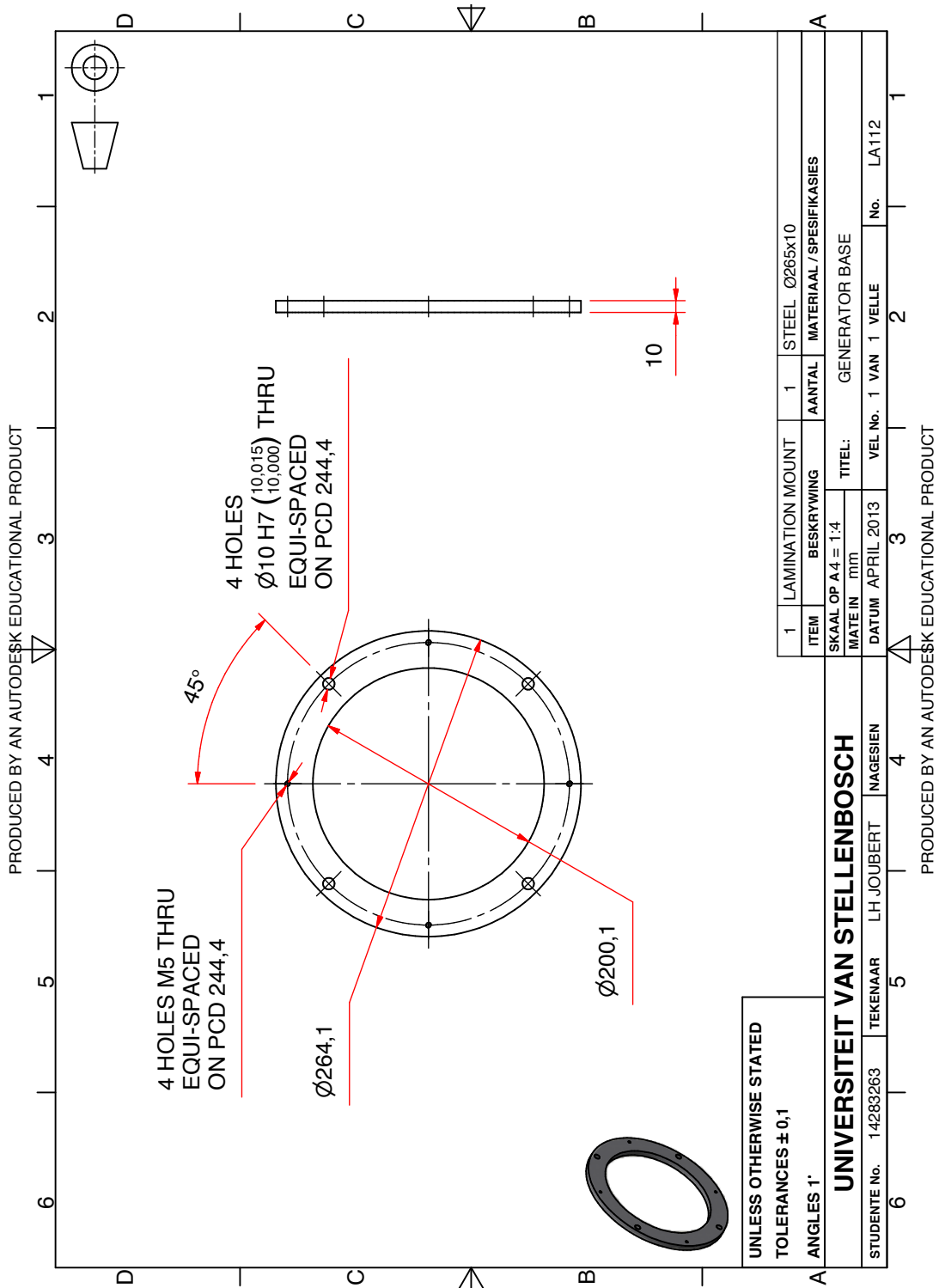


Figure D.12: Generator Base

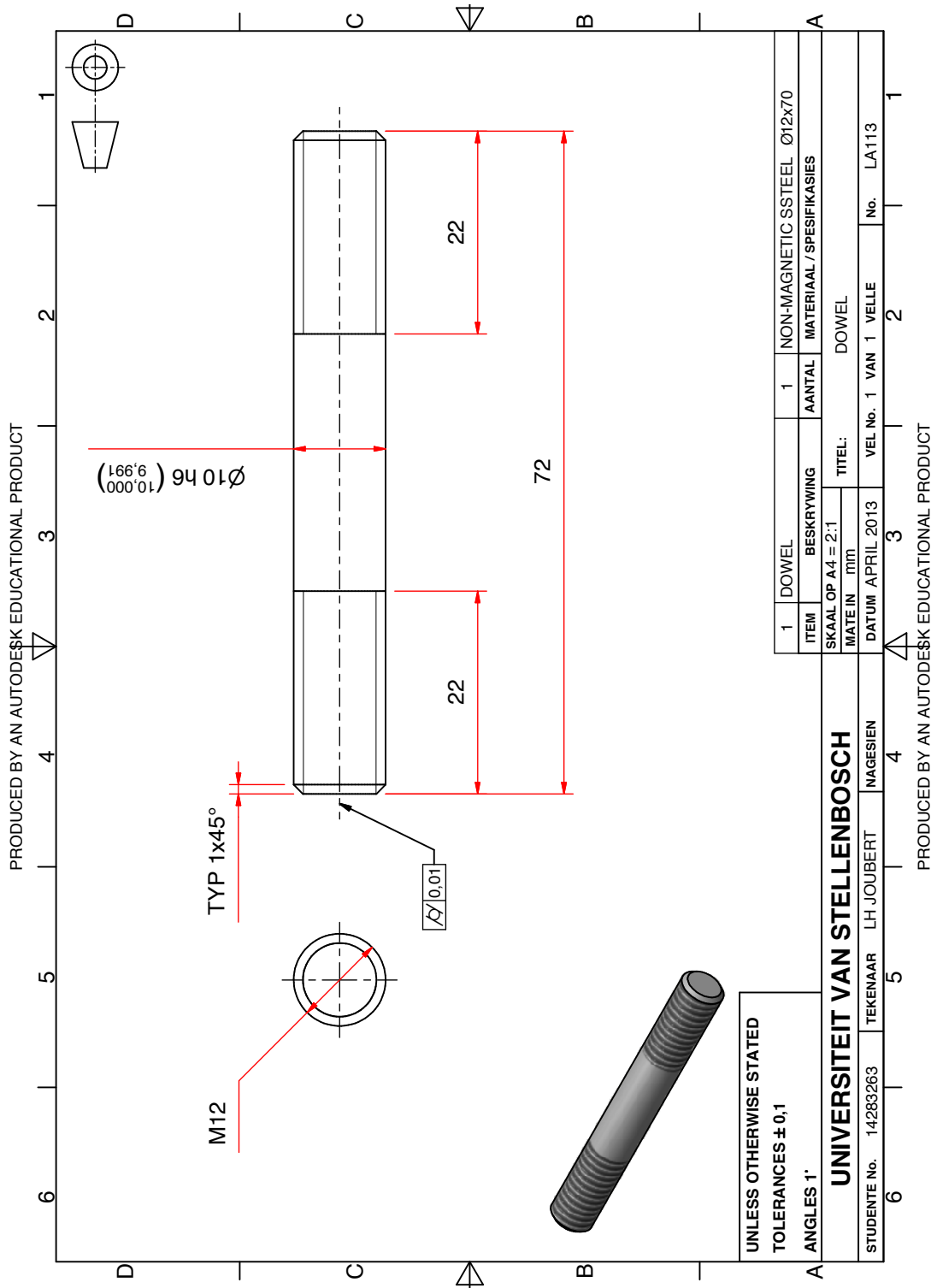


Figure D.13: Dowel

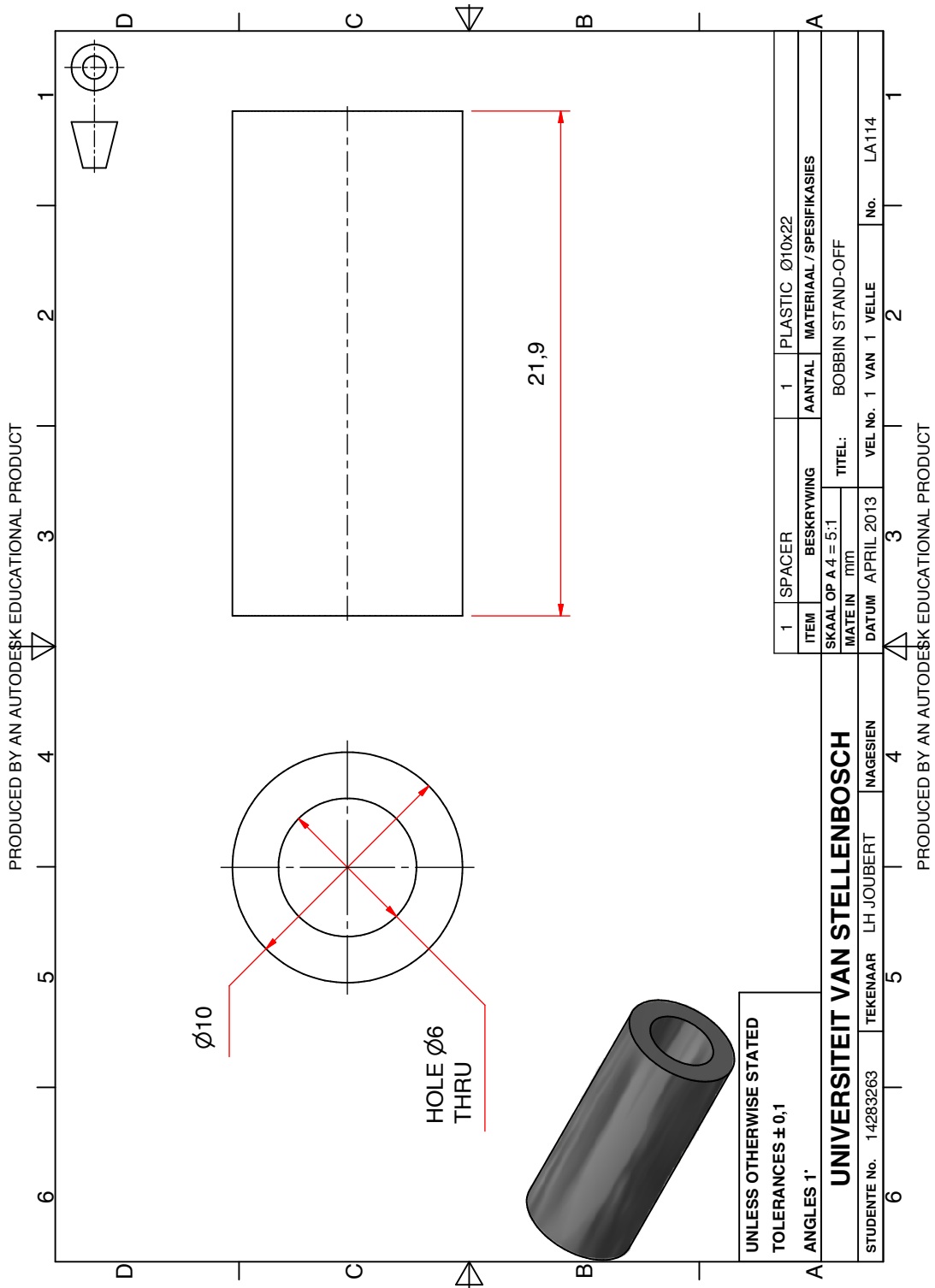


Figure D.14: Spacer

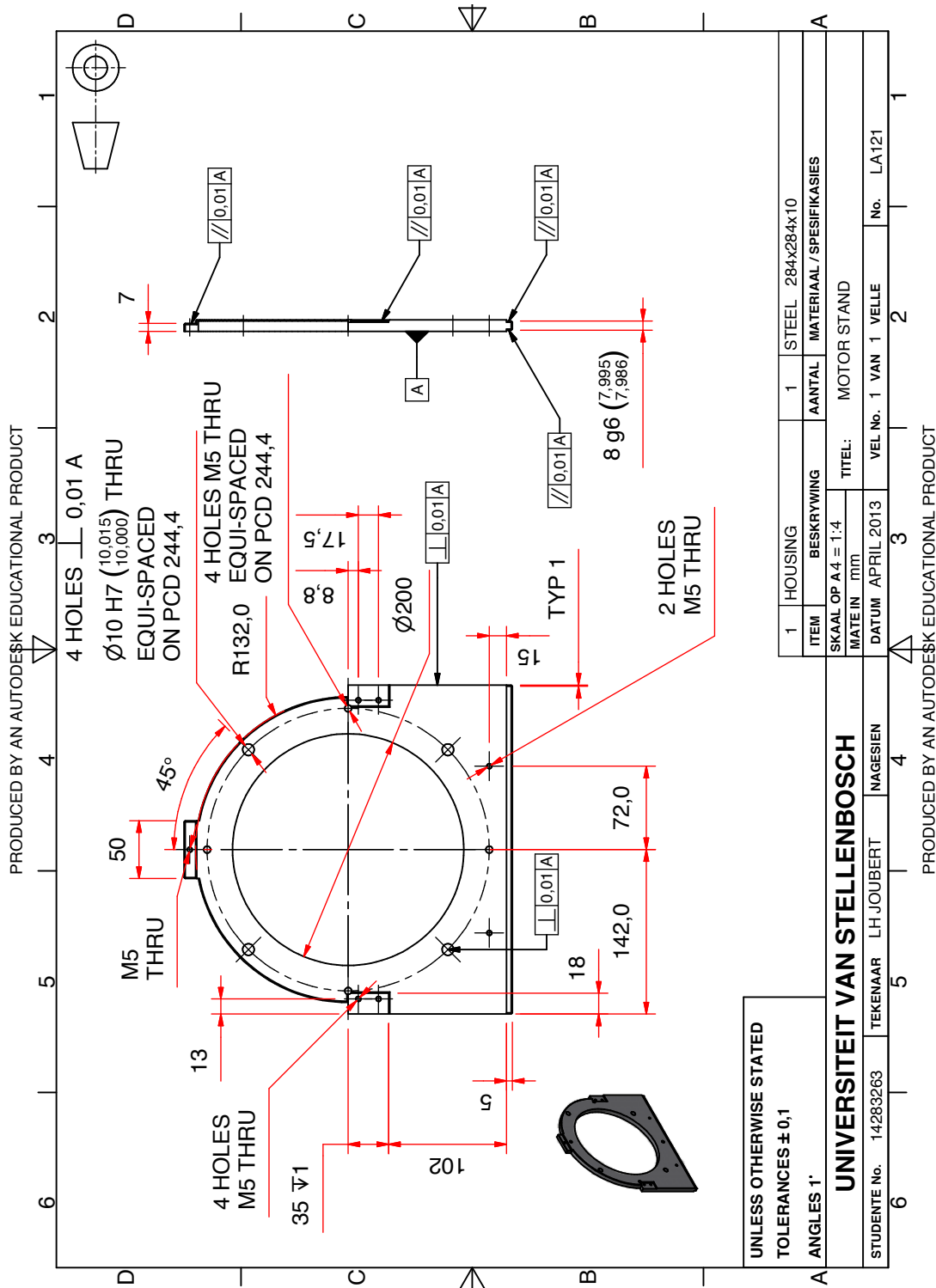


Figure D.15: Motor Stand

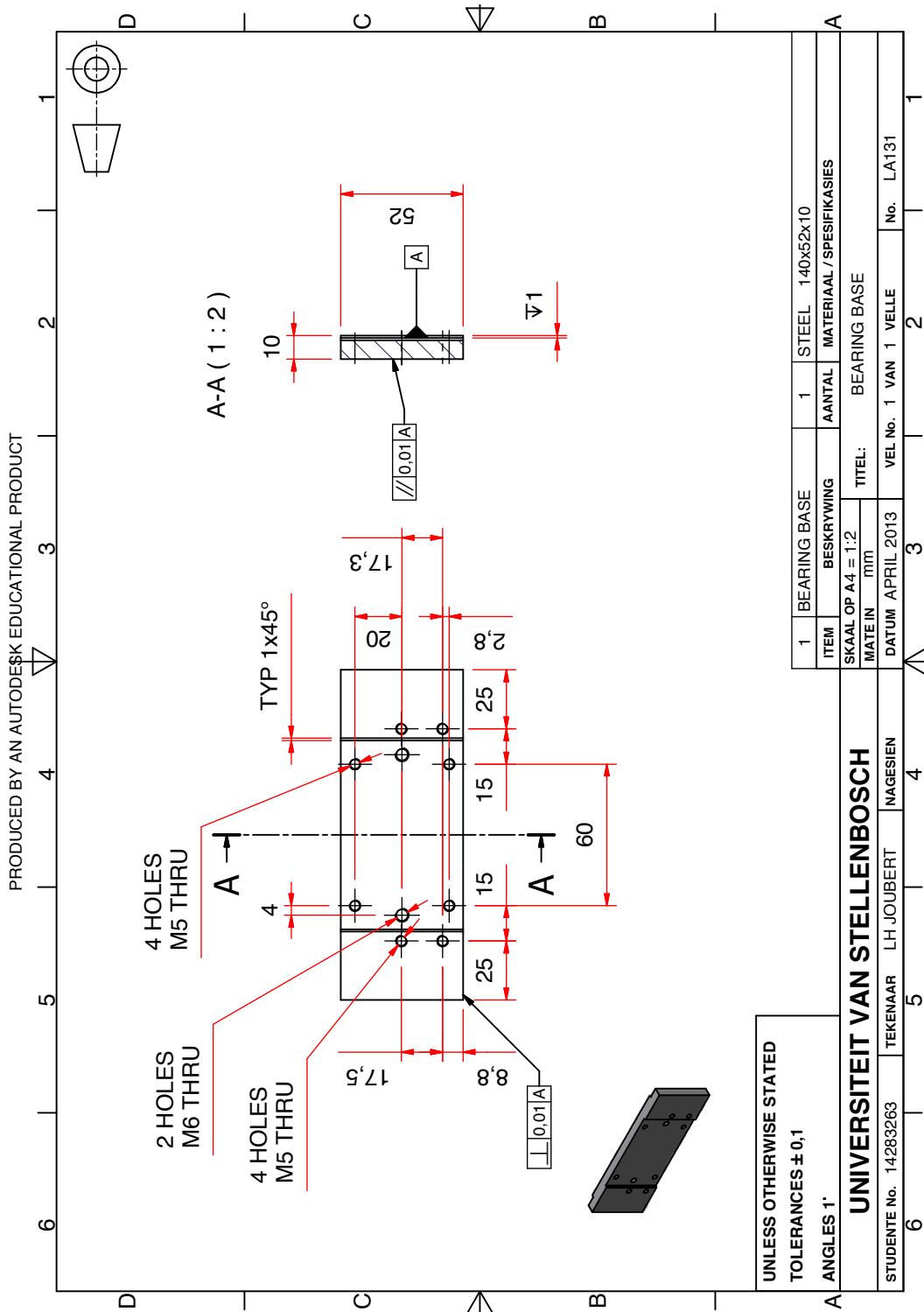


Figure D.16: Bearing Base

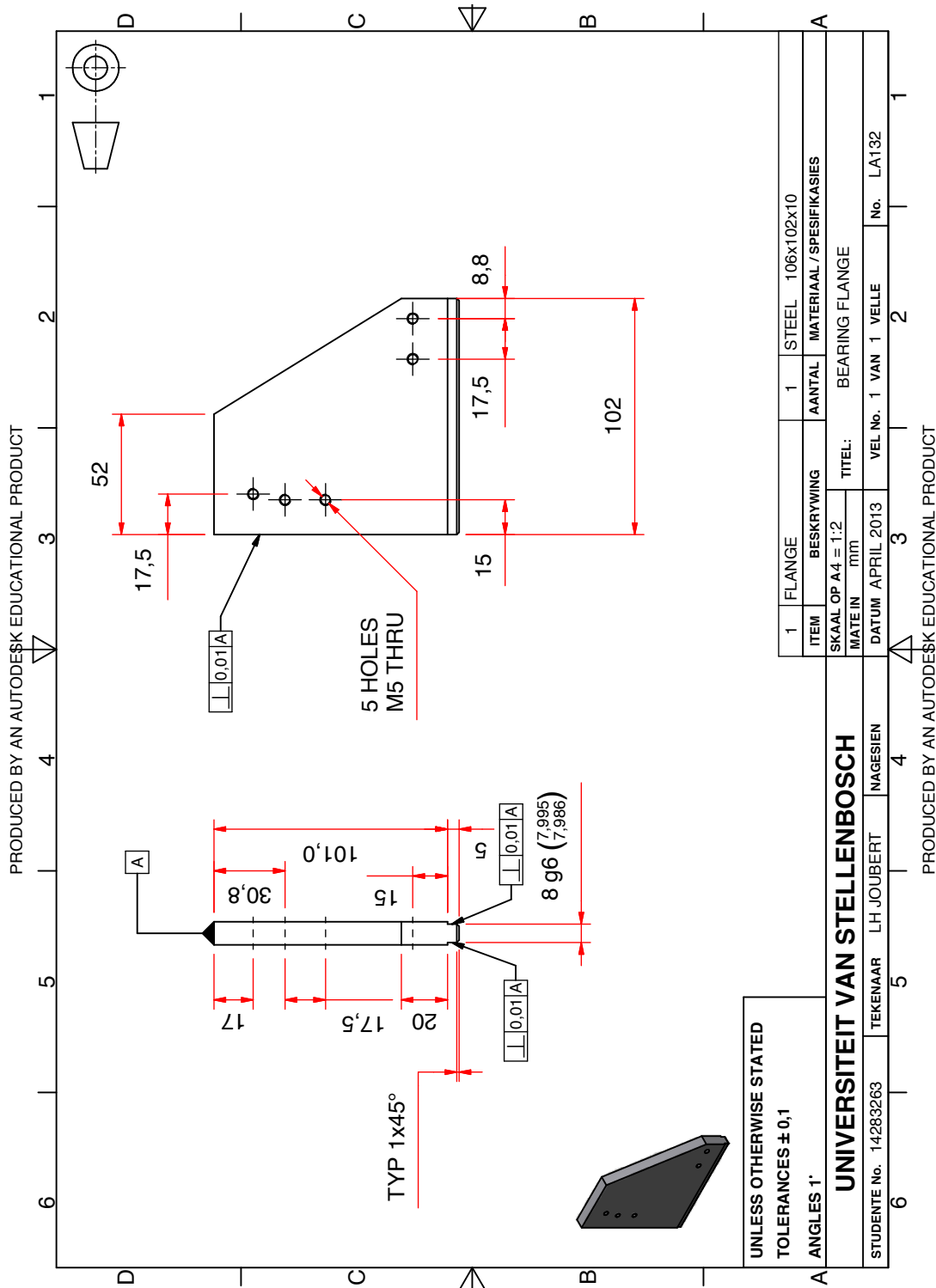


Figure D.17: Flange

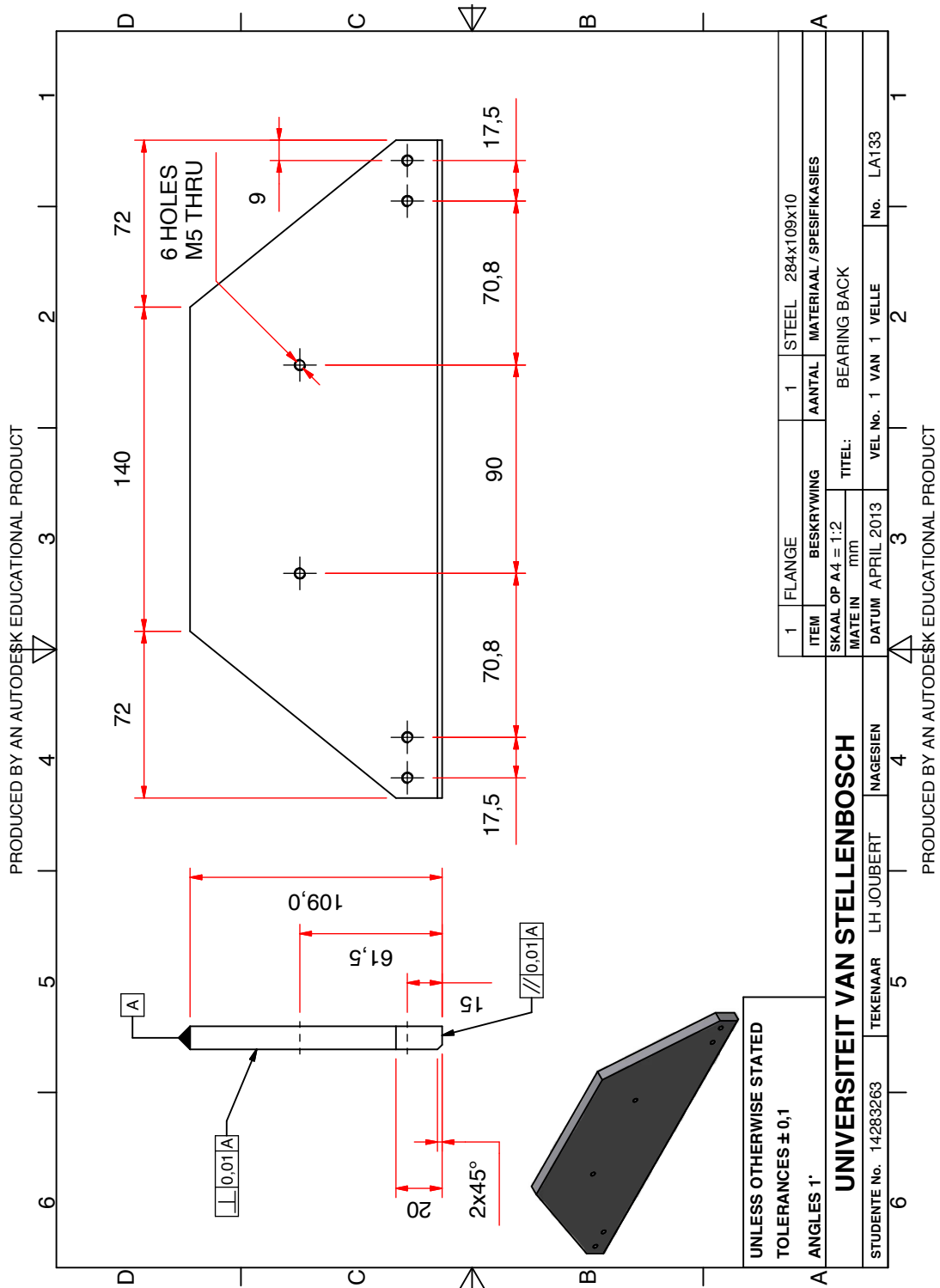


Figure D.18: Back Plate

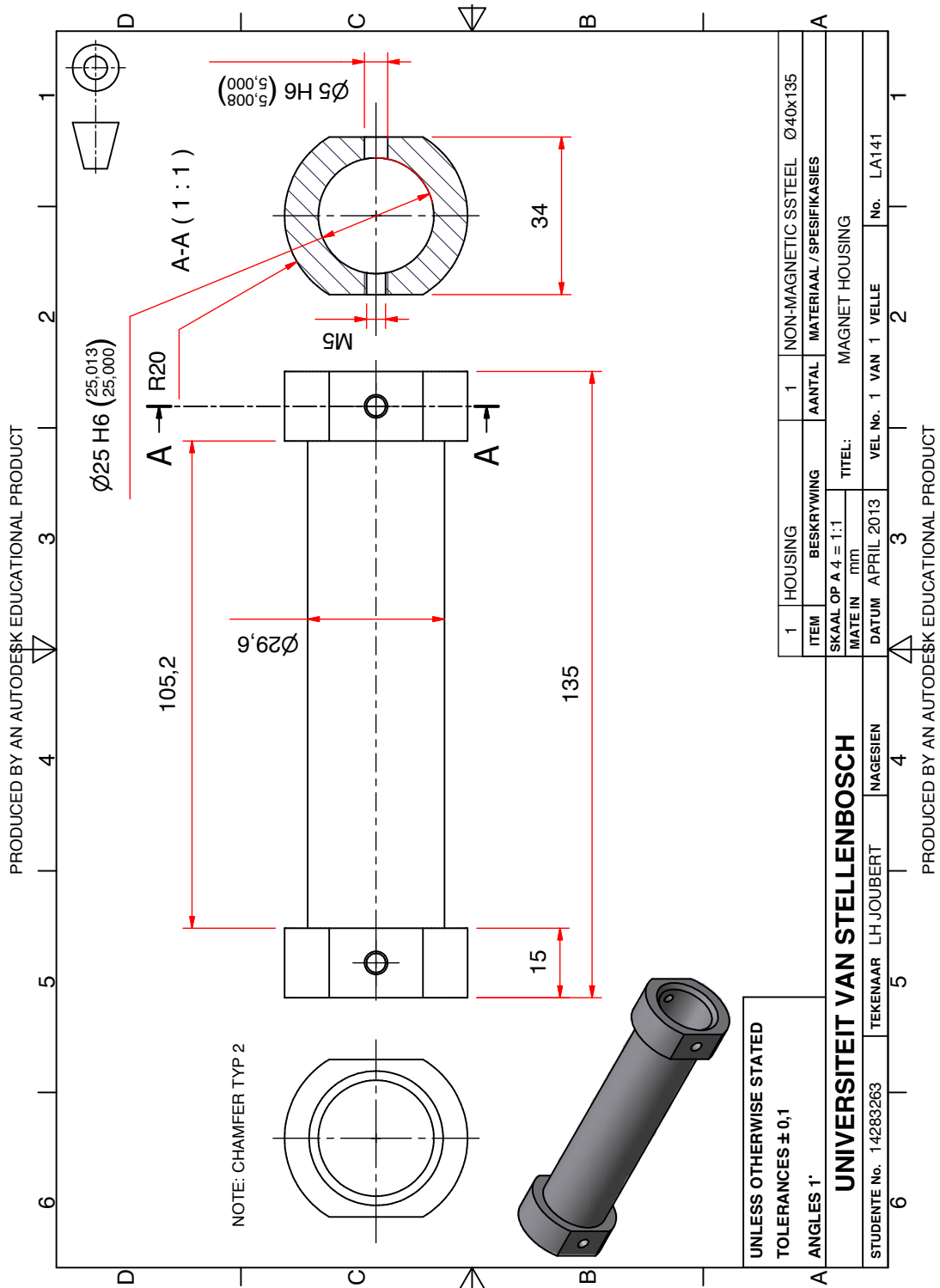


Figure D.19: Magnet Housing

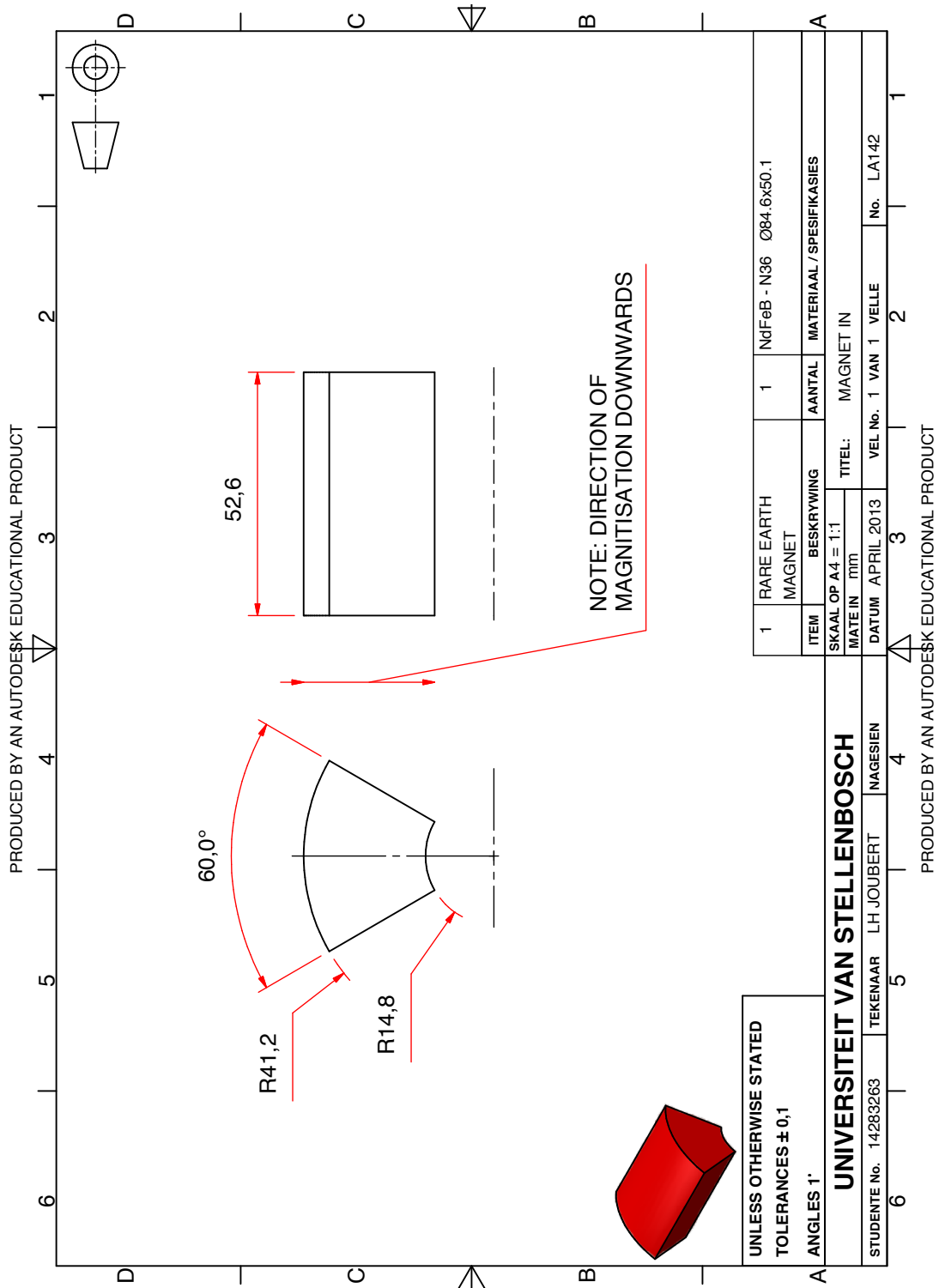


Figure D.20: Magnet In

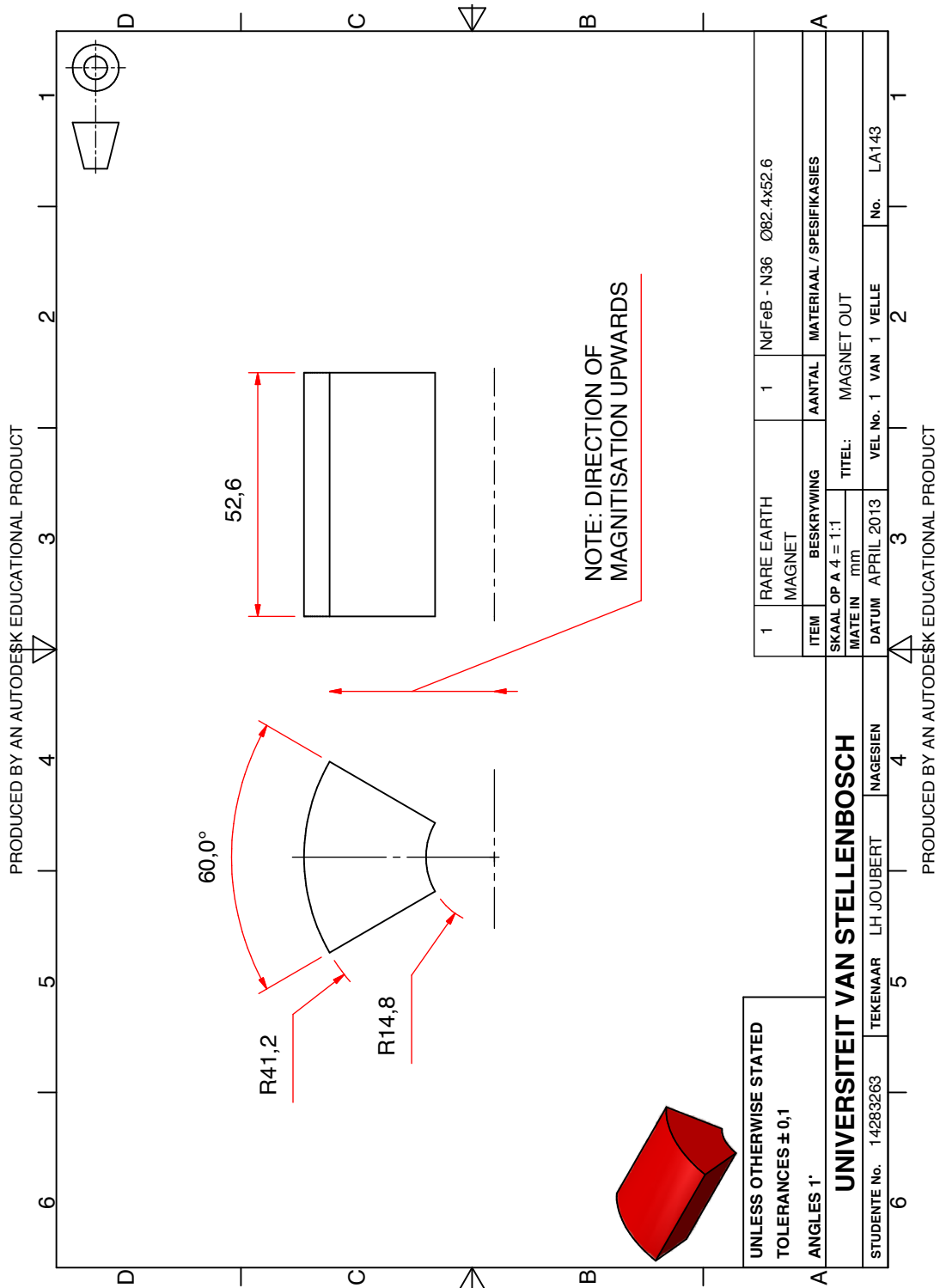


Figure D.21: Magnet In

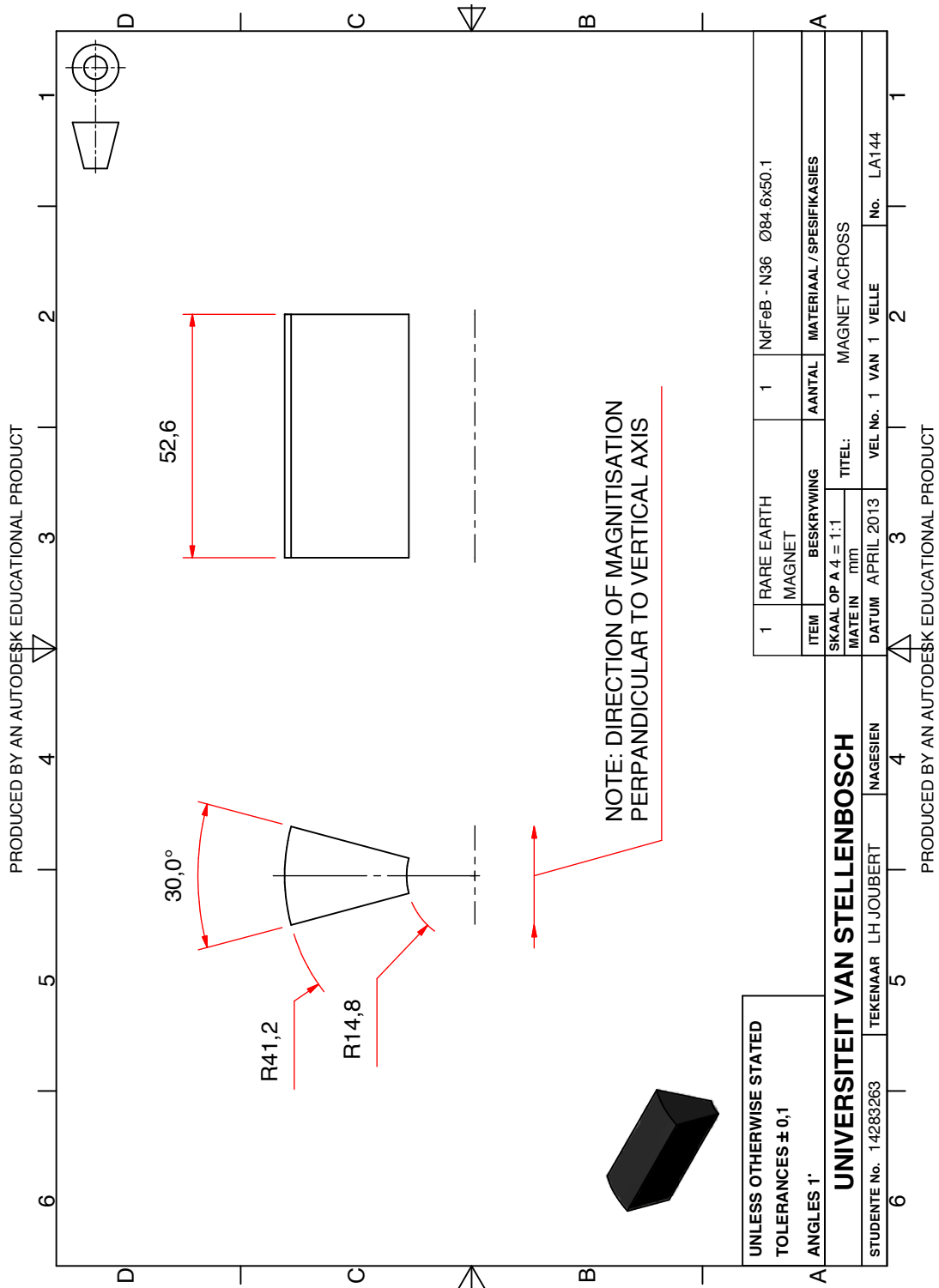


Figure D.22: Magnet Across

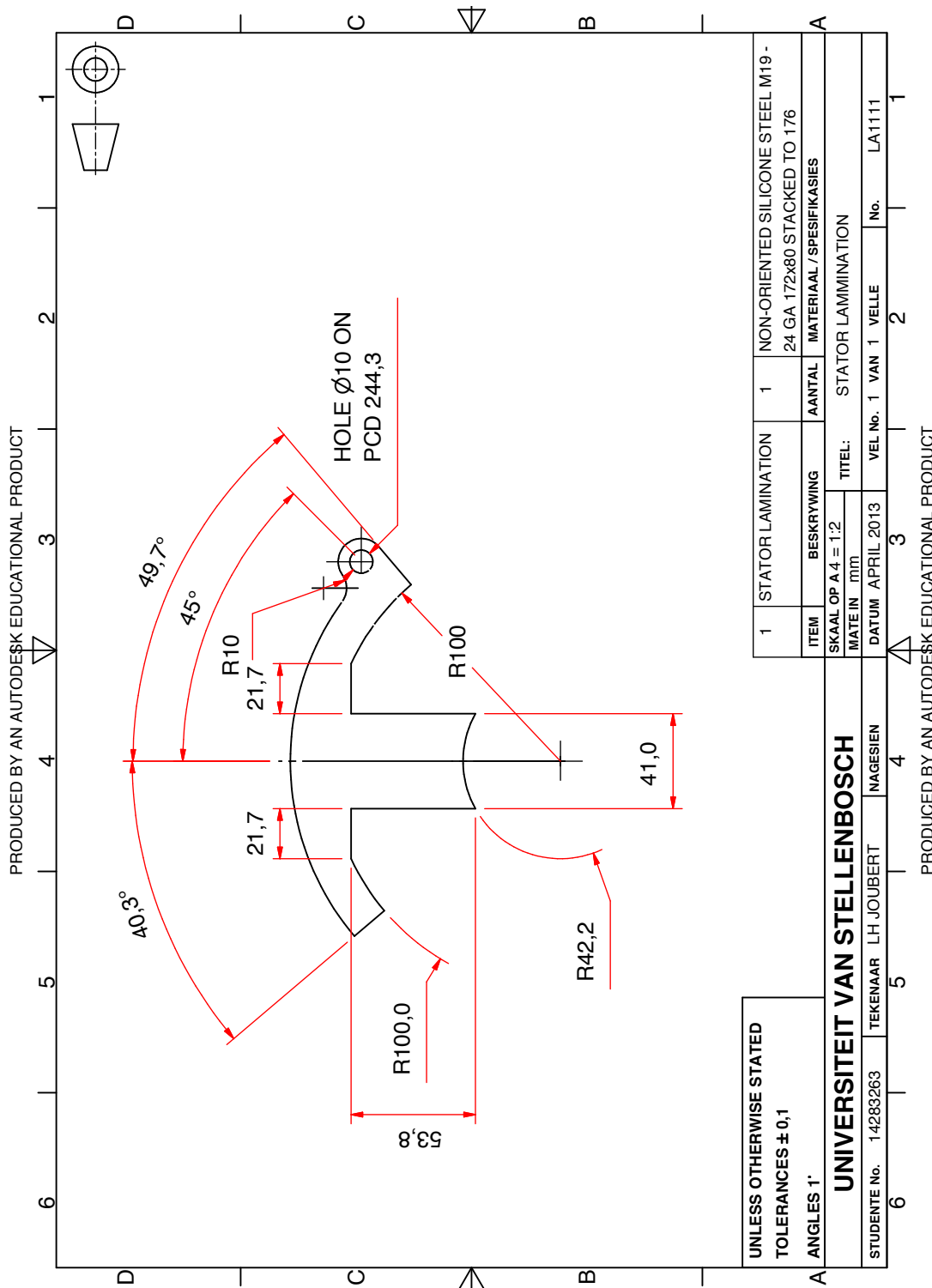


Figure D.23: Stator Lamination

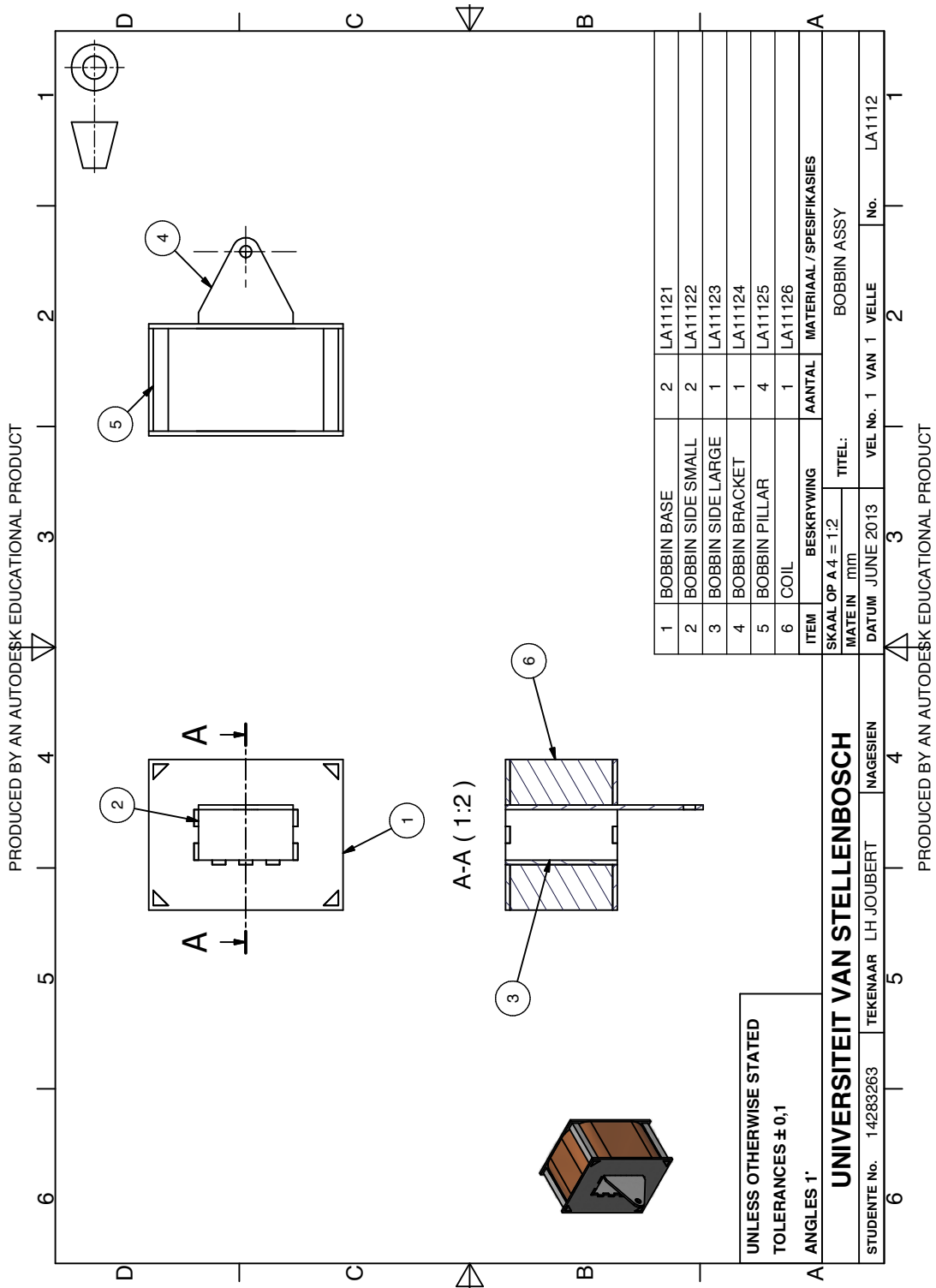


Figure D.24: Bobbin Assembly

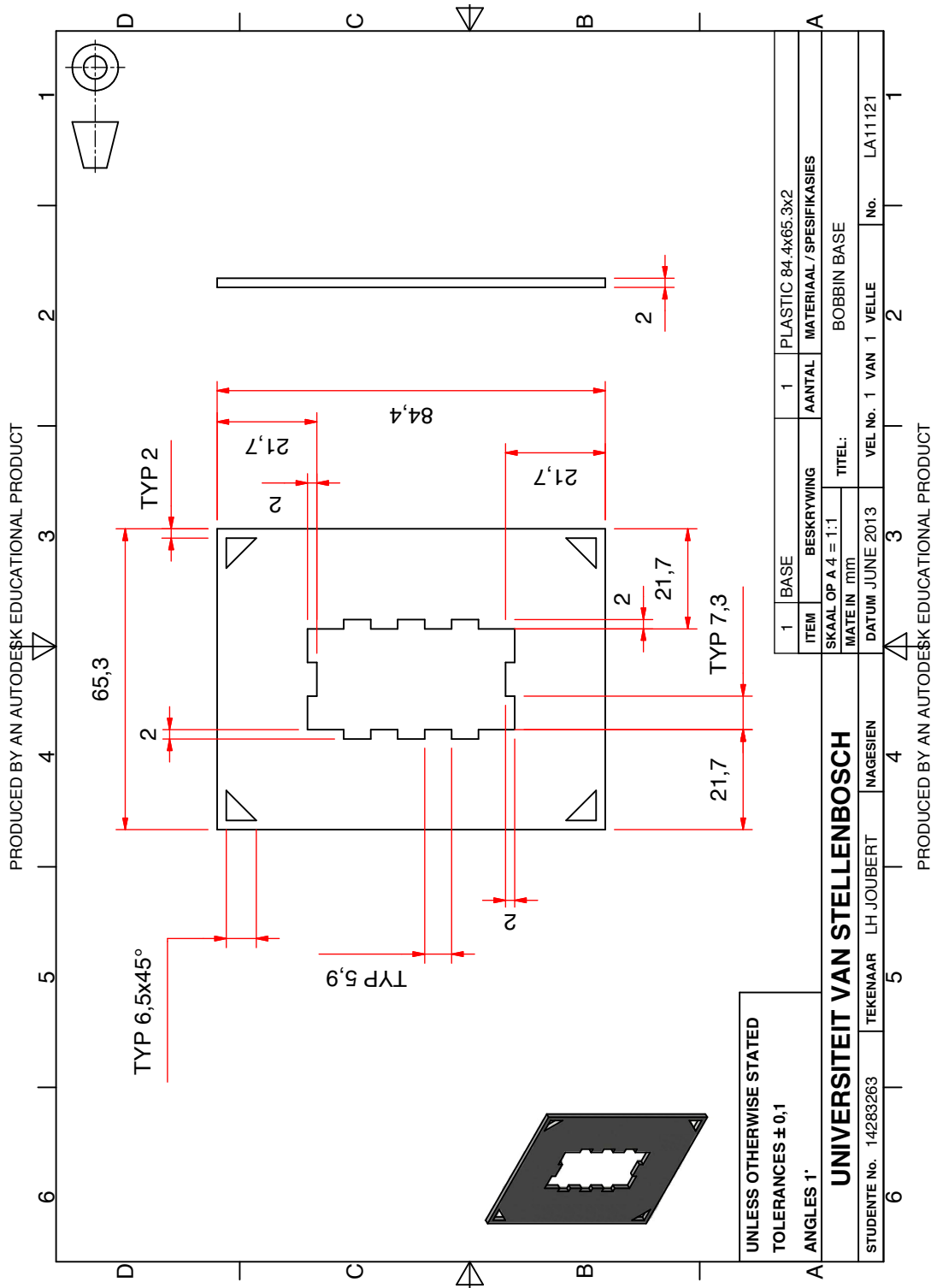


Figure D.25: Bobbin Base

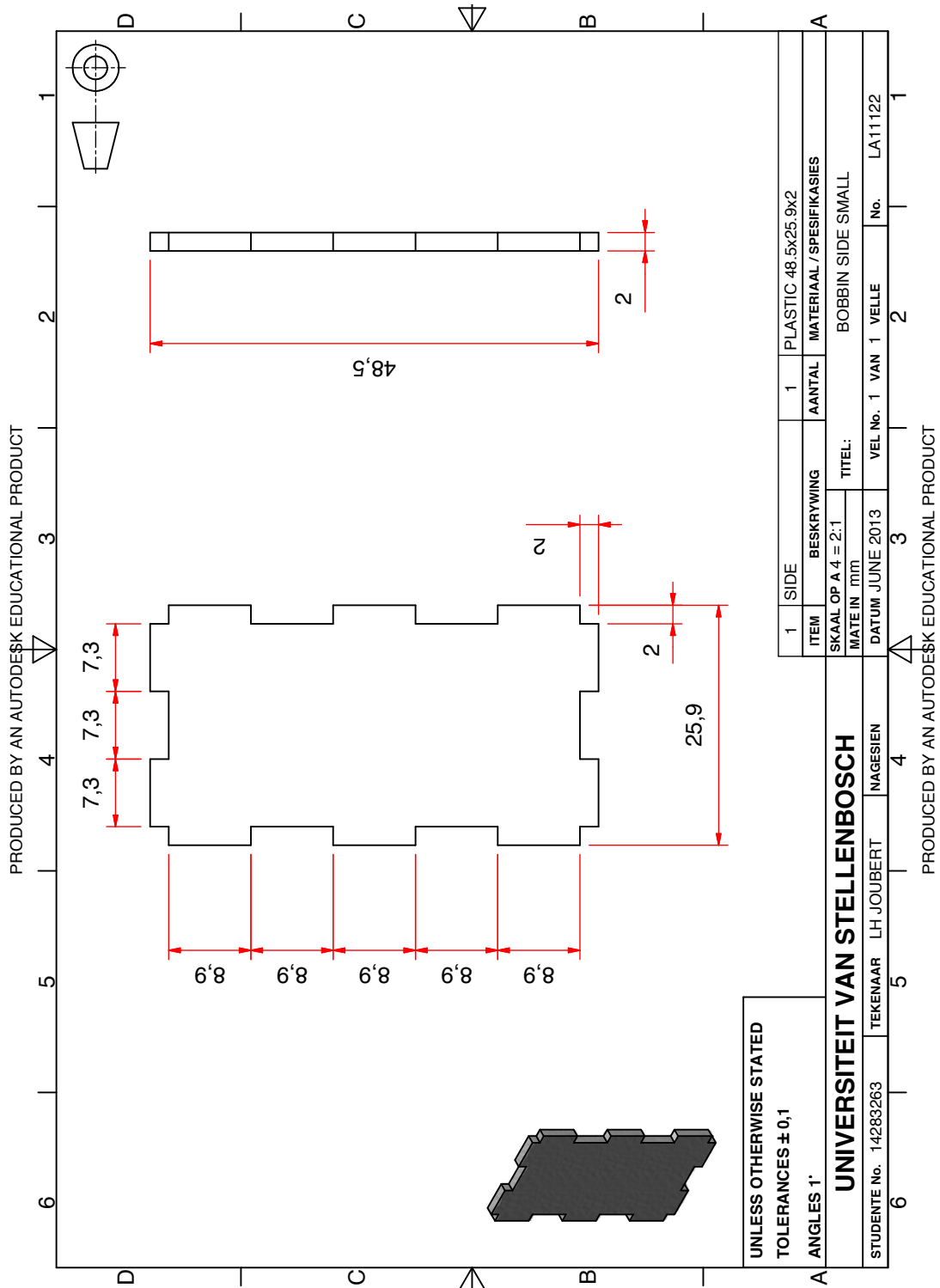


Figure D.26: Bobbin Small Vertical Side

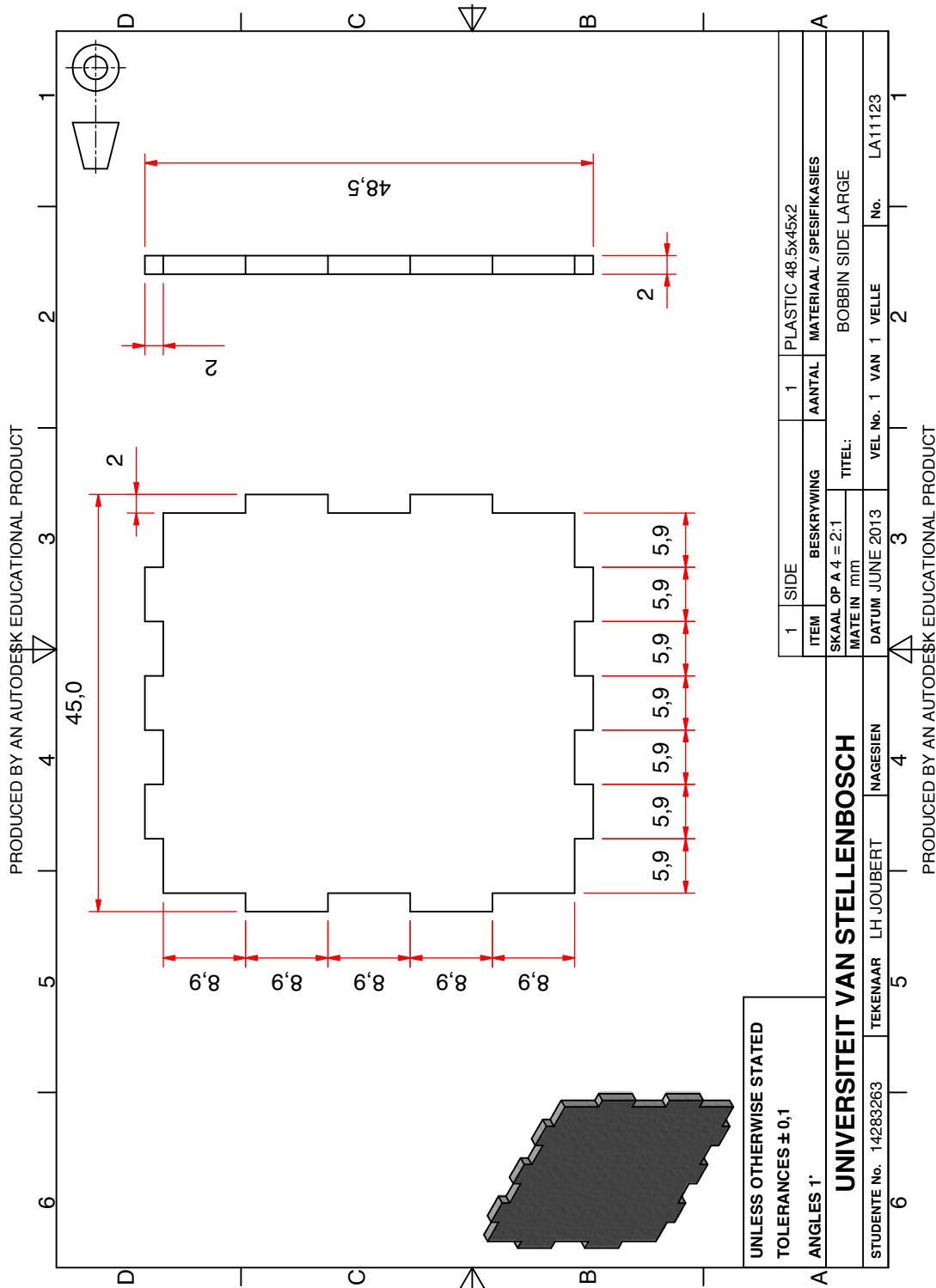


Figure D.27: Bobbin Large Vertical Side

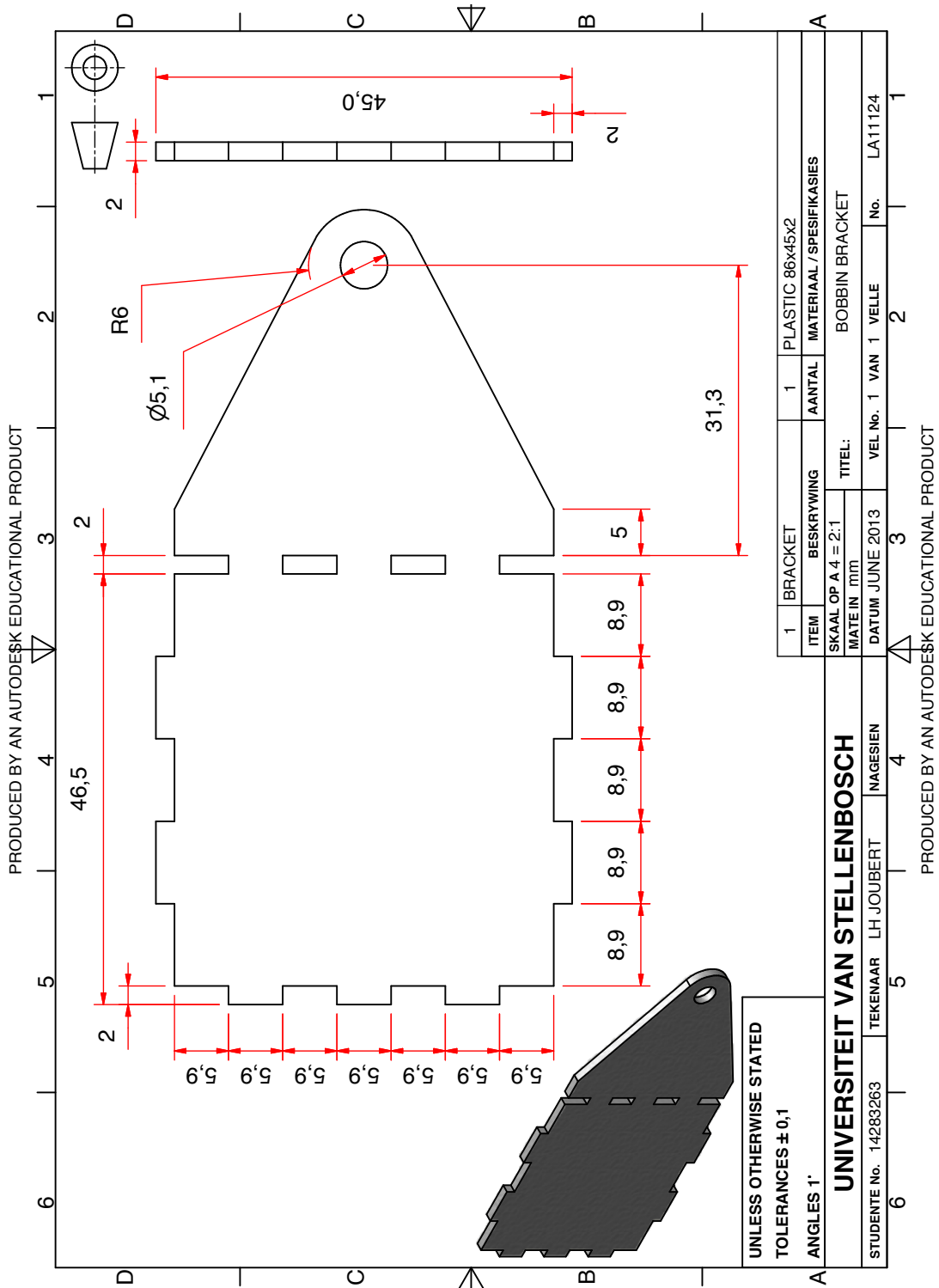


Figure D.28: Bobbin Bracket